

SYNTHESIS, CHARACTERIZATION AND ELECTROCHEMICAL  
ENHANCEMENT OF TIN OXIDE-BASED NANOFIBERS SYNTHESIZED  
BY ELECTROSPINNING PROCESS



A THESIS SUBMITTED IN PARTIAL FULFILLMENT OF THE REQUIREMENT FOR THE  
DEGREE OF DOCTOR PHILOSOPHY PROGRAM IN APPLIED CHEMISTRY  
DEPARTMENT OF CHEMISTRY  
FACULTY OF SCIENCE  
KING MONGKUT'S INSTITUTE OF TECHNOLOGY LADKRABANG  
2017  
KMITL-2017-SC-D-010-002



COPYRIGHT 2017

FACULTY OF SCIENCE

KING MONGKUT'S INSTITUTE OF TECHNOLOGY LADKRABANG

This material is reserved for educational use only, not allowed for commercial use.

Forbidden to modify the content, and cite the document when use.

หัวข้อวิทยานิพนธ์	การสังเคราะห์ การศึกษาสมบัติและการเพิ่มประสิทธิภาพทางเคมีไฟฟ้าของเส้นใยนาโนทินออกไซด์ที่เตรียมด้วยกระบวนการปั่นด้วยไฟฟ้า
ชื่อนักศึกษา	นายสมทบ สันติ เบ็ญจกุล
รหัสประจำตัว	๕๕๖๕๐๓๐๕
ปริญญา	ปรัชญาดุษฎีบัณฑิต
สาขาวิชา	เคมี
พ.ศ.	๒๕๖๐
อาจารย์ที่ปรึกษาวิทยานิพนธ์	รองศาสตราจารย์ ดร. สุวรรณ ไชยสิทธิ์
อาจารย์ที่ปรึกษาวิทยานิพนธ์ร่วม	รองศาสตราจารย์ ดร.วิษณุ เพชรภา

### บทคัดย่อ

ในงานวิทยานิพนธ์นี้เป็นการเตรียมเส้นใยของทินออกไซด์ ( $\text{SnO}_2$ ) ที่ทำการเจือด้วยธาตุแอนติโมนี สังเคราะห์ด้วยเทคนิคการปั่นเส้นใยด้วยไฟฟ้า และปลูกอนุภาคโลหะเงินบนเส้นใยของทินออกไซด์ที่เจือด้วยธาตุแอนติโมนี ( $\text{Ag}/\text{ATO}$ ) โดยสังเคราะห์ด้วยวิธีไฮโดรเทอร์มอลเพื่อเพิ่มความสามารถในการเร่งปฏิกิริยาออกซิเดชันของเอทานอล ทินคลอไรด์เพนตะไฮเดรต ( $\text{SnCl}_4 \cdot 5\text{H}_2\text{O}$ ) แอนติโมนีคลอไรด์ ( $\text{SbCl}_3$ ) และพอลิเมอร์ โพลีไวนิลไพโรลิโดน (PVP) ใช้เป็นสารตั้งต้นของการเตรียมเส้นใย กระบวนการปั่นเส้นใยด้วยไฟฟ้าที่เหมาะสมสำหรับการสังเคราะห์ คือ การใช้ความต่างศักย์ไฟฟ้ากำลังสูง 10 กิโลโวลต์ ระยะห่างระหว่างเข็มฉีดสารละลายกับฐานรองรับ 10 เซนติเมตร และอัตราการฉีดเส้นใย 0.5 มิลลิลิตรต่อชั่วโมง ผืนเส้นใยที่สังเคราะห์ได้จะนำไปเผาในบรรยากาศปกติที่ 600 องศาเซลเซียสเป็นเวลา 3 ชั่วโมง เพื่อให้ได้เส้นใยของทินออกไซด์ที่ทำการเจือด้วยธาตุแอนติโมนี เส้นใยออกไซด์ที่ได้จะผสมกับซิลเวอร์ไนเตรตในสารละลายเฮกซะเมทิลีนเตตระมีน (HMTA) ภายใต้ปฏิกิริยาของไฮโดรเทอร์มอล ที่อุณหภูมิ 90 องศาเซลเซียสเป็นเวลา 1 ชั่วโมงเพื่อให้ได้ตัวเร่งปฏิกิริยาโลหะเงินบนตัวรองรับเส้นใยของทินออกไซด์ที่ทำการเจือด้วยธาตุแอนติโมนี เส้นใยที่สังเคราะห์ได้จะนำไปวิเคราะห์ลักษณะเฉพาะด้วยเครื่องวัดการเลี้ยวเบนของรังสีเอ็กซ์ กล้องจุลทรรศน์อิเล็กตรอนแบบส่องกราด เอ็กซ์เรย์สเปกโตรสโกปีแบบกระจายพลังงาน และฟูเรียร์ทรานสฟอร์มอินฟราเรดสเปกโตรมิเตอร์ นอกจากนี้ได้ศึกษาสมบัติการเร่งปฏิกิริยาทางไฟฟ้าของตัวเร่งปฏิกิริยาโลหะเงินบนตัวรองรับเส้นใยของทินออกไซด์ที่ทำการเจือด้วยธาตุแอนติโมนีต่อการออกซิเดชันของ เอทานอลด้วยเทคนิคไซคลิกโวลแทมเมตรี (และ โครโนแอมเพอโรเมตรี ในตัวกลางสารละลายกรด จากการศึกษาพบว่าความเข้มข้นของสารละลายพอลิเมอร์ และความเข้มข้นของสารเจือในเส้นใยของทินออกไซด์ที่ทำการเจือด้วยธาตุแอนติโมนี เป็นปัจจัยที่กำหนดโครงสร้าง

สัณฐานวิทยาของสาร อีกประการหนึ่ง ตัวเร่งปฏิกิริยาโลหะเงินบนตัวรองรับเส้นใยของทินออกไซด์ที่ทำการเจือด้วยธาตุแอนติโมนีที่ได้ มีความเป็นรูพรุนสูงและมีพื้นผิวที่ขรุขระ ซึ่งสามารถเร่งปฏิกิริยาออกซิเดชันของเอทานอลได้ ปรากฏการณ์นี้เกี่ยวข้องกับความสามารถของตัวเร่งปฏิกิริยาบนตัวรองรับเส้นใยของทินออกไซด์ที่ทำการเจือด้วยธาตุแอนติโมนี ที่กำจัดการบวมของทินออกไซด์ที่ดูดซับบนพื้นผิวของตัวเร่งโลหะเงิน ส่งผลให้ปฏิกิริยาการแตกพันธะของคาร์บอน-คาร์บอน ของเอทานอล และเกิดเป็นคาร์บอนไดออกไซด์เพิ่มขึ้น สรุปได้ว่า ตัวเร่งปฏิกิริยาโลหะเงินบนตัวรองรับเส้นใยของทินออกไซด์ที่ทำการเจือด้วยธาตุแอนติโมนี เป็นตัวเลือกหนึ่งสำหรับการเป็นตัวเร่งของปฏิกิริยาออกซิเดชันของเอทานอลในเซลล์เชื้อเพลิงชนิดแบบป้อนสารเอทานอลโดยตรง

คำสำคัญ : กระบวนการไฮโดรเทอร์มอล, เทคนิคการปั่นเส้นใยด้วยไฟฟ้า, ปฏิกิริยาออกซิเดชันของเอทานอล, เส้นใยของทินออกไซด์



Thesis Title	Synthesis, Characterization and Electrochemical Enhancement of Tin Oxide-Based Nanofibers Synthesized by Electrospinning Process
Student Name	Somtop Santibenchakul
Student ID	55650305
Degree	Doctor of Philosophy
Program	Chemistry
Year	2017
Thesis Advisor	Assoc. Prof. Dr. Suwan Chaiyasith
Thesis Co-advisor	Assoc. Prof. Dr. Wisanu Pecharapa

## ABSTRACT

Antimony-doped tin oxide (ATO) fibers were synthesized using electrospinning technique while silver-ATO (Ag/ATO) catalyst were prepared using hydrothermal method to enhance the catalytic activity for the ethanol oxidation.  $\text{SnCl}_4 \cdot 5\text{H}_2\text{O}$ ,  $\text{SbCl}_3$  and polyvinylpyrrolidone (PVP) were used as tin and antimony sources and polymer template precursor, respectively. The optimized electrospinning process was carried out using applied voltage of 10 kV by maintaining tip to collector distance of 10 cm and the injection rate of mixed precursor was controlled at 0.5 ml/h. The as-spun fiber mats were calcined in air at  $600^\circ\text{C}$  for 3 h to yield the ATO nanofibers. Subsequently, the obtained fibers were mixed with  $\text{AgNO}_3$  in  $\text{C}_6\text{H}_{12}\text{N}_4$  (HMTA) solution and treated at  $90^\circ\text{C}$  for 1 h under hydrothermal reaction to receive Ag/ATO catalyst. The tin oxide based nanofibers were characterized by X-ray diffraction (XRD), scanning electron microscopy (SEM), energy dispersive X-ray spectrometry (EDX), and Fourier-transform infrared spectrometry (FTIR). Moreover, the electrocatalytic properties of Ag/ATO catalyst for ethanol oxidation were investigated by cyclic voltammetry (CV) and chronoamperometric techniques. It is found that the polymer solution concentration and doping concentration in ATO fibers plays a key role on their network morphology. The obtained Ag/ATO catalyst has high porosity and rough surface that exhibits a

catalytic activity for the ethanol oxidation reaction. This phenomenon can be attributed to the ability of ATO support catalyst to remove the CO adsorbed at the Ag surface catalyst. As a result, the reaction barrier for C–C bond splitting of ethanol and CO<sub>2</sub> production was increased. It can be concluded that Ag–ATO is a candidate ethanol oxidation catalyst for the reaction in direct ethanol fuel cells.

**Keywords:** hydrothermal process, electrospinning technique, ethanol oxidation reaction, tin oxide fibers



## Acknowledgements

This thesis was successfully completed by supporting of my best advisor, Assoc. Prof. Dr. Suwan Chaiyasith and co-advisor, Assoc. Prof. Dr. Wisanu Pecharapa. I would like to thank to them for great support and good advices in my life and my thesis.

I would like to thank Rajamangala University of Technology Tawan-Ok (RMUTTO) for the Ph. D scholarship.

This work was financially supported by KMITL research fund. Author gratefully acknowledge the support from Department of Chemistry, Faculty of Science, King Mongkut's Institute of Technology Ladkrabang (KMITL); College of Nanotechnology, King Mongkut's Institute of Technology Ladkrabang (KMITL) and Faculty of Engineering, Rajamangala University of Technology Thanyaburi (RMUTT) for XRD measurement.

Thank you to Nanomaterial Research Laboratory (NMRL) for very good relationships in my experimental laboratory. Finally, thank you to my wife and my parent for good encouragement.

(Mr. Somtop Santibenchakul)

# Table of Contents

	Page
Abstract in Thai .....	i
Abstract in English.....	iii
Acknowledgements.....	v
Table of Contents.....	vi
List of Tables.....	viii
List of Figures.....	ix
Abbreviations/Symbols.....	xiii
<b>Chapter 1 Introduction</b> .....	<b>1</b>
1.1 Research Motivation.....	1
1.2 Objectives of the study.....	2
1.3 Scopes of the study.....	3
1.4 Benefits of the study.....	3
<b>Chapter 2 Theory and Literature Reviews</b> .....	<b>4</b>
2.1 Tin (IV) Oxide.....	4
2.2 Electrospinning.....	5
2.3 Direct ethanol fuel cell.....	9
2.4 Cyclic voltammetry.....	14
2.5 Literature Reviews.....	16
<b>Chapter 3 Research methodology</b> .....	<b>36</b>
3.1 Chemical reagents.....	36
3.2 Equipments.....	37
3.3 Experimental methods.....	37
3.3.1 Synthesis of PVP nanofibers via electrospinning process .....	37
3.3.2 Synthesis of SnO <sub>2</sub> nanofibers with varied calcination temperature via electrospinning process .....	38
3.3.3 Synthesis of SnO <sub>2</sub> nanofibers with varied PVP concentration via electrospinning process .....	39
3.3.4 Synthesis of Sb doped SnO <sub>2</sub> (ATO) nanofibers with varied antimony concentration via electrospinning process.....	40

## Table of Contents (Con.)

	Page
3.3.5 Synthesis of Sb/F co-doped SnO <sub>2</sub> (AFTO) nanofibers with varied antimony concentration via electrospinning process.....	41
3.3.6 Synthesis of Ag/SnO <sub>2</sub> , Ag/ATO and Ag/AFTO electrocatalysts via hydrothermal method .....	42
3.3.7 Characterization .....	43
3.3.8 Working electrode fabrication and electrochemical measurement.	44
Chapter 4 Results and Discussion .....	45
4.1 Result and discussion .....	45
4.1.1 Comparison of morphologies between PVP fibers and as-spun SnO <sub>2</sub> fibers .....	45
4.1.2 Optimized calcination temperature of SnO <sub>2</sub> nanofibers.....	46
4.1.3 Optimized concentration of PVP solutions of SnO <sub>2</sub> nanofibers .....	50
4.1.4 Synthesized Sb doped SnO <sub>2</sub> (ATO) fibers.....	58
4.1.5 Synthesized Sb/F doped SnO <sub>2</sub> (AFTO) fibers.....	62
4.1.6 Comparison of material based on SnO <sub>2</sub> nanofibers.....	68
4.1.7 Synthesized Ag doped SnO <sub>2</sub> (Ag/SnO <sub>2</sub> ), Ag doped Sb/SnO <sub>2</sub> (Ag/ATO) and Ag doped Sb/F/SnO <sub>2</sub> (Ag/AFTO) fibers.....	70
4.1.8 Ethanol oxidation reaction based on Ag/SnO <sub>2</sub> electrocatalysts.....	76
Chapter 5 Conclusions and Suggestions .....	83
5.1 Conclusions .....	83
5.2 Suggestions .....	84
References.....	85
Appendix/Appendices.....	94
Appendix A.....	95
Appendix B.....	100
Appendix C.....	107
Author Biography .....	117

## List of Tables

Table	Page
Table 2.1 The properties of SnO <sub>2</sub> .....	4
Table 2.2 Comparison of processing techniques for synthesis polymer nanofibers.....	6
Table 2.3 Comparison of different fuels in a direct fuel cell .....	12



## List of Figures

Figure	Page
Figure 2.1 the tetragonal rutile structure of SnO <sub>2</sub> .....	5
Figure 2.2 Schematic diagram of the electrospinning system.....	6
Figure 2.3 Schematic diagram of a hydrogen/oxygen fuel cell.....	10
Figure 2.4 Schematic diagram of a direct ethanol fuel cell.....	13
Figure 2.5 A typical cyclic voltammogram of current versus potential. ....	16
Figure 2.6 (up) SEM image and (below) XRD patterns of SnO <sub>2</sub> hollow nanofibers.....	18
Figure 2.7 SEM image of SnO <sub>2</sub> nanotubes.....	19
Figure 2.8 SEM image of SnO <sub>2</sub> nanobelts.....	20
Figure 2.9 SEM image of porous SnO <sub>2</sub> fibers.....	21
Figure 2.10 SEM image of SnO <sub>2</sub> hollow microtubes.....	22
Figure 2.11 SEM image of Ag/SnO <sub>2</sub> composite nanotubes.....	23
Figure 2.12 SEM image of SnO <sub>2</sub> -core carbon-shell composite nanotubes .....	24
Figure 2.13 (up) FE-SEM image, (below) TEM image of Pt/SnO <sub>2</sub> nanofibers.....	25
Figure 2.14 SEM images of the Ag/SnO <sub>2</sub> heterostructures .....	26
Figure 2.15 (A) SEM image of Pure TiO <sub>2</sub> fibers; (B) SEM image of Ag/TiO <sub>2</sub> ; (C) TEM image of TiO <sub>2</sub> fibers; (D) TEM images of the Ag/TiO <sub>2</sub> fibers.....	27
Figure 2.16 (up) cyclic voltammograms and (below) chronoamperograms of various electrodes.....	29
Figure 2.17 Resistivity of ATO with different Sb dopant.....	30
Figure 2.18 cyclic voltammograms of (a) Pt-ATO/C, (b) Pt-SnO <sub>2</sub> /C, and (c) Pt/C in 1.0 M H <sub>2</sub> SO <sub>4</sub> + 1.0 M CH <sub>3</sub> OH aqueous solution.....	31
Figure 2.19 the propose mechanism of the ethanol oxidation reaction on Pt electrode in H <sub>2</sub> SO <sub>4</sub> solution.....	32
Figure 2.20 Proposed ethanol electro-oxidation mechanism over Pt/SnO <sub>2</sub> /C, indicating the products from the bulk and adsorbed on surface catalyst..	33

## List of Figures (Con.)

Figure	Page
Figure 2.21 Comparison of cyclic voltammogram for a SnO <sub>2</sub> /Pt electrode (red line) and a bare Pt electrode (black line) in ethanol 0.5 M with 0.1 M HClO <sub>4</sub> solution. (b) Comparison of chronoamperogram for ethanol oxidation activity on a SnO <sub>2</sub> /Pt electrode (red) and a bare Pt electrode (black) in the ethanol solution .....	34
Figure 2.22 Linear sweep voltammograms at different concentrations of ethanol in 1 M H <sub>2</sub> SO <sub>4</sub> . All potentials are referred to the reference hydrogen electrode. Sweep rate 50 mV s <sup>-1</sup> .....	35
Figure 3.1 Experiment procedure of PVP nanofibers.....	38
Figure 3.2 Experiment procedure of SnO <sub>2</sub> nanofibers with varied calcination temperature.....	39
Figure 3.3 Experiment procedure of SnO <sub>2</sub> nanofibers with varied PVP concentration.....	40
Figure 3.4 Experiment procedure of Sb doped SnO <sub>2</sub> (ATO) nanofibers with varied antimony concentration.....	41
Figure 3.5 Experiment procedure of Sb/F doped SnO <sub>2</sub> (AFTO) nanofibers with varied antimony concentration.....	42
Figure 3.6 Experiment procedure of Ag/SnO <sub>2</sub> , Ag/ATO and Ag/AFTO electrocatalysts.....	43
Figure 4.1 SEM images of (a) PVP nanofibers and (b) as-spun SnO <sub>2</sub> nanofibers containing PVP + SnCl <sub>4</sub> ·5H <sub>2</sub> O.....	45
Figure 4.2 TGA graph of thermal decomposition of PVP fibers and electrospun PVP/SnO <sub>2</sub> composite.....	47
Figure 4.3 XRD patterns of the undoped SnO <sub>2</sub> nanofibers calcined at various temperatures.....	48
Figure 4.4 SEM images and the distribution of diameter of the undoped SnO <sub>2</sub> nanofibers calcined at various temperatures.....	49

## List of Figures (Con.)

Figure	Page
Figure 4.5 SEM images and the distribution of diameter of the as-spun SnO <sub>2</sub> fibers prepared from precursors with the different PVP concentrations; (a) 6 % (b) 8% (c) 10% and (d) 12%wt. ....	51
Figure 4.6 SEM images and phase diagram of formation of SnO <sub>2</sub> nanostructures prepared from precursors with the different PVP concentrations; (a) 6 % (b) 8% (c) 10% and (d) 12%wt. ....	54
Figure 4.7 EDX spectrum and SEM images (Inset) of as-spun SnO <sub>2</sub> nanofibers .....	56
Figure 4.8 XRD pattern of after-calcined SnO <sub>2</sub> nanostructures prepared from precursors with the different PVP concentrations. ....	57
Figure 4.9 EDX spectrum and SEM images (Inset) of ATO nanofibers (a) before and (b) after calcination. ....	58
Figure 4.10 SEM image of SnO <sub>2</sub> nanofibers containing varied Sb concentration .....	60
Figure 4.11 XRD patterns of SnO <sub>2</sub> and Sb doped SnO <sub>2</sub> (ATO) nanofibers with different Sb concentrations. ....	62
Figure 4.12 XRD patterns of the AFTO nanofibers with varied Sb concentration calcined at 600°C. ....	63
Figure 4.13 SEM images of the Sb/F co-doped SnO <sub>2</sub> (AFTO) nanofibers with varied Sb concentration calcined at 600°C. ....	65
Figure 4.14 EDX spectrum and SEM images (Inset) of AFTO nanofibers (a) before and (b) after calcination. ....	67
Figure 4.15 XRD patterns of the undoped SnO <sub>2</sub> , ATO, FTO and AFTO nanofibers calcined at 600°C. ....	69
Figure 4.16 FTIR spectra of an as-synthesized and after-calcined SnO <sub>2</sub> , ATO, FTO and AFTO nanofibers. ....	70
Figure 4.17 XRD patterns of the SnO <sub>2</sub> and Ag/SnO <sub>2</sub> structures. ....	71
Figure 4.18 XRD patterns of the ATO and Ag/ATO structures. ....	72
Figure 4.19 SEM images and EDX spectra (inset) of (a) the SnO <sub>2</sub> , (b) Ag/SnO <sub>2</sub> structures. ....	73

## List of Figures (Con.)

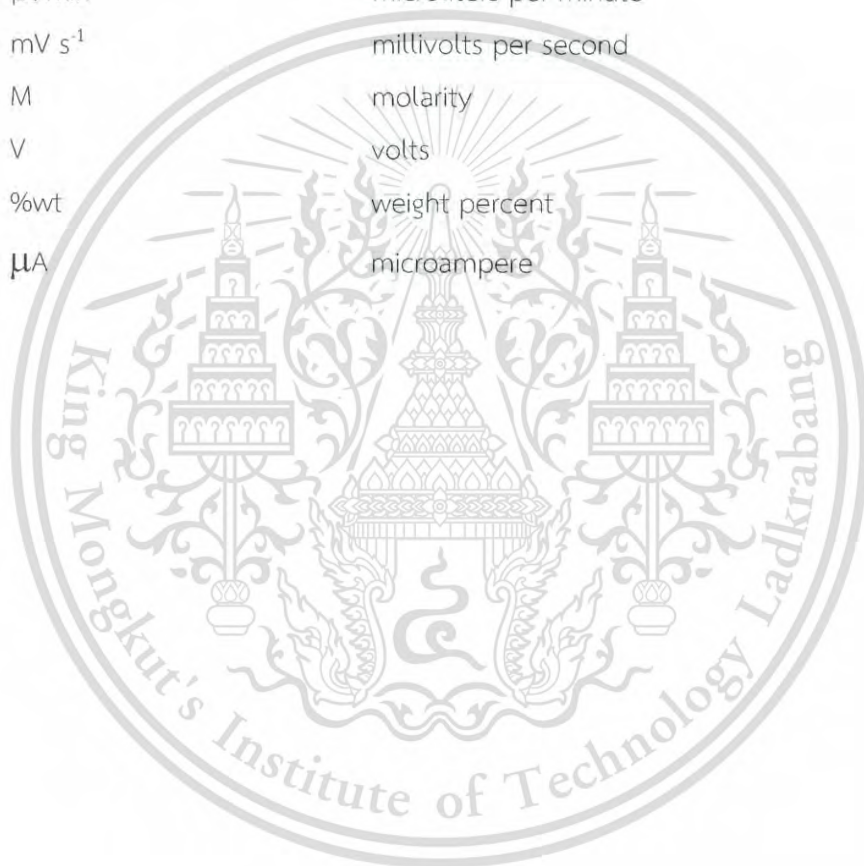
Figure	Page
Figure 4.20 SEM images and EDX spectra (inset) of (a) the ATO, (b) Ag/ATO structures.....	75
Figure 4.21 Comparison of voltammetric curves for Ag/SnO <sub>2</sub> , SnO <sub>2</sub> supported on FTO electrode and bare FTO electrode in 1.0 M ethanol with 1.0 M H <sub>2</sub> SO <sub>4</sub> solution. Scan rate: 50 mV/s. ....	76
Figure 4.22 Comparison of voltammetric curves for Ag/ATO, ATO supported on FTO electrode and bare FTO electrode in 1.0 M ethanol with 1.0 M H <sub>2</sub> SO <sub>4</sub> solution. Scan rate: 50 mV/s. ....	80
Figure 4.23 Comparison of voltammetric curves for Ag/SnO <sub>2</sub> , Ag/ATO and Ag/AFTO electrode in 1.0 M ethanol with 1.0 M H <sub>2</sub> SO <sub>4</sub> solution. Scan rate: 50 mV/s. ....	81
Figure 4.24 Chronoamperograms of Ag/SnO <sub>2</sub> /FTO, Ag/ATO/FTO and Ag/AFTO/FTO electrode at 0.25 V in 1.0 M ethanol with 1.0 M H <sub>2</sub> SO <sub>4</sub> solution.....	82

## Abbreviations/Symbols

DAFCs	direct alcohol fuel cells
DEFCs	direct ethanol fuel cells
PVP	polyvinylpyrrolidone
DMF	dimethylformamide
PVA	polyvinyl alcohol
HMTA	hexamethylenetetramine
TCO	transparent conducting oxide
ATO	antimony doped tin oxide
FTO	fluorine doped tin oxide
AFTO	antimony-fluorine co-doped tin oxide
MW	molecular weight
SEM	scanning Electron Microscopy
XRD	x-ray diffractometer
EDX	energy-dispersive X-ray spectroscopy
TGA	thermogravimetric Analysis
FTIR	fourier-transform infrared spectroscopy
CV	cyclic voltammetry
CA	chronoamperometry
Pt/C	carbon supported platinum
Pt/SnO <sub>2</sub>	tin oxide supported platinum
Ag/SnO <sub>2</sub>	tin oxide supported silver
Ag/SnO <sub>2</sub> /FTO	tin oxide supported silver on fluorine doped tin oxide substrate
Ag/ATO/FTO	antimony doped tin oxide supported silver on fluorine doped tin oxide substrate
Ag/AFTO/FTO	antimony-fluorine co-doped tin oxide supported silver on fluorine doped tin oxide substrate
Pt-SnO <sub>2</sub> /MWCNT	multi-walled carbon nanotubes supported platinum-tin oxide

Pt-ATO/MWCNT	multi-walled carbon nanotubes supported platinum-antimony doped tin oxide
TiO <sub>2</sub>	titanium dioxide
V <sub>2</sub> O <sub>5</sub>	vanadium (V) oxide
ZrO <sub>2</sub>	zirconium dioxide
SnO <sub>2</sub>	tin dioxide
Mn <sub>x</sub> O <sub>y</sub>	manganese oxide
WO <sub>x</sub>	tungsten oxide
MoO <sub>x</sub>	molybdenum oxide
RuO <sub>2</sub>	ruthenium (IV) oxide
CaSiO <sub>2</sub>	calcium silicate
MgO	magnesium oxide
CoO <sub>x</sub>	cobalt oxide
NO <sub>x</sub>	nitrogen oxides
CH <sub>3</sub> CH <sub>2</sub> OH	ethanol
CH <sub>3</sub> OH	methanol
SnCl <sub>2</sub> ·2H <sub>2</sub> O	tin (II) chloride dihydrate
SnCl <sub>4</sub> ·5H <sub>2</sub> O	tin (IV) chloride pentahydrate
SbCl <sub>3</sub>	Antimony (III) chloride
AgNO <sub>3</sub>	silver nitrate
H <sub>2</sub> PtCl <sub>6</sub> ·6H <sub>2</sub> O	chloroplatinic acid hexahydrate
HCl	hydrochloric acid
NaOH	sodium hydroxide
H <sub>2</sub> SO <sub>4</sub>	sulfuric acid
NH <sub>4</sub> F	ammonium fluoride
Eq	equation
Å	angstrom
g/cm <sup>3</sup>	gram per cubic centimeter
eV	electron volt
g·mol <sup>-1</sup>	gram per mol
°C	degree Celsius
H <sup>+</sup>	hydrogen ion
e	electron

$E_{pa}$	an anodic peak potential
$i_{pa}$	an anodic peak current
$E_{pc}$	a cathodic peak potential
$i_{pc}$	a cathodic peak current
kV	kilovolt
cm	centimeter
ml/h	milliliters per hour
$^{\circ}\text{C min}^{-1}$	degree Celsius per minute
$\mu\text{l/min}$	microliters per minute
$\text{mV s}^{-1}$	millivolts per second
M	molarity
V	volts
%wt	weight percent
$\mu\text{A}$	microampere



# Chapter 1

## Introduction

### 1.1 Research Motivation

Over the past of decades, the fossil fuels include petroleum, coal and natural gas were the main energy sources to fulfill the human activities in daily uses. The high rate of consumption of these fossil fuels was continuing while the amount of fossil fuels was drastically reduced. As a result, many researches have focused on alternative or renewable energy sources. Fuel cell is a candidate generation system to provide the energy that converts the chemical energy to the electrical energy. In general, it comprises a solid membrane that separates two electrodes producing electrical energy through an electrochemical reaction [1-2]. Direct alcohol fuel cell (DAFC) is a type of fuel cell that the alcohol oxidation reaction is occurred at the anode of fuel cell. Ethanol is highly selected as fuel in DAFCs because it is less toxic, inexpensive, and higher electrochemical reactivity. It can also be produced in large amounts from agricultural processes that provide the continuous available energy source. The complete oxidation of ethanol in redox reaction could produce  $8.0 \text{ kW h}^{-1} \text{ kg}^{-1}$  and generate 12 electrons in one reaction. Moreover, DEFCs give high-power density at low temperature [3-7]. Nevertheless, the main drawback is the high cost and the low utilization of electrocatalyst in the anode of DEFCs [8]. The electrocatalytic activity of ethanol oxidation reaction is typically dependent on the size and the dispersion of the electrocatalyst [9]. Furthermore, the properties of supporting catalyst such as the surface characteristics are effective for the catalyst to produce high catalytic activity [10]. In general, carbon supported platinum is used as catalyst for ethanol oxidation reaction, but it displays a lower percentage of complete oxidation reaction [11]. Recently, several studies have focused on some of metal oxides such as  $\text{TiO}_2$  [12],  $\text{V}_2\text{O}_5$  [13],  $\text{ZrO}_2$  [14] and  $\text{SnO}_2$  [15-16] that have been used as the support of Pt catalysts for improving the electrocatalytic activity of ethanol oxidation reaction. Tin oxide ( $\text{SnO}_2$ ) was usually chosen as supporting catalyst in DEFCs because of its unique electrical conductivity, catalytic properties and chemical stability [17]. The co-operation of Pt/ $\text{SnO}_2$  could further enhance the catalytic activity for ethanol oxidation reaction,

This material is reserved for educational use only, not allowed for commercial use.

Forbidden to modify the content, and cite the document when use.

comparing to a pure Pt catalyst [18]. In the same way, doping Antimony (Sb) into the  $\text{SnO}_2$  lattice process is an effective route to improve their response and sensitivity [19]. However, catalyst properties of semiconducting oxides were not effective when its surface was coated with Pt particles. As a result, their electrical conductivity was low and most of surface area was not active [20]. Many researches have focused on platinum as the anode catalyst in direct ethanol fuel cells. Platinum is the best noble metal catalyst for ethanol electro-oxidation but the cost of Pt precursors is typically very expensive. On the other hand, many electrocatalysts were chosen to substitute Pt although the efficiency were inferior.

In this work, the silver (Ag) electrocatalyst was fabricated onto the surfaces of support catalysts for ethanol oxidation reaction. Support catalysts based on  $\text{SnO}_2$  were synthesized by electrospinning technique in order to provide relatively high surface area to volume ratio accompanying small pore size. Finally, The  $\text{Ag}/\text{SnO}_2$ ,  $\text{Ag}/\text{ATO}$  and  $\text{Ag}/\text{AFTO}$  electrocatalysts were synthesized by hydrothermal method. The structures and morphologies of the synthesized catalysts were characterized and the electrochemical properties were evaluated in ethanol solution.

## 1.2 Objectives of the study

- 1) To study the processes for synthesizing  $\text{SnO}_2$  fibers by the electrospinning technique and calcination process.
- 2) To study effect of polymer concentration on the properties of electrospun  $\text{SnO}_2$  fibers.
- 3) To study effect of antimony doping concentration on the properties of Sb doped  $\text{SnO}_2$  (ATO) and Sb/F co-doped  $\text{SnO}_2$  (AFTO) fibers.
- 4) To study the route for synthesizing  $\text{Ag}/\text{SnO}_2$ ,  $\text{Ag}/\text{ATO}$  and  $\text{Ag}/\text{AFTO}$  catalyst for ethanol oxidation reaction.
- 5) To study the electrochemical properties of the  $\text{Ag}/\text{SnO}_2$ ,  $\text{Ag}/\text{ATO}$  and  $\text{Ag}/\text{AFTO}$  catalyst for ethanol oxidation reaction.

### 1.3 Scopes of the study

- 1) To synthesize SnO<sub>2</sub> nanofibers by an electrospinning technique and calcination process with various calcination temperature and polymer template concentration.
- 2) To synthesize the ATO and AFTO nanofibers by electrospinning technique and calcination process with various Sb doping concentration.
- 3) To synthesize the Ag/SnO<sub>2</sub>, Ag/ATO and Ag/AFTO catalyst for ethanol oxidation reaction.
- 4) To study the effects of the calcination temperature and the polymer concentration on the structural properties and morphologies of SnO<sub>2</sub> fibers.
- 5) To study the effects of the antimony doping concentration on the structural properties and morphologies of ATO and AFTO fibers.
- 6) To study the electrochemical properties of Ag/SnO<sub>2</sub>, Ag/ATO and Ag/AFTO catalysts.

### 1.4 Benefits of the study

- 1) To obtain the optimized calcination temperature for synthesizing SnO<sub>2</sub> fibers.
- 2) To obtain the electrospun SnO<sub>2</sub>, ATO and AFTO nanofibers.
- 3) To understand effect of calcination temperature, polymer concentration and Sb doping concentration on structural properties and morphologies of the obtained fibers.
- 4) To obtain the Ag/SnO<sub>2</sub>, Ag/ATO and Ag/AFTO catalysts for ethanol oxidation reaction.
- 5) To understand the electrochemical properties of the Ag/SnO<sub>2</sub>, Ag/ATO and Ag/AFTO catalysts.

## Chapter 2

### Theory and Literature Reviews

#### 2.1 Tin (IV) Oxide

Tin (IV) oxide or stannic oxide with the formula  $\text{SnO}_2$  is the inorganic compound. Tin oxide is the colorless, diamagnetic and amphoteric substance. The principal properties of  $\text{SnO}_2$  are shown in table 2.1.

Table 2.1 Physical properties of  $\text{SnO}_2$  [21]

Chemical formula	$\text{SnO}_2$
Crystal structure	Rutile
Lattice constant (Å)	$a = 4.737$ , $c = 3.185$
Density ( $\text{g/cm}^3$ )	6.99
Band gap [eV]	3.6
Appearance	White or light grey powder
Molar mass ( $\text{g}\cdot\text{mol}^{-1}$ )	150.71
Melting point ( $^{\circ}\text{C}$ )	1,630
Boiling point ( $^{\circ}\text{C}$ )	1,900

The crystallization of  $\text{SnO}_2$  is tetragonal rutile structure as shown in Figure 2.1. It is an n-type semiconductor with a direct band gap of approximately 3.6 eV. The high electrical conductivity and optical transparency are the major prominent physical properties of  $\text{SnO}_2$ . Therefore,  $\text{SnO}_2$  or impurity doped  $\text{SnO}_2$  are widely utilized as transparent conducting oxides (TCOs). Otherwise,  $\text{SnO}_2$  is also used as support catalyst material for electrochemical reaction. Usually, metal catalysts such as Pt or Pd could be dispersed on the surface of  $\text{SnO}_2$  to exhibit catalytic activity or display by

This material is reserved for educational use only, not allowed for commercial use.

Forbidden to modify the content, and cite the document when use.

themselves. The active surface area of some metal catalysts in the oxidation reaction was increased rather than the pure metal catalyst. Moreover, the excellent properties of  $\text{SnO}_2$  such as acidic-basic, oxidizing-reducing properties and the variation of the oxidation states in  $\text{SnO}_2$  has a significant importance in catalysis properties of  $\text{SnO}_2$ . Furthermore, it can act as an active heterogeneous catalyst for many organic reactions [21-22].

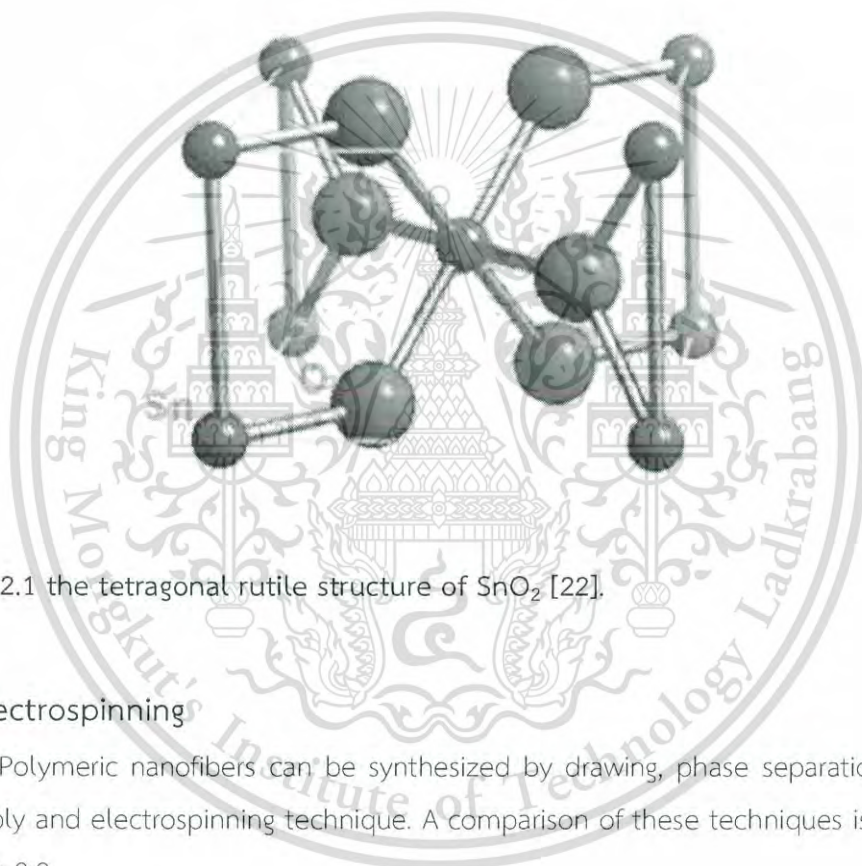


Figure 2.1 the tetragonal rutile structure of  $\text{SnO}_2$  [22].

## 2.2 Electrospinning

Polymeric nanofibers can be synthesized by drawing, phase separation, self-assembly and electrospinning technique. A comparison of these techniques is shown in table 2.2.

From table 2.2, electrospinning technique has advantage over other methods. It can be employed to synthesize the long nanofibers of polymer with continuous process with cost effectiveness. Furthermore, it is a simple method that can control dimension of the obtained nanofibers. Several polymers and salt precursors can be used in the synthesis process to fabricate fibers by electrospinning technique. Polymers nanofibers can be directly synthesized whereas ceramics require calcination process for the electrospun fibers to release the polymer template.

This material is reserved for educational use only, not allowed for commercial use.

Forbidden to modify the content, and cite the document when use.

Table 2.2 Comparison of processing techniques for synthesis polymer nanofibers [23]

Process	Repeatability	Convenient to process	Control fiber dimensions
Drawing	√	√	×
Phase separation	√	√	×
Self-assembly	√	×	×
electrospinning	√	√	√

Electrospinning is a process using electrical force to form electrostatic fiber. The precursor solution can be prepared by dissolving the polymer in the suitable solvent. Finally, the obtained smooth polymer fibers could have the diameters from nanometer to micrometer with larger surface area. In general, a power supply is a necessary component that produces a direct voltage of several tens kilovolts to generate the polymer nanofibers as shown in figure 2.2 depicting a schematic diagram of the electrospinning system.

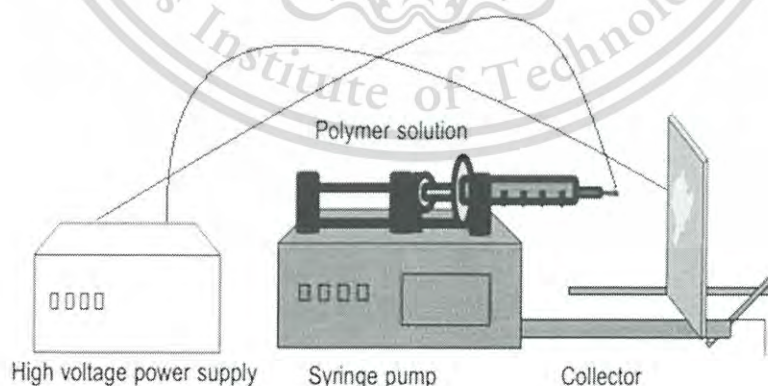


Figure 2.2 Schematic diagram of the electrospinning system.

Typically, an electrospinning system is set up with three major components and operated at ambient temperature with atmosphere pressure: a power supply generates high voltage, a syringe contains polymer solution with a metal tip and a conductive collector supports the electrospun fibers. Basically, the electric field is conducted between the metal tip and the collector. The surface tension of polymer solution at the metal tip is subjected to an electric field and the charge of surface polymer solution is induced by this electric field. When the electric field is increased to the critical value, the electrical forces overcome the surface tension forces of the polymer solution. The surface of solution at the tip forms the Taylor cone and ejected from a metal tip toward to the opposite charged collector in the air while the solvent was rapidly evaporated. Thus, the continuous polymer fibers can be collected on the metal collector [24-26].

The transformation of electrospun solution in liquid phase under the high electric field is described by the Taylor Cone theory [27]. At the beginning, the electrically liquid phase is controlled by an electric field. If the potential is less than critical value, the stable shape of conductive liquid will be generated under the equilibrium of the electric forces and the surface tension. As the voltage is enlarged to the critical potential, the equilibrium of the electric forces and the surface tension will be destroyed. Finally, the conductive liquid shape achieves a conical shape as the Taylor Cone.

The obtained electrospun fibers is in form of one-dimensional structure that can provide relatively high surface area to volume ratio accompanying small pore size which making them excellent candidates for use in electrocatalyst applications. The structure and the morphology of as-spun nanofibers are highly dependent on process parameters of electrospinning such as solution properties, applied voltage, control rate of polymer solution and the distance between the metal tip and the collector. It is found that the solution properties play a key role on the transformation of inorganic-organic solution into as-spun nanofibers. In general, the electrospun solution of polymer and inorganic precursor has to be considered to optimize the viscosity of solution jet.

During the electrospinning process, the important role of the fiber formation is the concentration of polymer solution. It can be explained by dividing concentration in four critical levels from low to high concentration:

1. When the concentration of polymer solution is very low, the polymeric micro or nanoparticles will be obtained. It should be noted that electrospray may occur instead of electrospinning because of the low viscosity and high surface tension of the polymer solution.

2. When the concentration of polymer solution is increased, a mixture of polymeric beads and polymeric fibers will be achieved.

3. When the concentration of polymer solution is suitable, the smooth polymeric nanofibers can be obtained.

4. When the concentration of polymer solution is very excessive, the complicated micro or nanostructure will be observed.

Usually, preparation of the suitable concentration of polymer solution is the first priority for electrospinning process. The obtained fiber diameter could be varied with the concentration of polymer solution. If the concentration of polymer solution increases, the fiber diameter will grow up. Additionally, polymer solution viscosity can be also modulated by adjusting the polymer solution concentration. When the viscosity of polymer solution is low, the discontinuous and beaded fiber will be obtained. If the viscosity of the polymer solution is suitable, the continuous fibers can be achieved. On the other hand, the high viscosity of polymer solution results in the inconvenient ejection of jets to form the polymeric fibers. It can be concluded that solution viscosity, polymer concentration, and polymeric molecular weight are the main key in defining the fiber morphology and dimension in diameter.

The applied voltage is also a crucial factor for electrospinning process. When the sufficient voltage was adjusted to the polymer solution, charged jets will be ejected from Taylor Cone. Moreover, the flow rate of the polymer solution is another important process parameter. It has an influence in the morphology and size diameter of polymeric fibers. Generally, lower flow rate is insufficient to generate fibers. On the contrast, the high flow rate generates the bead fibers with thick diameter. By the way,

the distance between the tip and the collector is an important parameter to determine the morphology and diameter of electrospun fibers. This parameter is related to the dryness from the electrospun fibers. If the distance is too short, the solvent in the fiber will not have enough time to evaporate before reaching the collector, whereas if the distance is too long, the bead fiber can be obtained.

During the electrospinning process, the conductive collectors are normally used as a substrate to store the obtained fibers. Generally, aluminium foil is used as a collector whereas wire mesh, pin, grids, rotating rods or wheel, liquid bath could be applied for various applications.

The humidity can also affect the diameter and morphology of fibers. At low humidity, the solvent in fibers may rapidly evaporate before reaching to the collector. On the contrary, high humidity will lead to the thick fiber diameter [28-30].

### 2.3 Direct ethanol fuel cell

Fuel cells are electrochemical devices that convert the chemical reaction of fuels directly into electrical energy without combustion. They have electrical efficiencies and high fuel conversion than other power generation devices. A fuel cell is much cleaner than conventional energy sources because no intermediate combustion stage of chemical substance. Heat and water is the main product reused in the reverse of electrolysis. Fewer of toxic gas such as  $\text{NO}_x$ , ozone and particles are byproduct from chemical reaction [31]. The principles of the fuel cell are shown in Figure 2.3 [32]. The electrochemical cell consists of two electrodes which are electron conductors. Oxidation reaction is occurred at an anode electrode whereas reduction reaction is occurred at a cathode electrode. Each of electrodes is separated by a solid or liquid electrolyte which is an ion conductor. An elementary electrochemical cell changes a given fuel such as hydrogen, natural gas, hydrocarbons, alcohols or biomass resources into electricity energy. Free electrons are generated by the electro-oxidation reaction of the fuel pass through the external circuit and arrive at the cathode where reduction reaction of oxygen gases takes place. For many applications, hydrogen is not a primary fuel and many different masses such as water, natural gas or biomass

resources were used for hydrogen source. The difficulties with its storage and large-scale distribution are the limitations for the development of such techniques. Therefore, alcohols are alternative fuels because they are liquid substance at room temperature and pressure. They have a high energy density (methanol  $6.09 \text{ kW h kg}^{-1}$  and ethanol  $8.00 \text{ kW h kg}^{-1}$ ) and they can be obtained from renewable sources [32].

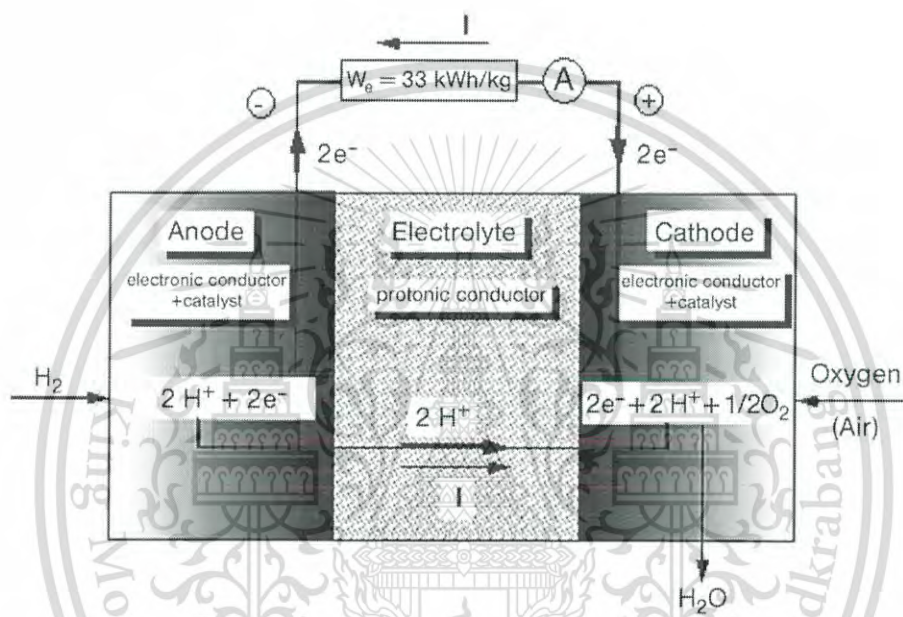


Figure 2.3 Schematic diagram of a hydrogen/oxygen fuel cell [32].

Direct alcohol fuel cells are storage power systems that use alcohol as liquid fuel. The usage of alcohol as liquid fuel has overcome obstacles about storage system. Liquid fuels have greater advantage than hydrogen fuel regarding the convenience of their transport and handling. The small organic molecules of alcohols have been considered as fuels in direct ethanol fuel cells. However, the main disadvantage of this alcohol is its high toxicity. Some liquid fuels such as ethanol and ethylene glycol are researched and are reconsidered as replacement of methanol. The electro-oxidation of ethanol and ethylene glycol are prone to be oxidized at ambient temperature with suitable catalysts. Ethanol is the most interesting alcohol for direct ethanol fuel cells

because of lower toxicity and higher energy density. Moreover, the dissociation of C-C bond in complete oxidation reaction of ethanol bring about to form only CO<sub>2</sub> [33].

Direct alcohol fuel cells are new sources of energy which the alcohol reacts directly at the anode of fuel cell without any reforming process. The notable alcohols that are used as fuels in DAFCs are methanol and ethanol. The direct methanol fuel cells (DMFCs) use methanol as fuel and operate at ambient temperature. Methanol is oxidized in the anode and releases electrons and protons. The electrons are transported through an external circuit to the cathode while the protons enter the electrolyte membrane to the cathode. Oxygen from the air reacts with the electrons and protons and generates water. The electrochemical reaction is shown in equation (1) to (3): [34]



The direct methanol fuel cells have the advantages of high energy density, non-pollutant byproducts, and ease of operation. However, there are the three major obstacles of DMFC in an industrialized process. First, the methanol oxidation reactions are not fast enough. Second, methanol diffuses crossover from the anode to cathode. Third, methanol is a toxic fuel which has an effect on the human optical nerve. To overcome these issues about methanol as fuel, ethanol is a very attractive substitute since it has a higher energy density and non-toxic alcohol. It can be easily produced from agriculture or biomass source.

Table 2.3 shows considerable advantages of ethanol over hydrogen and methanol as fuels. Ethanol has lower toxicity, higher efficiency, higher energy density and ease of storage and transportation. Especially, ethanol can be produced from sugar resources such as wheat, corn, or cellulose. Thus, ethanol may be a substantial energy source in the future technology.

Table 2.3 Comparison of different fuels in a direct fuel cell [33]

	Hydrogen	Methanol	Ethanol
Energy Density (kW h kg <sup>-1</sup> )	0.42	6.1	8.0
Boiling Point (°C)	-253	65	78
Hazard	Flammable	Very toxic	Non-toxic
Storage	Difficult	Easy	Easy
Sources	Fossil fuels	Fossil fuels	sugar

In direct ethanol fuel cells (DEFC), ethanol is directly fed to the anode of the fuel cell, and the air is provided to the cathode of the cell (Figure 2.4). Ethanol is oxidized to form protons, carbon dioxide and electrons. The protons are transported through the membrane, and electrons flow through the electrical circuit. At the cathode, protons react with oxygen in air and form water. The electrochemical reactions can be written as follows.



The success ethanol electro-oxidation relates to 12 electrons per molecule and many intermediates with different catalytic surfaces or in different media are generated through different pathways. Thus, it is more difficult to clarify exactly the mechanism of ethanol electro-oxidation. In fact, the primary disadvantage of DEFC is the lack of a catalyst that can initiate complete electro-oxidation of ethanol. Platinum (Pt) is a suitable catalyst with high activity and stability for electro-oxidation of ethanol. However, pure platinum is not an appropriate anode catalyst for ethanol or methanol electro-oxidation at ambient temperature because it is absolutely poisoned by the adsorbed intermediates. To overcome this drawback, ethanol is almost completely

oxidized into carbon dioxide and producing 12 electrons via a single electro-oxidation reaction with binary alloys and intermetallics of platinum [35].

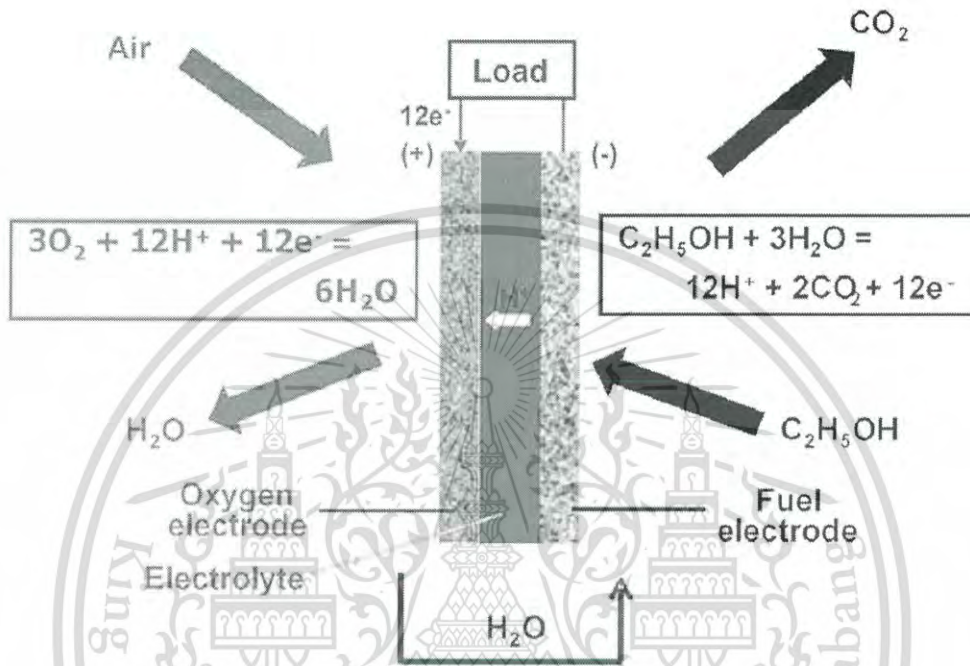
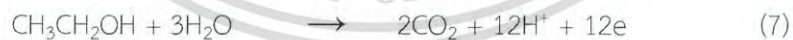


Figure 2.4 Schematic diagram of a direct ethanol fuel cell [31].

Two pathway mechanisms on Pt based catalysts for ethanol oxidation reaction can be described as following equation:



The first pathway is the complete oxidation of ethanol shown in equation 7. It can suggest that one mole of ethanol can produce twelve moles of electron and two moles of carbon dioxide ( $\text{CO}_2$ ) which are the main products of the complete oxidation of ethanol.



The second pathway is the partial oxidation of ethanol. One mole of ethanol can be oxidized to provide acetic acid and four electrons or to acetaldehyde and two electrons as expressed in equation 8 and 9, respectively. The partial oxidation of ethanol can be occurred without the cleavage of the C–C bond that generates a few electrons to the circuit. During ethanol oxidation reaction, intermediates such as CO or  $\text{CH}_x$  which has one carbon atom is occurred and adsorbed at the Pt surface that results in the reduction of charge transfer rate of the ethanol oxidation reaction. Therefore, modifying Pt with secondary species could release the poisoning of adsorbed reaction and improve the kinetic of ethanol oxidation reaction and complete oxidation of ethanol into  $\text{CO}_2$  [36].

The development and design of efficient catalysts for breaking the C–C bond during ethanol electrooxidation is a central question in electrocatalysis. Many factors are known to have an influence in catalyst activity and selectivity such as chemical composition, morphology, size and shape of the catalyst in addition to the reaction conditions. Therefore, the precise control of these parameters is crucial for the rational design of efficient and stable electrocatalysts for DEFCs. Catalyst supports are reported to play a significant role towards morphology, dispersion, activity, and selectivity of the catalysts. There are several reports showing the application of metal oxide supports such as  $\text{CeO}_2$ ,  $\text{SnO}_2$ ,  $\text{TiO}_2$ ,  $\text{Mn}_x\text{O}_y$ ,  $\text{WO}_x$ ,  $\text{MoO}_x$ ,  $\text{RuO}_2$ ,  $\text{ZrO}_2$ ,  $\text{CaSiO}_2$ ,  $\text{MgO}$ , and  $\text{CoO}_x$  as promising supports for EOR catalysts. These metal oxide supports have a significant effect on the catalytic activity of the catalysts because of the interaction phenomenon known as “strong metal-support interaction” which was recognized by Tauster *et al.*

## 2.4 Cyclic voltammetry

Voltammetry is an electro-analytical technique in which measurement of current as a function of applied potential is related to the analytical information. It is widely used to study the redox processes, adsorption processes on surfaces, electron transfer mechanisms and electrode kinetics.

Cyclic voltammetry is a potential sweep technique. The cyclic scan is operated by sweeping the electrode potential between the lowest potential to the highest potential. At the beginning, the electrode is applied from the lowest potential to the highest potential which is called “forward scan”. After that, the sweep is reversed from the highest potential to the lowest potential which is called “backward scan”. The Cyclic voltammogram is plotted between current versus potential. It indicates that the potential is related to the redox reaction of the analyte.

The current measured during this process is usually normalized to the electrode surface area which is referred to the current density. Therefore, a cyclic voltammogram can be plotted between the current density versus the applied potential. The measuring current is seen at the peculiar potential that is characteristic of any electrode reaction taking place. For a particular process, the sweep rate, electrolyte concentration and the electrode material affect to the peak width and peak height. The cyclic voltammogram in Figure 2.5 describes a redox process. When the potential is applied to the positive direction, the active species will lose an electron at the electrode. Suddenly, an oxidation peak at a given potential ( $E_{pa}$ ) occurs and gives an anodic peak current ( $i_{pa}$ ). Subsequently, the potential is applied in the negative direction. A reduction process will occur at the electrode giving a cathodic currents ( $i_{pc}$ ) at a given potential ( $E_{pc}$ ). Typically, the cyclic voltammetry is initiated at a potential where the active species are unresponsiveness.

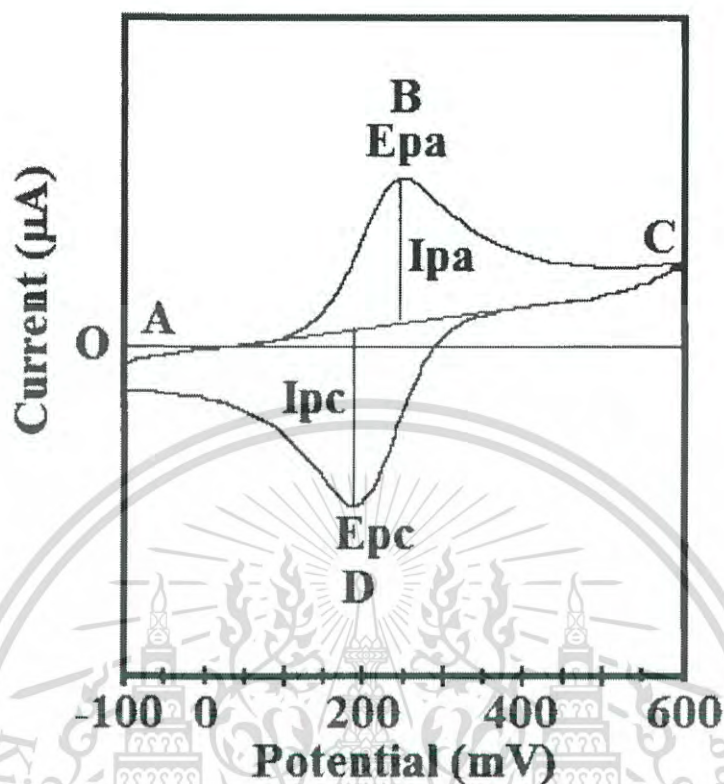


Figure 2.5 A typical cyclic voltammogram of current versus potential.

The principle equipment required to operate cyclic voltammetry consists of a traditional three-electrode potentiostat connected to three electrodes (working, reference and counter electrode) immersed in an electrolyte testing solution. The potential is applied by the potentiostat between the working and reference electrode while measuring the current at the working electrode. Charge flows between the working electrode and the counter electrode. A recording device is used to record the resulting cyclic voltammogram as a plot of current versus potential.

## 2.5 Literature Reviews

L. Cheng *et al.* [37] synthesized SnO<sub>2</sub> hollow nanofibers with a porous structure by electrospinning technique and calcination procedure. Tin chloride dihydrate (SnCl<sub>2</sub>·2H<sub>2</sub>O) and PolyVinylPyrrolidone (PVP,  $M_w = 1,300,000$ ) was used as starting

material. Tin precursor was dissolved with N,N-dimethylformamide (DMF) while polymer precursor was dissolved with ethanol. Both of them were mixed and stirred until the homogeneous solution was obtained. The PVP/  $\text{SnCl}_2 \cdot 2\text{H}_2\text{O}$  composite were calcined at  $600^\circ\text{C}$  for 2 hours. The SEM image (up) and XRD pattern (below) in Figure 2.6 shows the obtained  $\text{SnO}_2$  fibers having hollow nanofibers structures with the average diameter of 200 nm which is indexed to rutile structure of  $\text{SnO}_2$ .



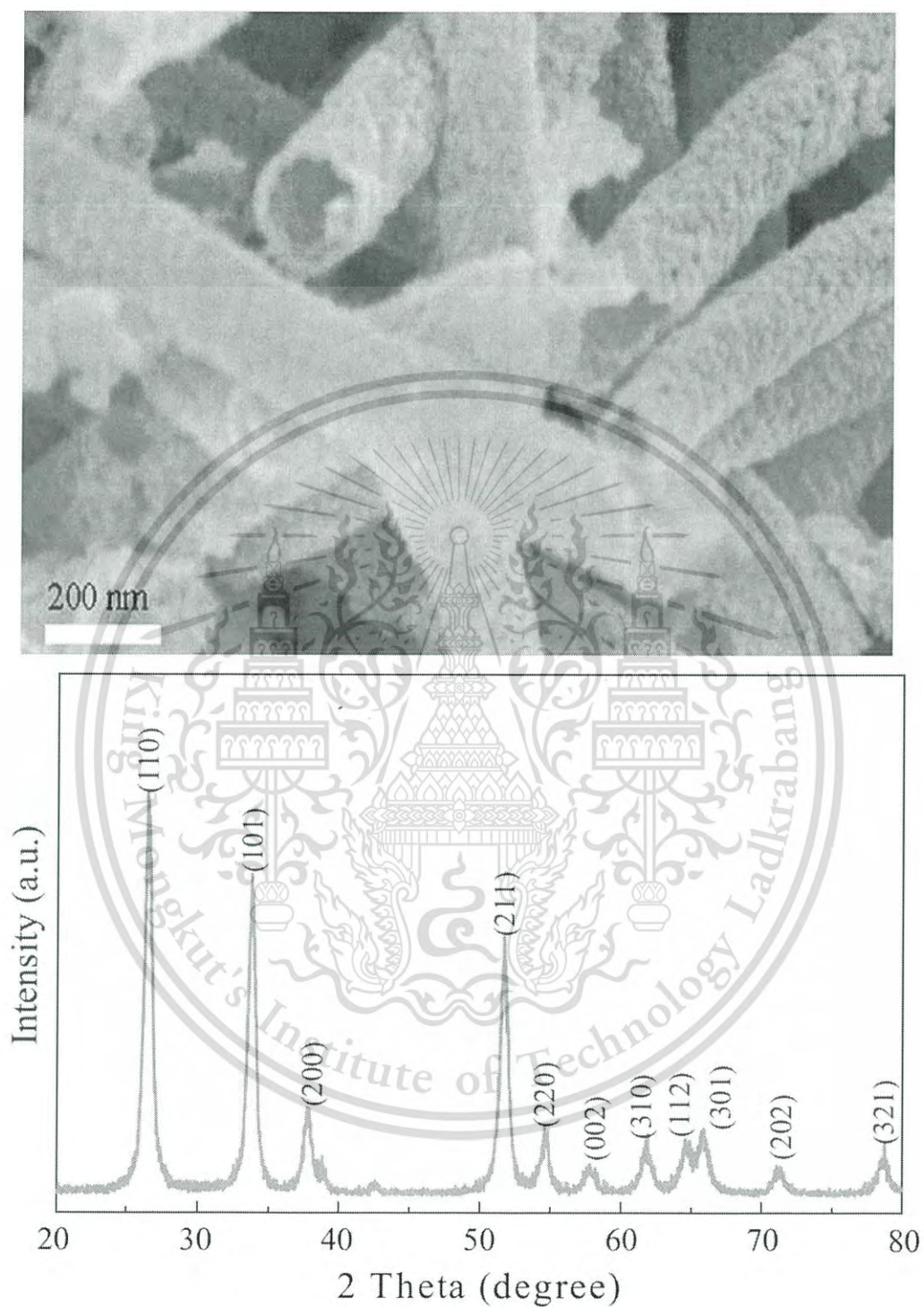


Figure 2.6 (up) SEM image and (below) XRD patterns of SnO<sub>2</sub> hollow nanofibers [37].

L. Li *et al.* [38] synthesized SnO<sub>2</sub> nanotubes with a porous structure via electrospinning technique followed by calcination in the air. PVP ( $M_w=30,000$ ) and SnCl<sub>4</sub>·5H<sub>2</sub>O was dissolved in ethanol for preparing electrospun solution. The voltage of 20 kV was applied between the tip of needle and the aluminum surface to the electrospun solution. The fibers mat was dried at 60°C for 24 hours under vacuum. The obtained product was calcined at 500°C for 3 hours with a heating rate of 2.8°C/min. Figure 2.7 shows the rough surface of SnO<sub>2</sub> nanotubes with an average diameter of 220 nm obtained after calcination process. The crystalline phase existing in the obtained nanotubes was the tetragonal rutile phase of SnO<sub>2</sub>.

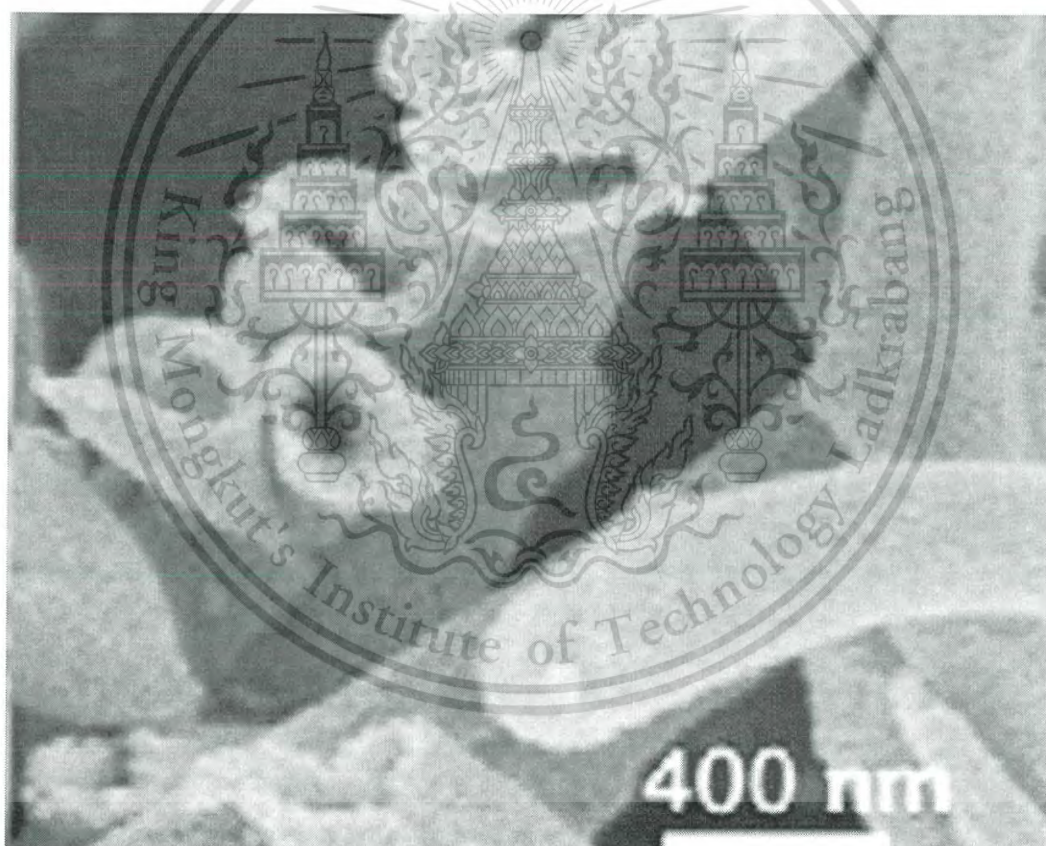


Figure 2.7 SEM image of SnO<sub>2</sub> nanotubes [38].

W.Q. Li *et al.* [39] synthesized hollow SnO<sub>2</sub> nanobelts through a single capillary electrospinning method. Typically, PVP was dissolved in ethanol and SnCl<sub>2</sub>·2H<sub>2</sub>O was

This material is reserved for educational use only, not allowed for commercial use.

Forbidden to modify the content, and cite the document when use.

dissolved in DMF. Two solutions were mixed and stirred for 2 hours at 40°C until the obtained solution was homogeneous. The voltage of 3.4 kV was applied between the needle and collector at a distance of 15 cm. The fiber mat was calcined in a furnace at 600°C for 1.5 hours. Figure 2.8 shows the thin and uniform SnO<sub>2</sub> nanobelts with concave-convex and porous surface. The average diameter of the SnO<sub>2</sub> nanobelts was 140 nm.

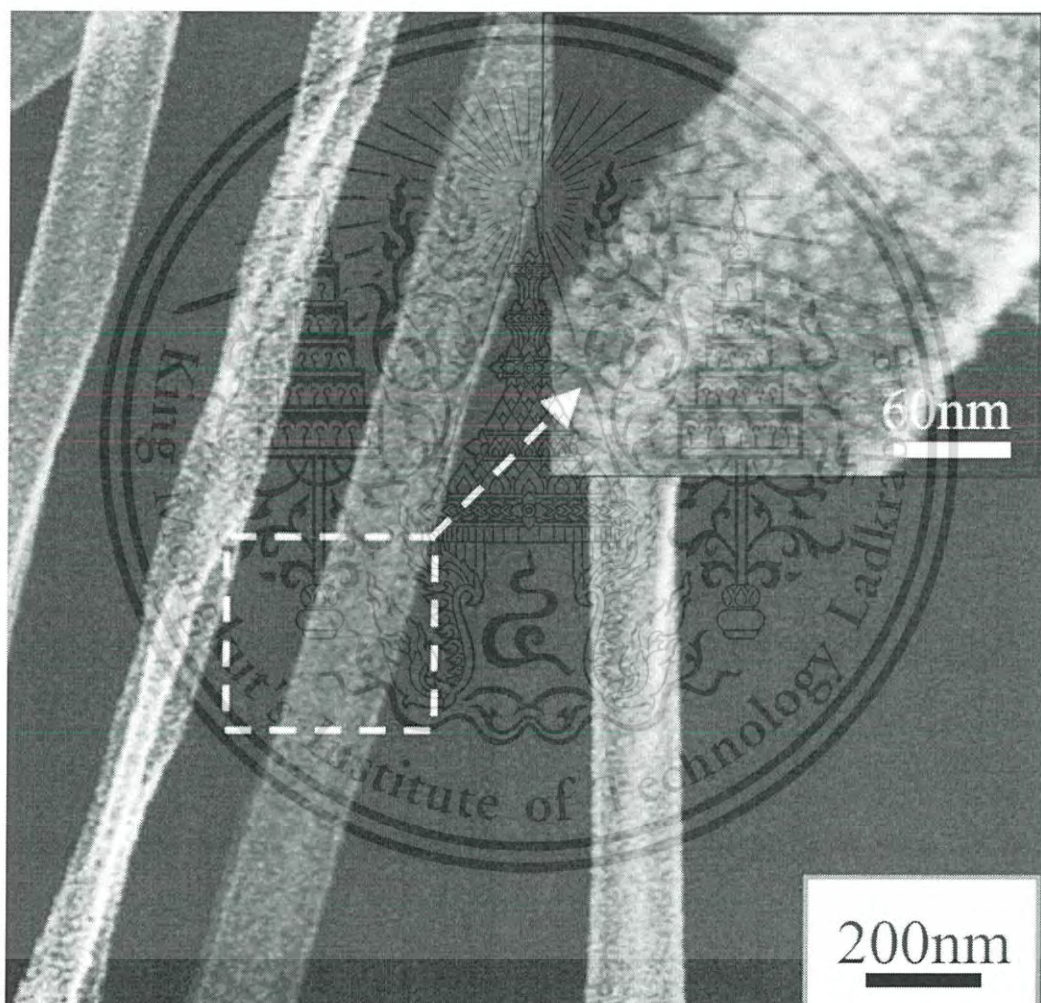


Figure 2.8 SEM image of SnO<sub>2</sub> nanobelts [39].

Y. Zhang *et al.* [40] synthesized SnO<sub>2</sub> fibers with a porous structure by electrospinning process and oxygen plasma etching. The electrospun solution is PVA

This material is reserved for educational use only, not allowed for commercial use.

Forbidden to modify the content, and cite the document when use.

( $M_w = 80,000$  g/mol) / $\text{SnCl}_4 \cdot 5\text{H}_2\text{O}$  composite that was dissolved in deionized water. The electrospinning process was set up at the angle of the syringe to horizontal was  $60^\circ$  and the needle tip-to-collector distance was kept at 1.5 cm while the voltage of 8 kV was applied. The obtained fibers were dried for 24 h at  $80^\circ\text{C}$  followed by a plasma treatment which oxygen gas was used as the reactant. At last, annealing process at  $500^\circ\text{C}$  for 4 hours was carried out to obtain the highly porous  $\text{SnO}_2$  fibers as shown in Figure 2.9.

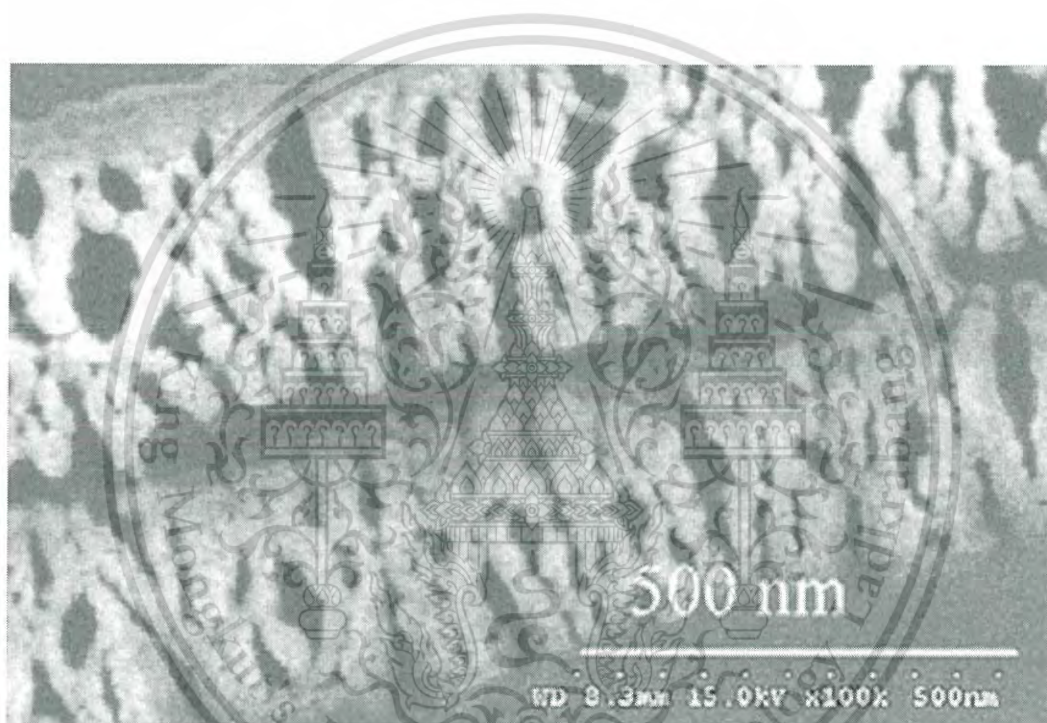


Figure 2.9 SEM image of porous  $\text{SnO}_2$  fibers [40].

X. Wang *et al.* [41] synthesized hollow  $\text{SnO}_2$  microtubes (MTs) by electrospinning technique.  $\text{SnCl}_2 \cdot 2\text{H}_2\text{O}$  and PVP ( $M_w = 58,000$ ) were used as starting materials for preparing electrospun solution. PVP and  $\text{SnCl}_2 \cdot 2\text{H}_2\text{O}$  was separately dissolved with deionized water and absolute ethanol, respectively. The tin precursor solution was added to the polymer solution and stirred until the solution was homogeneous. The obtained solution was filled into Teflon capillary with controlled flow rate of 3 ml/h and the capillary was 10 cm from the Al collector. The white

This material is reserved for educational use only, not allowed for commercial use.

Forbidden to modify the content, and cite the document when use.

products electrospun fibers were produced under a high voltage of 30 kV then were collected on the plate. Finally, the SnO<sub>2</sub> hollow microtubes were achieved by annealing at 600°C with heating rate of 2°C min<sup>-1</sup> for 2 hours. Figure 2.10 reveals the SEM image of SnO<sub>2</sub> hollow microtubes with the rough porous surface.



Figure 2.10 SEM image of SnO<sub>2</sub> hollow microtubes [41].

Y.-E. Miao *et al.* [42] synthesized Ag/SnO<sub>2</sub> composite nanotubes by electrospinning technique. PVP, SnCl<sub>2</sub>·2H<sub>2</sub>O and AgNO<sub>3</sub> were used as starting materials. Mixing solution of DMF and ethanol was utilized for preparing electrospun solution by dissolving PVP/SnCl<sub>2</sub>·2H<sub>2</sub>O and stirring until homogeneous solution was reached. The electrospinning parameter was set up as an electrical potential of 15 kV and a speed solution of 1.5 mL h<sup>-1</sup> with a distance of 15 cm between the needle tip and the aluminum foil collector. The obtained fibers were calcined at 600°C in air for 3 hours. The Ag/SnO<sub>2</sub> composite nanotubes were prepared by mixing SnO<sub>2</sub> nanotubes in AgNO<sub>3</sub> solution and irradiated with mercury lamp for 2 h to reduce Ag<sup>+</sup> to Ag. The obtained composite fibers is shown in Figure 2.11.

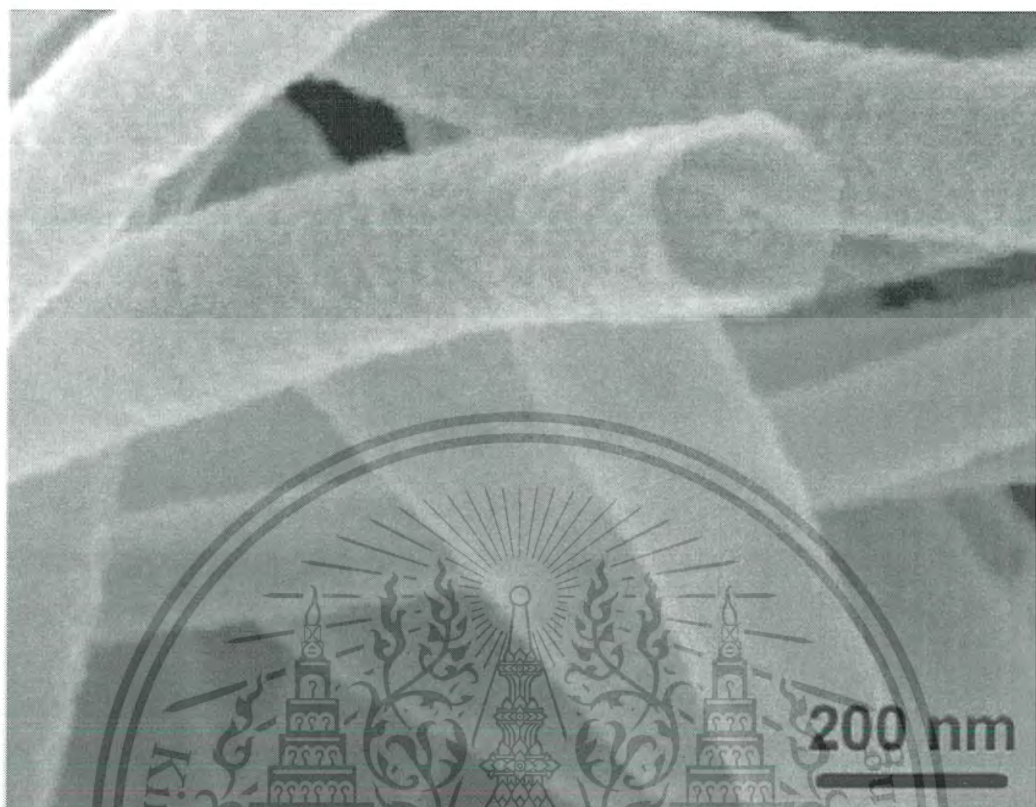


Figure 2.12 SEM image of SnO<sub>2</sub>-core carbon-shell composite nanotubes [43].

A. B. Suryamas *et al.* [44] synthesized Pt/SnO<sub>2</sub> nanofibers by an electrospinning technique. Polyacrylonitrile (PAN,  $M_w=150,000$ ) was used as the polymer template. Tin chloride pentahydrate (SnCl<sub>4</sub>·5H<sub>2</sub>O) and hexachloroplatinic acid (H<sub>2</sub>PtCl<sub>6</sub>·6H<sub>2</sub>O) were used as starting precursors for Sn and Pt, respectively. N,N-dimethylformamide (DMF) was utilized to prepare the electrospun solution. The voltage was set up at 14 kV with the length between needle tip and electrode about 23 cm. The flow rate of the precursor solution and rotation drum velocity was 20  $\mu$ l/min and 450 rpm, respectively. The obtained composite nanofibers were calcined at 500°C with a heating rate of 2°C/min for 4 hours in air. The obtained Pt/SnO<sub>2</sub> nanofibers had crystallite size of 23.74 nm and the rough porous surface as shown in Figure 2.13.

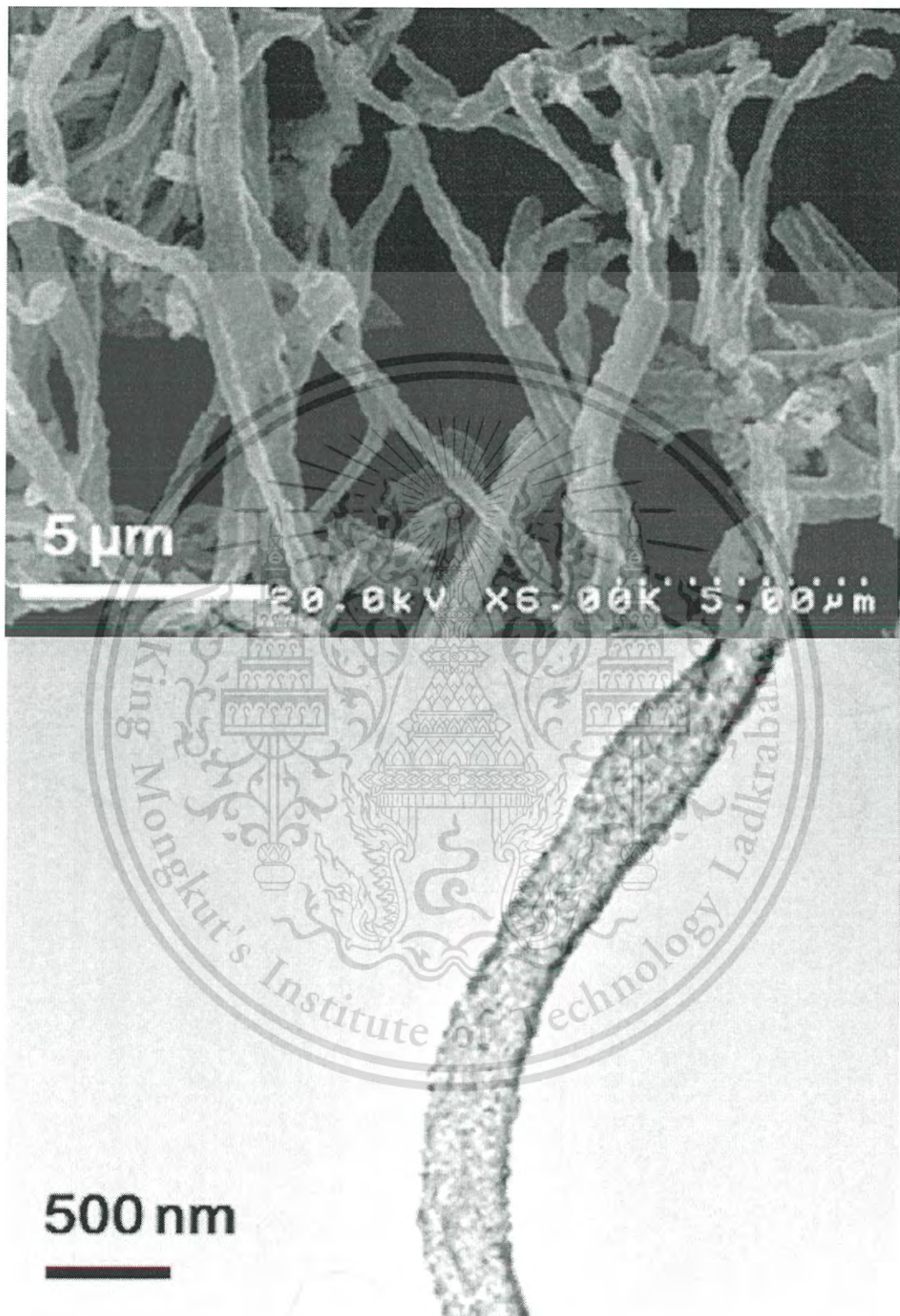


Figure 2.13 (up) FE-SEM image, (below) TEM image of Pt/SnO<sub>2</sub> nanofibers [44].

This material is reserved for educational use only, not allowed for commercial use.

Forbidden to modify the content, and cite the document when use.

X. Wang *et al.* [45] prepared Ag/SnO<sub>2</sub> heterostructures via a simple microwave hydrothermal process. The mixture of alkali solution of tin (II) chloride dihydrate (SnCl<sub>2</sub>·2H<sub>2</sub>O), sodium citrate (Na<sub>3</sub>C<sub>6</sub>H<sub>5</sub>O<sub>7</sub>·2H<sub>2</sub>O) and silver nitrate (AgNO<sub>3</sub>) were used as starting precursors. The hydrothermal condition was set up at the power of 400 W with the temperature at 200°C for 1 hour. Subsequently, the obtained precipitate product was dried at 80°C for several hours and annealed in a muffle furnace at 600°C for 2 hours. Figure 2.14 shows the SEM image of the Ag/SnO<sub>2</sub> heterostructures which look like nanoflowers constructed from aggregate of nanoplates. Moreover, some small nanospheres are attached on the formed nanoflowers.

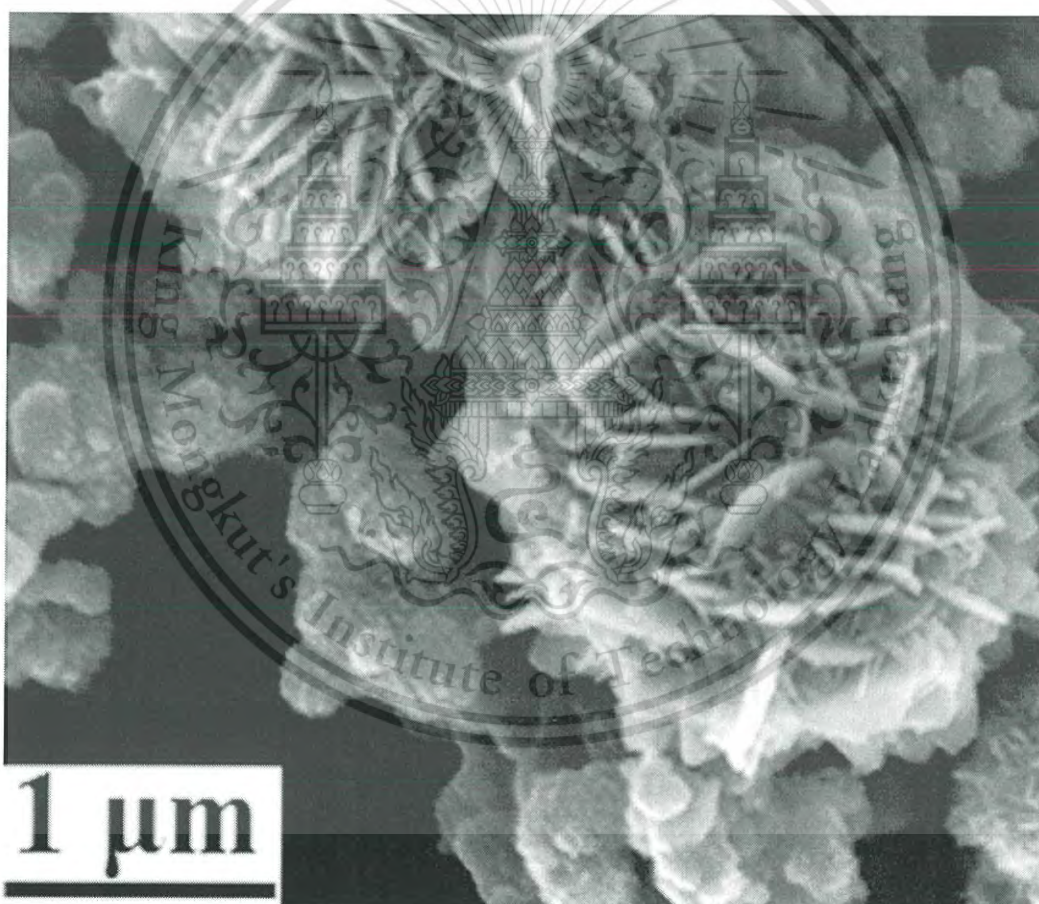


Figure 2.14 SEM images of the Ag/SnO<sub>2</sub> heterostructures [45].

F. Zhang *et al.* [46] synthesized Hierarchical structures of Ag nanoparticles grown on TiO<sub>2</sub> fibers by combining electrospinning techniques and hydrothermal

This material is reserved for educational use only, not allowed for commercial use.

Forbidden to modify the content, and cite the document when use.

process. The anatase  $\text{TiO}_2$  fibers were immersed in the mixed  $\text{AgNO}_3$  and HMTA ( $\text{C}_6\text{H}_{12}\text{N}_4$ ) aqueous solution in a batch reactor at  $90^\circ\text{C}$  for 10 hours. Figure 2.15 shows SEM image (A) of pure  $\text{TiO}_2$  fibers synthesized by electrospinning technique and SEM image (B) showing the  $\text{Ag}/\text{TiO}_2$  fibers synthesized by hydrothermal process. TEM image (C) and (D) exhibit the  $\text{TiO}_2$  fibers and the  $\text{Ag}/\text{TiO}_2$  fibers, respectively. It can conclude that an electrospinning technique can produce the  $\text{TiO}_2$  fibers, which have a large specific surface area and provide an area for the deposition of Ag crystal nucleus. After hydrothermal process, Ag crystal nucleus grown in the direction on the active surface are attached on the surface of  $\text{TiO}_2$  fibers.

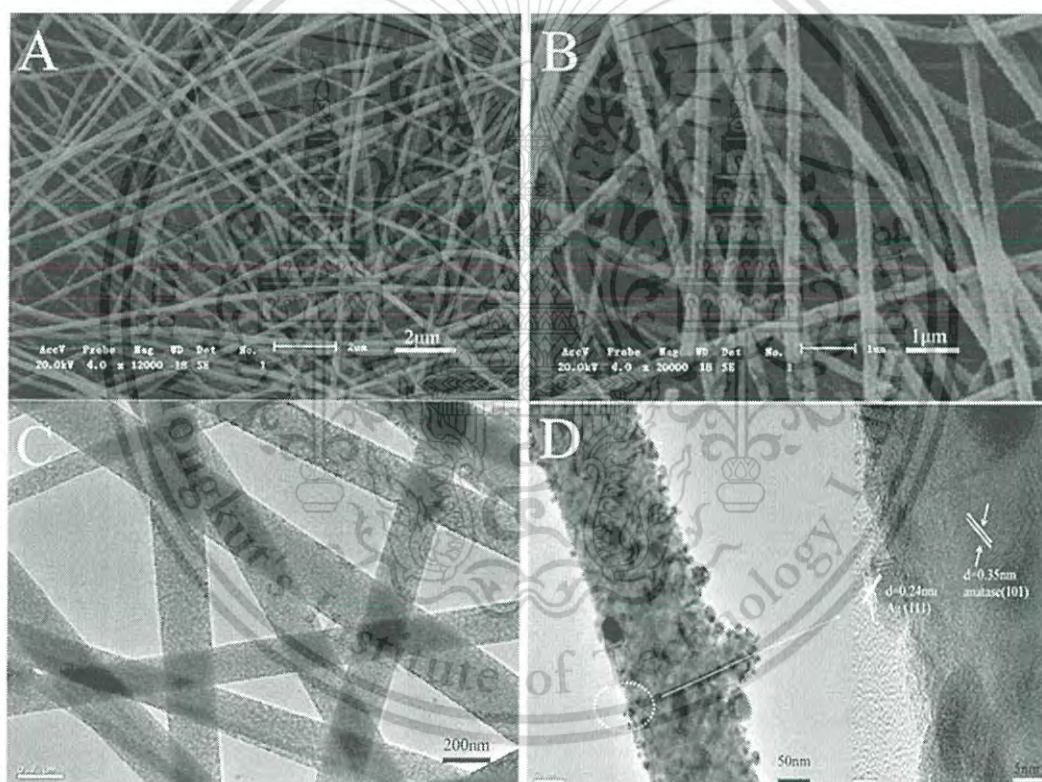


Figure 2.15 (A) SEM image of Pure  $\text{TiO}_2$  fibers; (B) SEM image of  $\text{Ag}/\text{TiO}_2$ ; (C) TEM image of  $\text{TiO}_2$  fibers; (D) TEM images of the  $\text{Ag}/\text{TiO}_2$  fibers [46].

D.-J. Guo [47] fabricated multi-walled carbon nanotubes supported platinum-antimony tin oxide (Pt-ATO/MWCNT) on a gold electrode ( $1 \text{ cm}^2$ ) for investigating the ethanol electrooxidation reactions in acidic medium. The ATO/MWCNT composites

were synthesized by mixing  $\text{SnCl}_4 \cdot 5\text{H}_2\text{O}$ ,  $\text{SbCl}_3$  and MWCNTs in hydrochloric (HCl) solution. After that, sodium hydroxide (NaOH) was added in the acidic solution until pH 10 and moved to reflux at  $100^\circ\text{C}$  for 2 hours in inert atmosphere. The obtained solid was calcined at  $400^\circ\text{C}$  for 1 hour in ambient air. The Pt nanoparticles were synthesized based on the polyol method using ethylene glycol as a stabilizer and reducing agent. The ATO/MWCNT composites were mixed with the Pt suspension solution to achieve the Pt-ATO/MWCNT catalysts. Cyclic voltammetry (CV) test was operated at  $50 \text{ mV s}^{-1}$  with a potential ranging from  $-0.2$  to  $1.4 \text{ V}$  in a mixture solution of  $1 \text{ M H}_2\text{SO}_4$  and  $1 \text{ M CH}_3\text{CH}_2\text{OH}$ . The morphologies of these catalysts showed the uniform distribution of Pt and ATO which has diameter of about  $3\text{--}8 \text{ nm}$  on the surface of the MWCNTs. Figure 2.16 shows cyclic voltammograms (up) of various electrodes which has the peak current densities of tethanol oxidation activity at  $0.70 \text{ V}$  of  $1300$ ,  $1198$ , and  $1036 \text{ mA mg}^{-1} \text{ Pt}$ , for Pt-ATO/MWCNT, Pt-SnO<sub>2</sub>/MWCNT, and Pt/C respectively. The steady-state current densities in the chronoamperograms (below) at  $3600 \text{ s}$  for Pt-ATO/MWCNT, Pt-SnO<sub>2</sub>/MWCNT, and Pt/C are  $63$ ,  $32$ , and  $17 \text{ mA mg}^{-1}$ , respectively. It could be suggested that the ATO/MWCNT as supporter for a Pt catalyst was increased the electrocatalytic activities of the catalyst for ethanol oxidation.

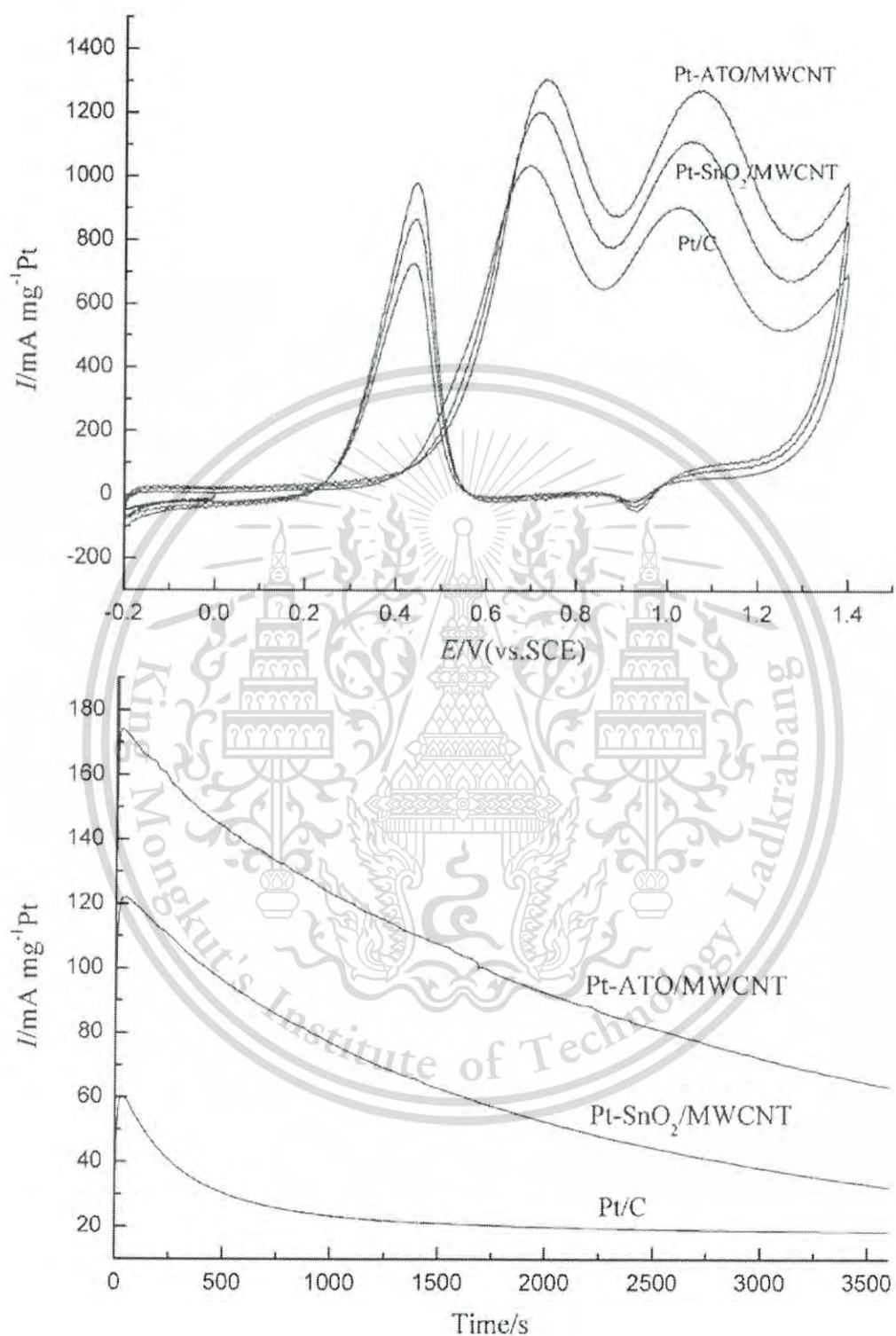


Figure 2.16 (up) cyclic voltammograms and (below) chronoamperograms of various electrodes [47].

This material is reserved for educational use only, not allowed for commercial use.

Forbidden to modify the content, and cite the document when use.

C. Pan *et al.* [48] synthesized Sb-doped SnO<sub>2</sub> supported carbon black (ATO/C) composites by co-precipitation method. SnCl<sub>4</sub>·5H<sub>2</sub>O, SbCl<sub>3</sub> and carbon black were mixed with anhydrous alcohol and NH<sub>3</sub>·H<sub>2</sub>O was dropped to the solution until the pH reached 9. The obtained solid was calcined at 600°C for 2 hours in air. The Pt-ATO/C nanoparticles were prepared by polyol method using H<sub>2</sub>PtCl<sub>6</sub>·xH<sub>2</sub>O as Pt starting material. A working electrode for investigating the activity of the catalyst for the methanol oxidation reaction were fabricated by mixing Pt-ATO/C nanoparticles with de-ionized water, 2-propanol, and 5wt.% Nafion solution then dropping it onto a glassy carbon (GC) electrodes. The Pt-ATO particles were distributed on the carbon-black support with an average diameter of 15 and 8 nm for ATO and Pt particles, respectively. The minimum resistivity of ATO about 2.29 Ω·cm was obtained at the Sb doping concentration of 5% as expressed in Figure 2.17. Cyclic voltammograms of various electrodes at 50 mV s<sup>-1</sup> in 1.0 M H<sub>2</sub>SO<sub>4</sub> + 1.0 M CH<sub>3</sub>OH aqueous solution is shown in Fig 2.18. It was found that the peak currents due to methanol oxidation for Pt-ATO/C, Pt-SnO<sub>2</sub>/C and the Pt/C catalyst are 8.9, 5.9 and 3.5 mA·cm<sup>-2</sup>, respectively.

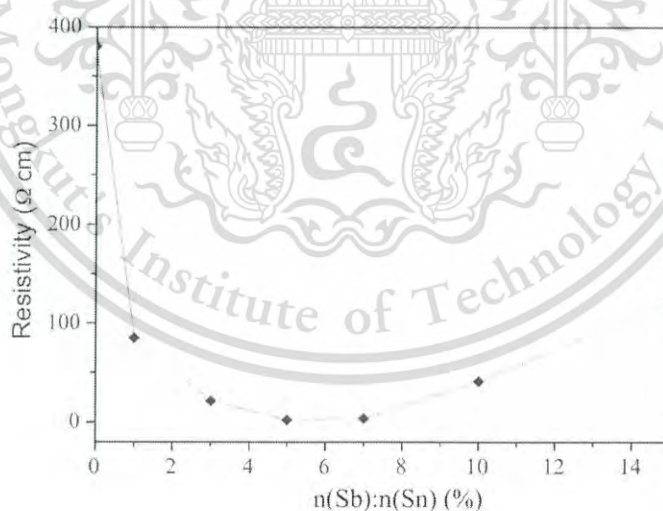


Figure 2.17 Resistivity of ATO with different Sb dopants [48].

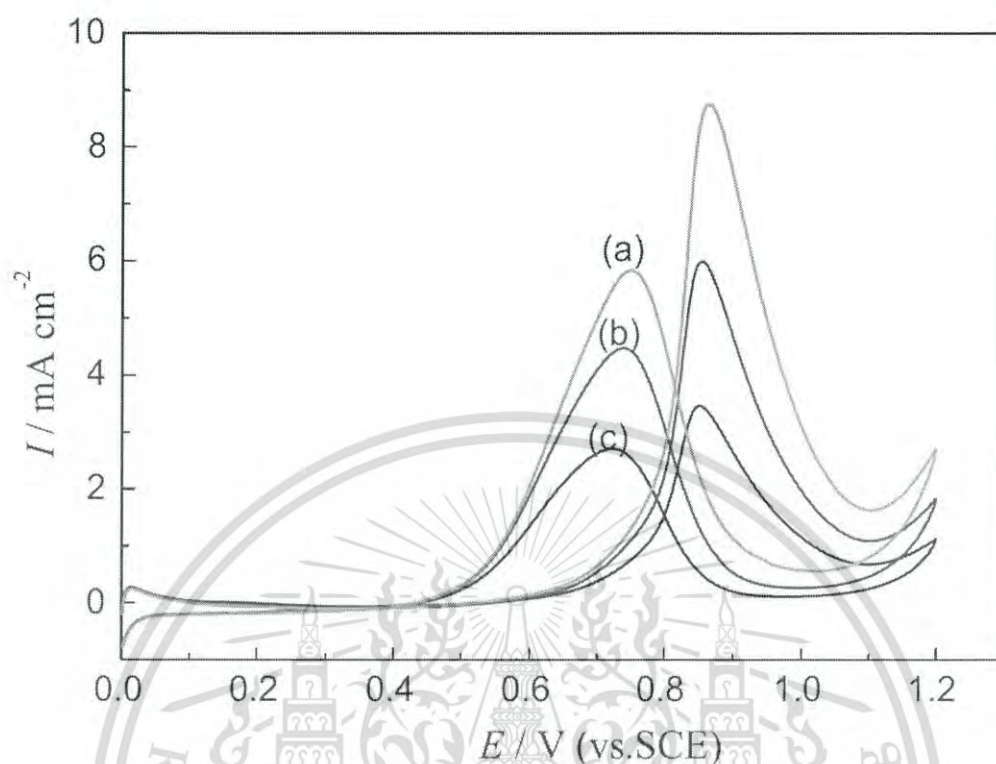


Figure 2.18 cyclic voltammograms of (a) Pt-ATO/C, (b) Pt-SnO<sub>2</sub>/C, and (c) Pt/C in 1.0 M H<sub>2</sub>SO<sub>4</sub> + 1.0 M CH<sub>3</sub>OH aqueous solution [48].

J. Flórez-Montaño *et al.* [49] studied the electrochemical behavior and mass spectrometric features for ethanol reactions on nanostructured mesoporous platinum catalysts in acidic medium. Figure 2.18 shows the mechanism of the ethanol oxidation reaction on Pt catalysts in H<sub>2</sub>SO<sub>4</sub> solution. It can suggest that the ethanol adsorption on the Pt sites is the starting step for the ethanol electrooxidation reaction. The hydrogen of ethanol at the catalyst surface is desorbed affecting to achieve the ethoxi species (Pt-OCH<sub>2</sub>CH<sub>3</sub>) or alcohol derivative (Pt-CHOHCH<sub>3</sub>). In general, the ethoxi species are more stable than alcohol derivative. Alcohol derivative was easily dehydrogenated to produce acetaldehyde. However, it can be assumed that the free of hydrogen adsorption reacts with the alcohol derivative to produce methane (CH<sub>4</sub>) and carbon monoxide (CO). On the other hand, free Pt sites can deprotonate alcohol species to form Pt<sub>2</sub>-COHCH<sub>3</sub>. The new adsorbate will be oxidized to carbon dioxide (CO<sub>2</sub>). In addition, it is observed that carbon dioxide is mainly produced from the methyl

adsorbed species that react with hydroxyl species. Nevertheless, the ethane formation may be formed the reaction between adsorbed acetaldehyde (Pt-COHCH<sub>3</sub>) and adsorbed hydrogen (Pt-H). Finally, the acetic acid formation can be predicted as a reaction of adsorbed acetaldehyde with adsorbed oxygenated species (Pt-OH) on the Pt substrate.

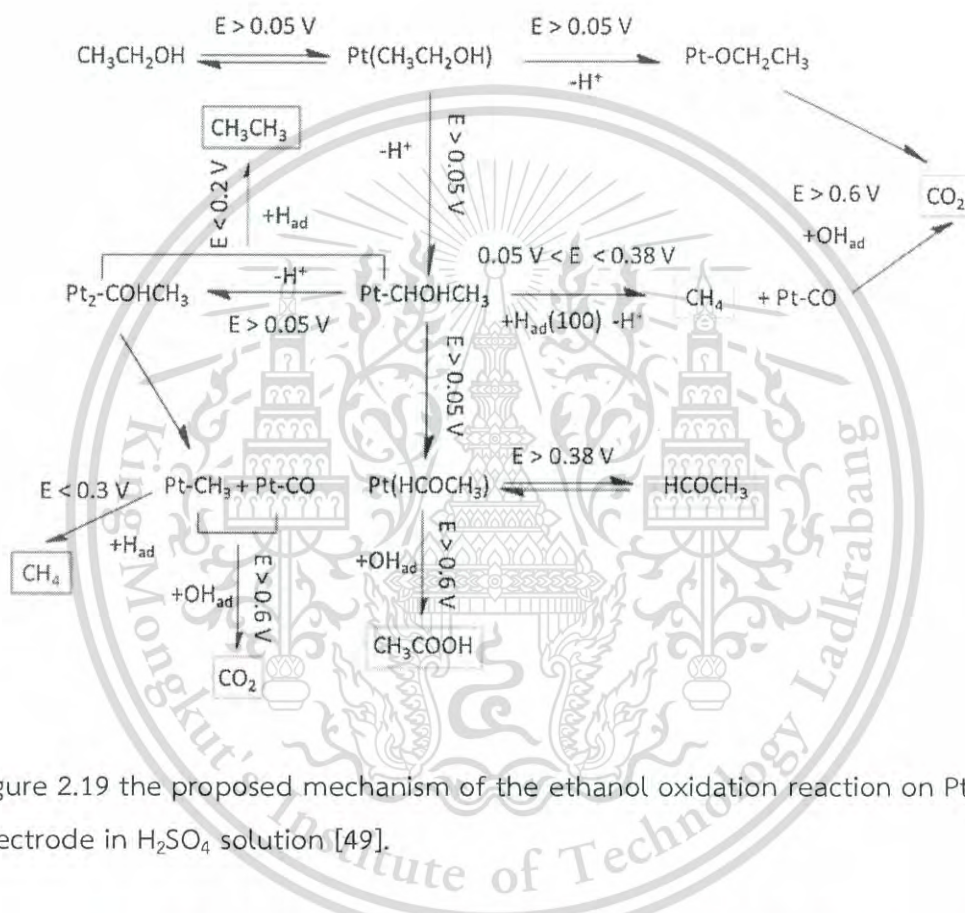


Figure 2.19 the proposed mechanism of the ethanol oxidation reaction on Pt electrode in H<sub>2</sub>SO<sub>4</sub> solution [49].

R.M. Antoniasse *et al.* [50] synthesized Pt/SnO<sub>2</sub>/C proposed as anodic electrocatalysts for direct ethanol fuel cell. The results showed that Pt/SnO<sub>2</sub>/C electrocatalysts had better electrical performance for ethanol electro-oxidation than Pt/C electrocatalysts. The main product for ethanol electro-oxidation was acetic acid whereas the small quantities of CO<sub>2</sub> were formed. The mechanism of ethanol electro-oxidation was proposed as shown in Figure 2.19. The adsorption and dehydrogenation of ethanol molecule were occurred at the Pt active sites. Acetaldehyde was generated resulting in the release of two electrons for external circuit. Some acetaldehyde

molecules can form acetyl species which may be oxidized to acetic acid with the collaboration of oxygenated species from  $\text{SnO}_2$ . In addition, the C-C bond of the acetyl species were broken that led to the generation of CO and  $\text{CH}_3$  species. Subsequently, the CO and  $\text{CH}_3$  species could be oxidized to  $\text{CO}_2$  by the collaboration of oxygenated species from  $\text{SnO}_2$ . The  $\text{SnO}_2$  could contribute to partial oxidization of ethanol to acetic acid or full oxidization of ethanol to carbon dioxide.

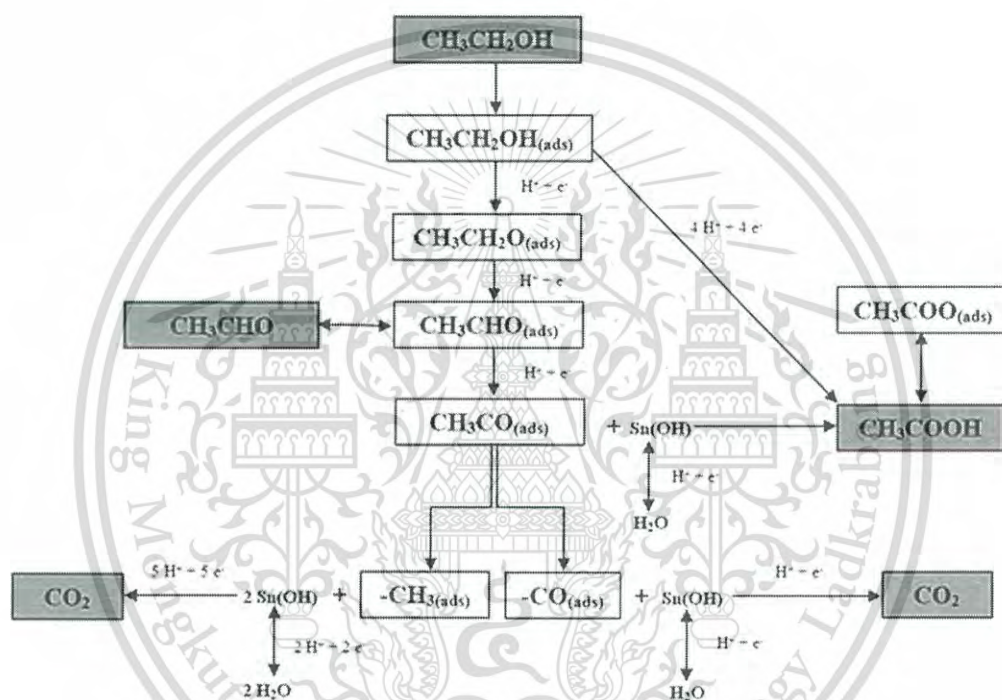


Figure 2.20 Proposed ethanol electro-oxidation mechanism over Pt/ $\text{SnO}_2$ /C, indicating the products from the bulk and adsorbed on surface catalyst [50].

J.W. Magee *et al.* [51] studied the catalytic effect of  $\text{SnO}_2$  for ethanol oxidation reaction. The prepared  $\text{SnO}_2$  solution dispersed in ethylene glycol was pipetted onto the Pt surface. Figure 2.20 (a) compares cyclic voltammogram for ethanol oxidation over the  $\text{SnO}_2$  /Pt electrode and the bare Pt electrode in ethanol 0.5 M with 0.1 M  $\text{HClO}_4$  solution at room temperature. It can be clarified that the potential of ethanol oxidation reaction with the  $\text{SnO}_2$  /Pt electrode has shifted compared to the bare Pt electrode. Moreover, Figure 2.20 (b) shows chronoamperogram that confirms the

enhancement in stability for the  $\text{SnO}_2$  /Pt electrode. It can be predicted that CO species are removed from the Pt surface by  $\text{SnO}_2$  particles affecting to the improvement in electrocatalytic C–C bond splitting of ethanol. As a result, the  $\text{SnO}_2$  support catalysts can promote the electrooxidation of ethanol to  $\text{CO}_2$  on Pt surfaces.

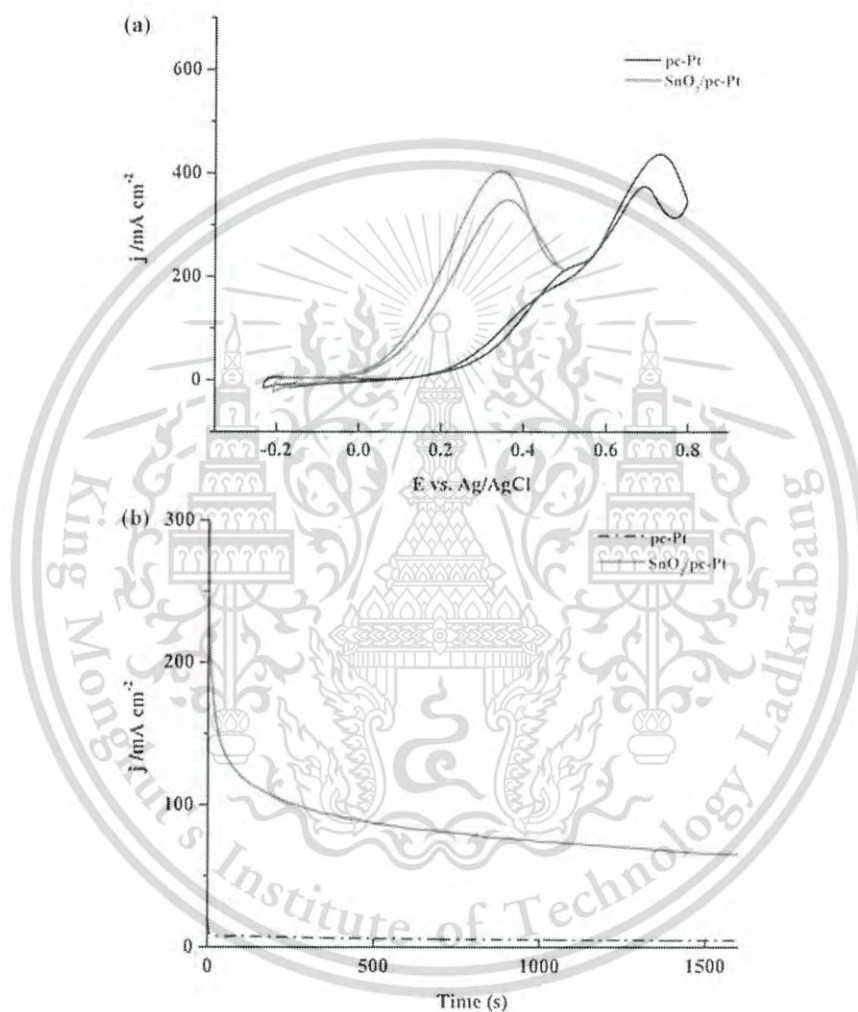


Figure 2.21 Comparison of cyclic voltammogram for a  $\text{SnO}_2$  /Pt electrode (red line) and a bare Pt electrode (black line) in ethanol 0.5 M with 0.1 M  $\text{HClO}_4$  solution. (b) Comparison of chronoamperogram for ethanol oxidation activity on a  $\text{SnO}_2$  /Pt electrode (red) and a bare Pt electrode (black) in the ethanol solution [51].

J. Selva *et al.* [52] studied the electrocatalytic activities of silver atomic quantum clusters for ethanol oxidation. The silver atomic quantum clusters supported on glassy carbon electrodes were fabricated to oxidize ethanol in electrochemical cells. The solution containing different ethanol concentrations in 1 M  $\text{H}_2\text{SO}_4$  were tested with linear sweep voltammetry for studying the catalytic activities of silver for ethanol oxidation. Figure 2.21 shows electrocatalysis of the oxidation of ethanol by silver atomic quantum clusters. It indicates that silver atomic quantum clusters requires very low potentials to promote electrocatalysis for ethanol oxidation.

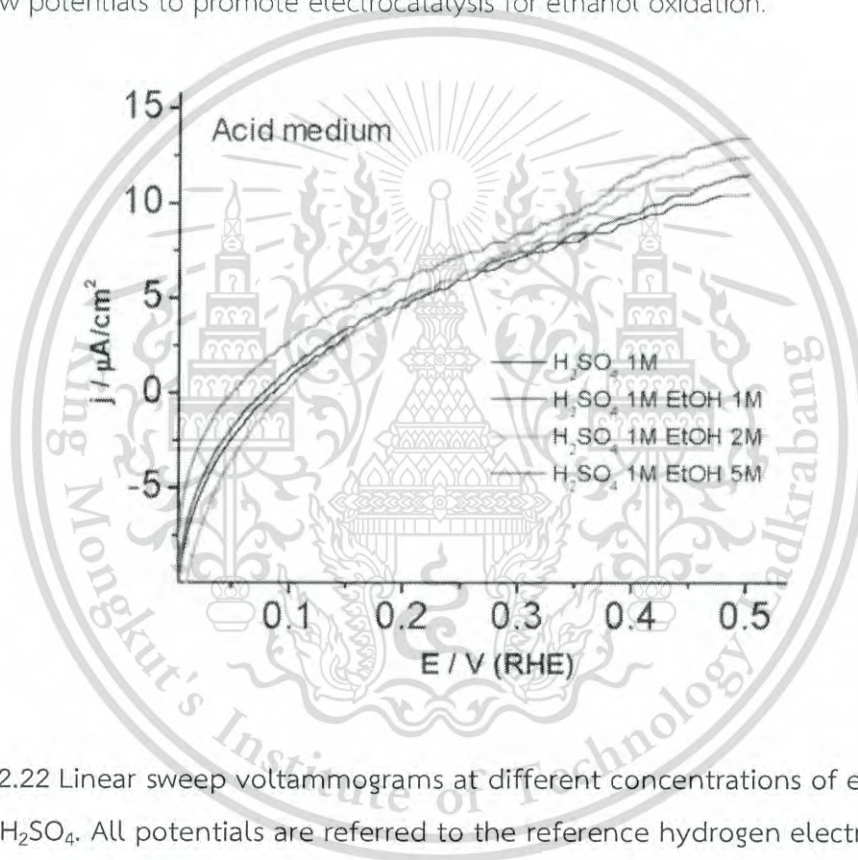


Figure 2.22 Linear sweep voltammograms at different concentrations of ethanol in 1 M  $\text{H}_2\text{SO}_4$ . All potentials are referred to the reference hydrogen electrode. Sweep rate is  $50 \text{ mV s}^{-1}$  [52].

## Chapter 3

### Research methodology

In this chapter, the combination of electrospinning technique and calcination process was the main route for synthesizing nanofibers based on tin oxide ( $\text{SnO}_2$ ). From the literature review results, polyvinylpyrrolidone (PVP) was an appropriate polymers template for synthesizing metal oxide nanofibers because of its solubility and stability.  $\text{SnCl}_4 \cdot 5\text{H}_2\text{O}$ ,  $\text{SbCl}_3$  and  $\text{NH}_4\text{F}$  were utilized as tin, antimony and fluorine source, respectively. The polymer concentration, doping concentration and calcined temperature were optimized regarding their morphologies and crystallite structure. Subsequently, the obtained  $\text{SnO}_2$ , ATO and AFTO were used as supported catalyst for ethanol oxidation reaction. The Ag/ $\text{SnO}_2$ , Ag/ATO and Ag/AFTO electrocatalysts were synthesized by hydrothermal method. The basic apparatus and simple procedure were required for synthesis and characterization. The obtained Ag/ $\text{SnO}_2$ , Ag/ATO and Ag/AFTO electrocatalysts were utilized to fabricate the working electrode for investigating the activity of the catalyst used in the ethanol oxidation reaction.

#### 3.1 Chemical reagents

1. Tin (IV) chloride pentahydrate ( $\text{SnCl}_4 \cdot 5\text{H}_2\text{O}$ ) (M.W. = 350.6)  $\geq 98\%$  Sigma-Aldrich, USA
2. Antimony Chloride ( $\text{SbCl}_3$ ) (M.W. = 228.12)  $\geq 99.95\%$  Sigma-Aldrich, USA
3. Ammonium fluoride ( $\text{NH}_4\text{F}$ ) (M.W. = 37.04) 100% Analar Normapur, Singapore
4. PolyVinylpyrrolidone (PVP) (M.W. = 1,300,000) Sigma-Aldrich, USA
5. Silver nitrate ( $\text{AgNO}_3$ ) (M.W. = 169.87)  $\geq 99.0\%$  Sigma-Aldrich, USA
6. Absolute ethanol ( $\text{C}_2\text{H}_5\text{OH}$ ) (M.W. = 46.07)  $\geq 99.98\%$  Analar Normapur, Singapore
7. *N,N*-Dimethylformamide (DMF,  $\text{C}_3\text{H}_7\text{NO}$ ) (M.W. = 73.09)  $\geq 99.8\%$  Ajax Finechem, Australia
8. Hexamethylenetetramine (HMTA) (M.W. = 140.19)  $\geq 99.0\%$  Sigma-Aldrich, USA
9. 2-propanol ( $\text{CH}_3\text{CHOHCH}_3$ ) (M.W. = 60.1)  $\geq 99.5\%$  J.T. Baker, USA

This material is reserved for educational use only, not allowed for commercial use.

Forbidden to modify the content, and cite the document when use.

Alfa Aesar, USA

10. Nafion D-521 dispersion, 5%w/w in water and 1-propanol Alfa Aesar, USA
11. Sulfuric acid ( $\text{H}_2\text{SO}_4$ ) (M.W. = 98.08)  $\geq 98\%$  RCI Labscan, Thailand

### 3.2 Equipment

1. Electrospinning apparatus (High Voltage Power Supply, syringe pump controller and collector)
2. Aluminum foil
3. Magnetic stirrer
4. Magnetic bar
5. Syringe and hypodermic needle
6. Fluorine-doped tin oxide substrate (FTO)  $\sim 10 \Omega/\text{sq}$  Sigma-Aldrich, USA
7. Oven
8. Potentiostat/Galvanostat AOVA 1.10/4.9 Metrohm, Netherlands

### 3.3 Experimental methods

#### 3.3.1 Synthesis of PVP nanofibers via electrospinning process

All experiments are illustrated in Figure 3.1. The mixture solvent was prepared by mixing *N,N*-dimethylformamide (DMF) and absolute ethanol ( $\text{C}_2\text{H}_5\text{OH}$ ) in ratio of 1:1 by volume. Subsequently, 2 grams of polyvinylpyrrolidone (PVP) was dissolved in mixture solvent to prepare 10%wt PVP solution. The PVP solution was stirred until the solution was homogeneous at the ambient temperature. The precursor solution was loaded into a 10 ml syringe with a metal needle tip for electrospinning. The Al foil was selected as a collector and the distance between the needle tip and the collector was fixed at 10 cm. The voltage was applied at 10 kV and the injection rate of the precursor solution was controlled at 0.5 ml/h by a syringe pump.

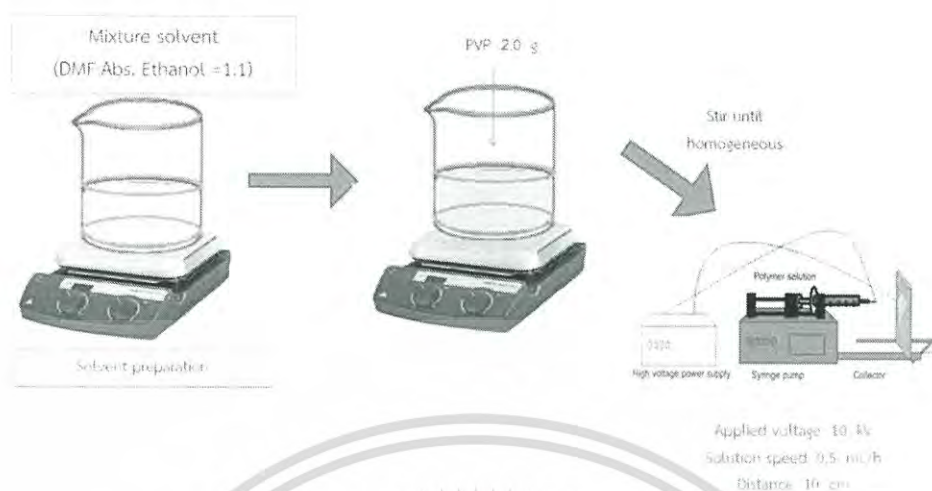


Figure 3.1 Experiment procedure of PVP nanofibers.

### 3.3.2 Synthesis of SnO<sub>2</sub> nanofibers with various calcination temperatures via electrospinning process

All experiments are illustrated in Figure 3.2. Firstly, the PVP solution 10%wt was prepared by weighing PVP 2 grams dissolved in mixture solvent between DMF and absolute ethanol (ratio = 1:1) 20 ml. Subsequently, 2 grams of SnCl<sub>4</sub>·5H<sub>2</sub>O was added to prepared polymer solution and stirred until the solution was homogeneous at the 50°C. The precursor solution was consecutively electrospun from the metal needle tip with an electrostatic voltage of 10 kV while the speed of precursor solution was designated at 0.5 ml/h and the distance between the needle and the aluminium foil collector was kept at 10 cm. The fibrous mats of electrospun precursor were collected on Al collector and calcined at 600 °C for 3 hours with a heating rate of 0.5°C/min. The calcination temperature was varied in range 450 – 600°C in order to investigate the effect of calcination temperature on their crystallite structures.

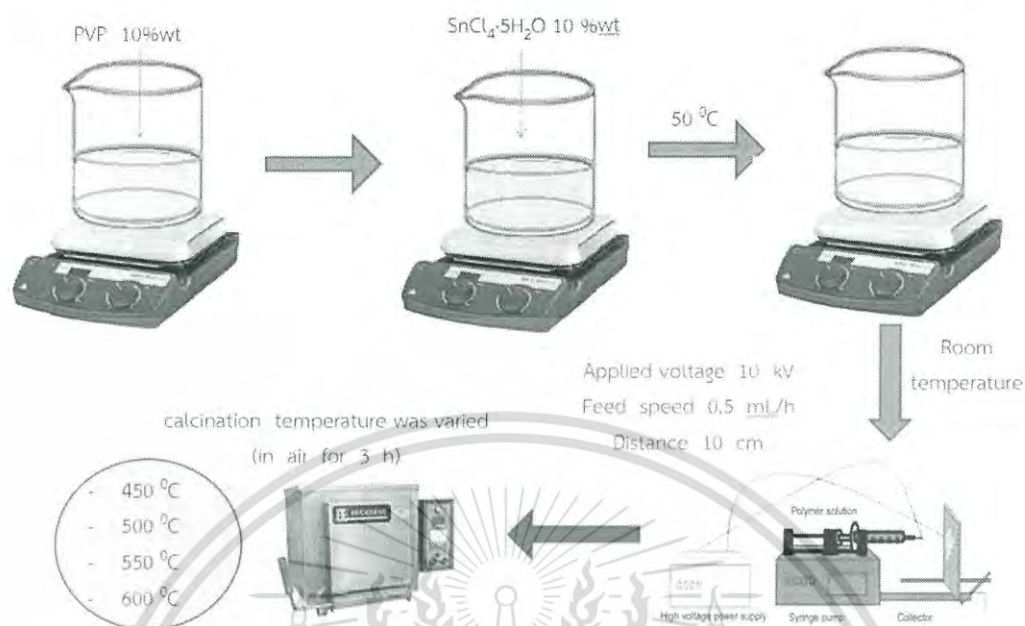


Figure 3.2 Experiment procedure of SnO<sub>2</sub> nanofibers with varied calcination temperature.

### 3.3.3 Synthesis of SnO<sub>2</sub> nanofibers with various PVP concentrations via electrospinning process

All experiment are illustrated in Figure 3.3. The concentration of PVP solution was varied in range 6 to 12 %wt to investigate the effect of PVP concentration on their morphologies. The concentration of PVP solutions were varied by weighing PVP 1.2, 1.6, 2.0 and 2.4 grams dissolved in mixture solvent between DMF and absolute ethanol (ratio = 1:1) to achieve the polymer concentration of 6, 8, 10 and 12%wt, respectively. Subsequently, 2 grams of SnCl<sub>4</sub>·5H<sub>2</sub>O was added to the prepared polymer solution then stirred until the solution was homogeneous at the 50°C. The electrospinning parameters were set up as follows; the applied voltage was kept at 10 kV, the distance between the needle tip and the Al foil collector was fixed at 10 cm and the feeding rate of the precursor solution was designated at 0.5 ml/h. The obtained as-spun SnO<sub>2</sub> fiber mats were calcined at 600°C in air for 3 hours with the heating rate of 5°C/min.

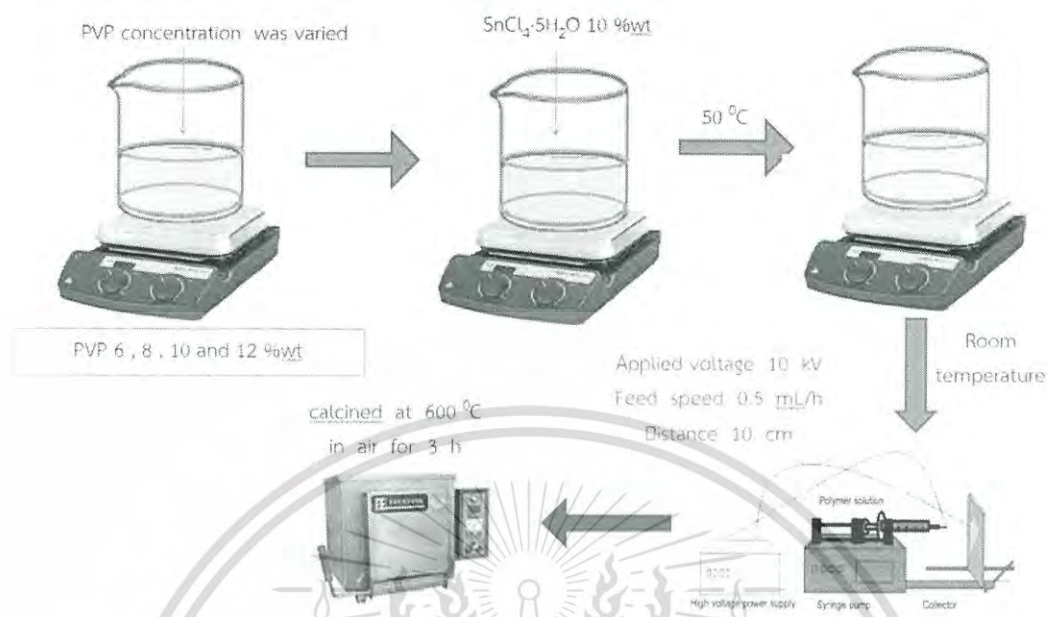


Figure 3.3 Experiment procedure of  $\text{SnO}_2$  nanofibers with varied PVP concentration.

### 3.3.4 Synthesis of Sb-doped $\text{SnO}_2$ (ATO) nanofibers with various antimony concentration via electrospinning process

All experiments are illustrated in Figure 3.4. The Sb-doped  $\text{SnO}_2$  (ATO) nanofibers were synthesized by facile and easy route via electrospinning process and calcination technique. The concentration of Sb doping was varied in range 0 to 10 %mol for investigating the effect of Sb concentration on crystallinity and morphology of  $\text{SnO}_2$  nanofibers. Firstly, 8% wt. PVP solution was prepared.  $\text{SnCl}_4 \cdot 5\text{H}_2\text{O}$  5.7 mmol (equal 2 grams) and a certain amount of  $\text{SbCl}_3$  was dissolved in the polymer solution with designated molar content of  $\text{SbCl}_3$  of 0%, 3%, 5%, 7% and 10%. Antimony concentration doping was calculated and weighed to substitute the amount of Sn precursor, 2-x grams of  $\text{SnCl}_4 \cdot 5\text{H}_2\text{O}$  and x grams of  $\text{SbCl}_3$  was added to PVP solution and stirred until the homogeneous solution was obtained. Subsequently, the precursor solution was subsequently loaded into a 10 ml syringe with a metal needle tip for electrospinning. The Al foil was selected as a collector and the distance between the needle tip and the collector was fixed at 10 cm. The voltage was applied at 10 kV and the injection rate of the precursor solution was controlled at 0.5 ml/h by a syringe

pump. The obtained fiber mats were afterward calcined at 600°C in air for 3 hours with the heating rate of 5°C/min.

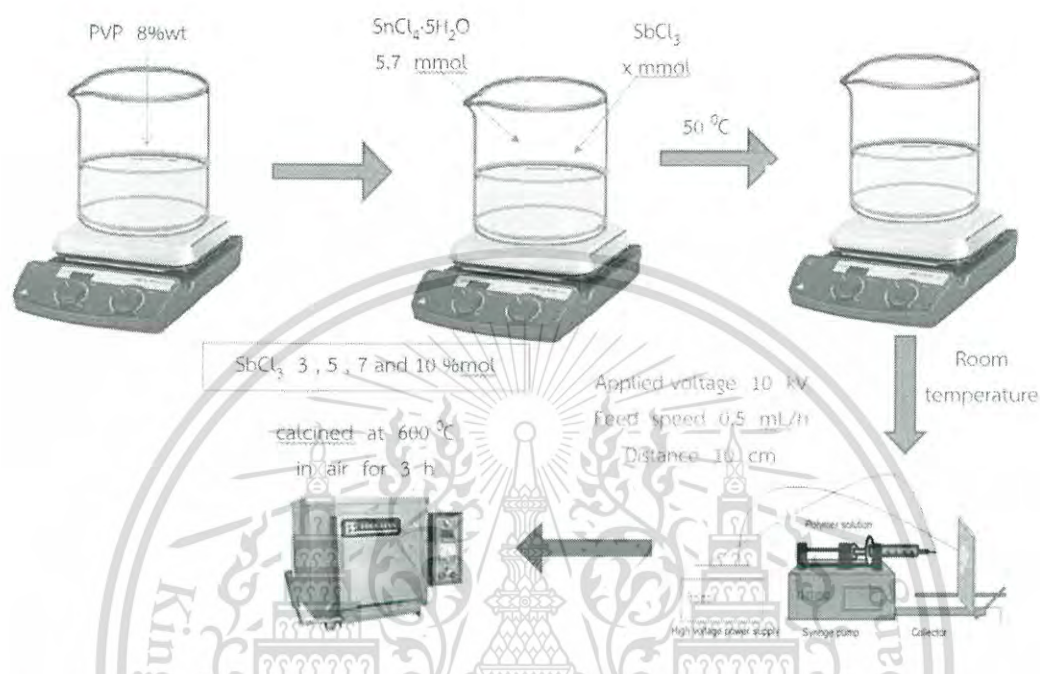


Figure 3.4 Experiment procedure of Sb doped SnO<sub>2</sub> (ATO) nanofibers with varied antimony concentration.

### 3.3.5 Synthesis of Sb/F co-doped SnO<sub>2</sub> (AFTO) nanofibers with various antimony concentrations via electrospinning process

All experiments are illustrated in Figure 3.5. The novel antimony-fluorine co-doped tin oxide (AFTO) nanofibers were synthesized by electrospinning method and calcination process. Effect of antimony concentration on crystallinity and morphology of AFTO nanofibers was investigated. Firstly, the polymer solution of 8% wt. PVP was prepared. Antimony concentration doping was calculated and weighed in range 0 – 10 %mol (x) while fluorine doping concentration was constant at 5 %mol (y). To substitute the amount of Sn precursor, 2-x-y grams of SnCl<sub>4</sub>·5H<sub>2</sub>O, x grams of SbCl<sub>3</sub> and y grams of NH<sub>4</sub>F was added to polymer solution and stirred until the homogeneous solution was obtained. The precursor solution was consecutively electrospun from the metal needle tip with an electrostatic voltage of 10 kV while the speed of precursor solution was designated at 0.5 ml/h and the distance between the needle and the

aluminium foil collector was kept at 10 cm. The fibrous mats of electrospun precursor were collected on a Al collector and calcined at 600°C for 3 h with a heating rate of 0.5°C/min.

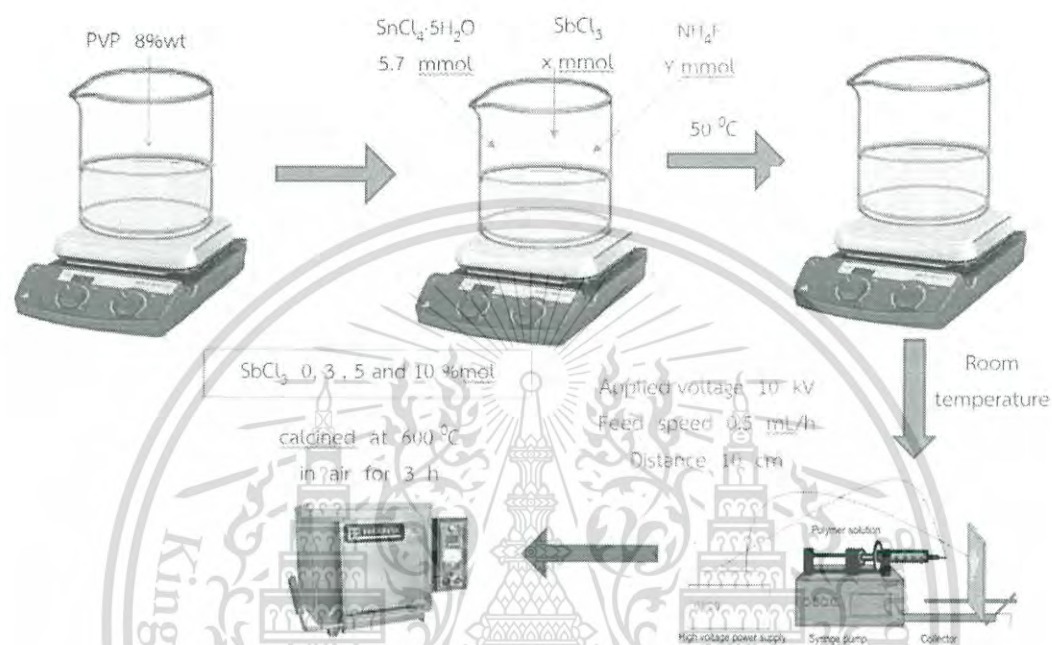


Figure 3.5 Experiment procedure of Sb/F doped SnO<sub>2</sub> (AFTO) nanofibers with varied antimony concentration.

3.3.6 Synthesis of Ag/ SnO<sub>2</sub>, Ag/ ATO and Ag/ AFTO electrocatalysts via hydrothermal method

A certain amount of pure SnO<sub>2</sub> fibers and weighed silver nitrate (10 %wt of Ag) were mixed with 0.1 M Hexamethylenetetramine (HMTA) 50 ml in an autoclave. The mixture was stirred for 3 hours before operated at 90°C for 1 hour. The obtained Ag-SnO<sub>2</sub> cluster was collected and washed with deionized water and dried at 100°C for 1 hour. The Ag/ATO and Ag/AFTO electrocatalysts were prepared as the above method.

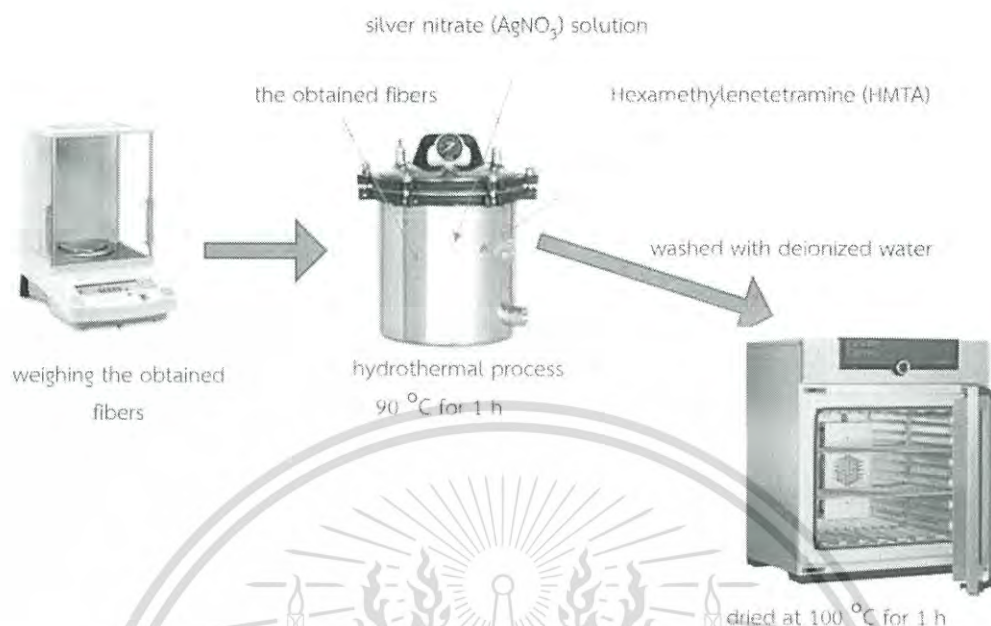


Figure 3.6 Experiment procedure of Ag/SnO<sub>2</sub>, Ag/ATO and Ag/AFTO electrocatalysts.

### 3.3.7 Characterization

3.3.7.1 Scanning Electron Microscopy (SEM) was used to observe the morphology of the Ag/SnO<sub>2</sub>, Ag/ATO catalyst and electrospun fibers by ZEISS, EVO MA10. The average diameter and diameter size distribution of fibers were measured from the diameter of 20 fibers in SEM micrographs.

3.3.7.2 Energy-dispersive X-ray Spectrophotometer (EDX) was utilized for investigating the chemical composition of Ag/SnO<sub>2</sub>, Ag/ATO catalyst and the as-synthesized, after-calcined fibers by EDX, Oxford instruments X-MaxN.

3.3.7.3 X-ray diffraction analysis (XRD) was used to characterize the crystal structure of the Ag/SnO<sub>2</sub>, Ag/ATO catalyst and the obtained fibers after calcination by Panalytical x'Pert pro MPD using Cu-K $\alpha$  radiation in the  $2\theta$  range of 20° to 80° with a scanning rate of 0.02° s<sup>-1</sup>.

3.3.7.4 The thermogravimetric analysis (TGA) was used to investigate the thermal behaviors of as-spun SnO<sub>2</sub> and pure PVP nanofibers by pyris 1 TGA, Perkin.

3.3.7.5 Fourier-transform Infrared spectroscopy (FTIR) was employed to measure the chemical bondings of as-synthesized and after-calcined as-spun fibers

with the scanning range of 400–4000  $\text{cm}^{-1}$  and the resolution of 1  $\text{cm}^{-1}$  by NICOLET 6700, Thermo scientific.

### 3.3.8 Working electrode fabrication and electrochemical measurement

Electrochemical reactivity of the catalysts was measured by cyclic voltammetry (CV) and chronoamperometry (CA) using a three-electrode cell. The Ag/AgCl and the Pt wires were used as reference and counter electrode, respectively. The electrocatalyst ink was prepared by mixing 120, 30 and 50 microliters of deionized water, isopropanol and Nafion suspension, respectively. Subsequently, 2.0 mg of the electrocatalyst was dispersed in the above solution. The resulting ink was ultrasonically stirred until the homogeneous solution was obtained. Afterward, using a micropipette to drop 5 microliters of the electrocatalyst ink on a FTO glass which was covered the edges of the electrodes by epoxy resin leaving an open area of 3 × 3 mm. Finally, the obtained working electrodes were dried in the air for overnight. The solution of 1.0 M  $\text{CH}_3\text{CH}_2\text{OH}/1.0 \text{ M H}_2\text{SO}_4$  was purged with nitrogen gas before the measurement. CV tests was conducted in the potential between -0.2 and 0.6 V versus reference electrode at a scan rate of 50 mV/s. CA tests was performed in 1.0 M  $\text{CH}_3\text{CH}_2\text{OH}/1.0 \text{ M H}_2\text{SO}_4$  for 600 s.

## Chapter 4

### Results and Discussion

#### 4.1 Result and discussion

##### 4.1.1 Comparison of morphologies between PVP fibers and as-spun SnO<sub>2</sub> fibers

Figure 4.1 shows the SEM images of PVP nanofibers and as-spun SnO<sub>2</sub> nanofibers. It is clearly observed that average diameter of PVP nanofibers is larger than the PVP + SnCl<sub>4</sub> as-spun nanofibers. The average diameter of pure polymer nanofibers and the salt-polymer nanofibers is approximately 850 and 300 nm, respectively. The first possible mechanism taking important roles on this difference is the low conductivity and high viscosity of polymer solution. Addition of SnCl<sub>4</sub> into the PVP solution is able to increase the conductivity of the solution. The net surface charge density of the solution jet consequently increases leading the significant decrease in the diameter of as-prepared fibers. The appearance of salt in polymer solution can additionally reduce the liquid jet viscosity resulting in the ease of fiber fabrication and the reduction in their size [53].

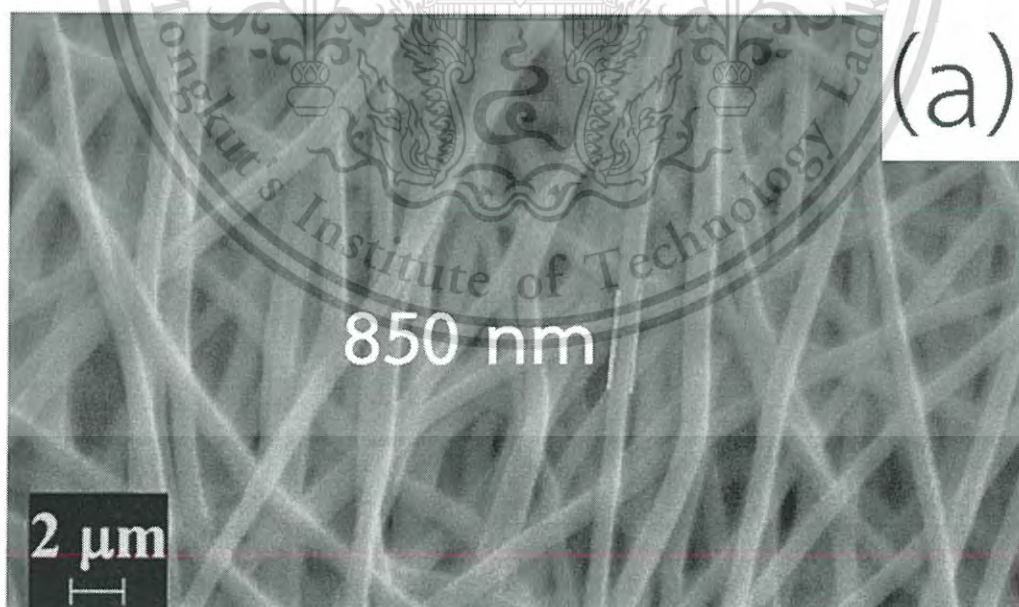


Figure 4.1 SEM images of (a) PVP nanofibers and (b) as-spun SnO<sub>2</sub> nanofibers containing PVP + SnCl<sub>4</sub>.5H<sub>2</sub>O.

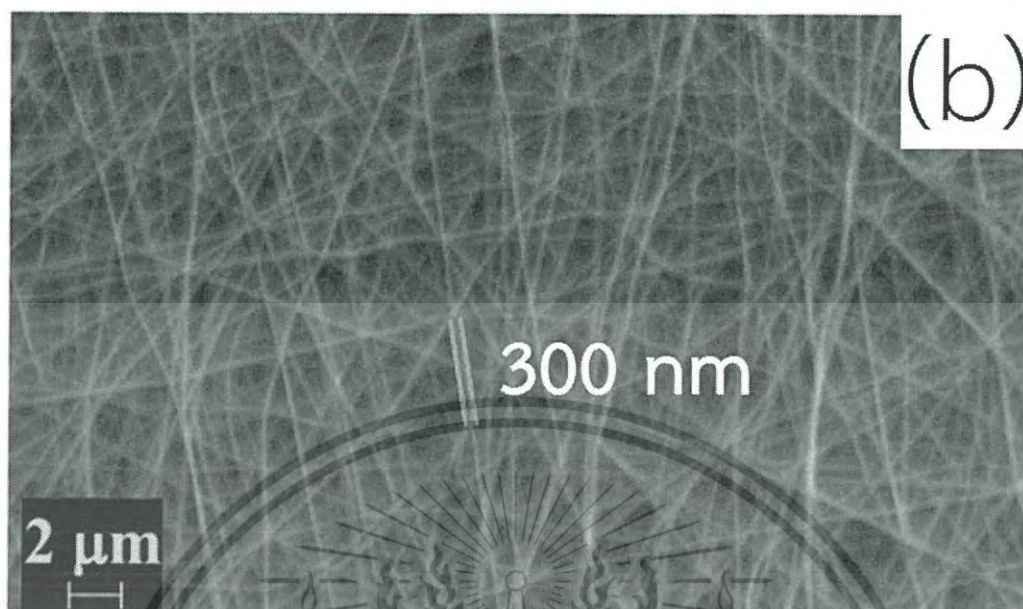


Figure 4.1 (Cont.) SEM images of (a) PVP nanofibers and (b) as-spun  $\text{SnO}_2$  nanofibers containing PVP +  $\text{SnCl}_4 \cdot 5\text{H}_2\text{O}$ .

#### 4.1.2 Optimized calcination temperature of $\text{SnO}_2$ nanofibers

Thermal behaviors of pure PVP nanofibers and as-spun  $\text{SnO}_2$  were performed using TGA and corresponding results are exhibited in Figure 4.2. The TGA curves of as-spun  $\text{SnO}_2$  nanofibers show three steps of weight loss with increasing temperature. The first weight loss of about 5% may be due to the evaporation of solvent mixture in the  $\text{SnCl}_4$ -PVP nanofibers. The 63% weight of the as-spun nanofibers was burnt out in the second step because of decomposition of PVP. The third step with 25% weight loss is originated from complete decomposition and oxidation of Sn precursor resulting the formation of  $\text{SnO}_2$  nanofibers [54].

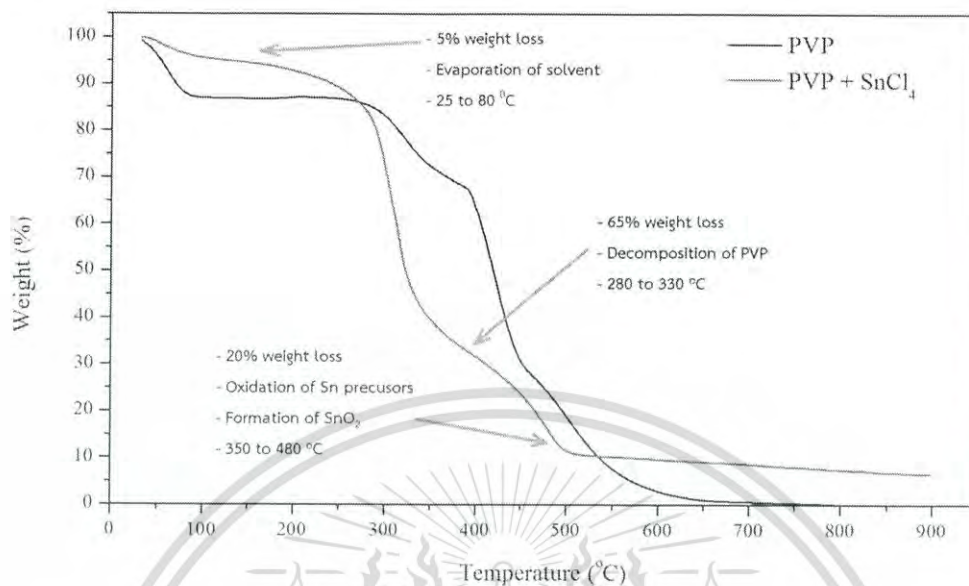
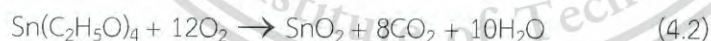


Figure 4.2 TGA graph of thermal decomposition of PVP fibers and electrospun PVP/SnO<sub>2</sub> composite.

The possible mechanism responsible for the formation of SnO<sub>2</sub> are proposed following equations (4.1) and (4.2). First, Sn precursor can react with absolute ethanol solvent to form tin alkoxide and consequently transforms to SnO<sub>2</sub>-based compounds after calcined at 600°C in air.



Tin chloride is then reacted with an excess of alcohol leading to replacement the chloride atom to formation of tin-alkoxide. Afterward, atomic rearrangement is occurred during the heat treatments in the air at 600°C leading to the crystallization of SnO<sub>2</sub>. The TGA curve of pure PVP shows that the complete disintegration of PVP occurs in the vicinity of 600°C.

The XRD patterns of the undoped SnO<sub>2</sub> nanofibers calcined at different temperatures are shown in Figure 4.3. The X-ray diffraction peak positions nicely fit with the values of rutile tetragonal SnO<sub>2</sub> phases (JCPDS 41-1445). The crystallization of

$\text{SnO}_2$  initiates at  $450^\circ\text{C}$  accompanying broad diffraction peak. At elevated temperatures the diffraction peaks of  $\text{SnO}_2$  become much sharper and more intense suggesting that the crystal growth of  $\text{SnO}_2$  is continued with an increasing calcination temperature [55].

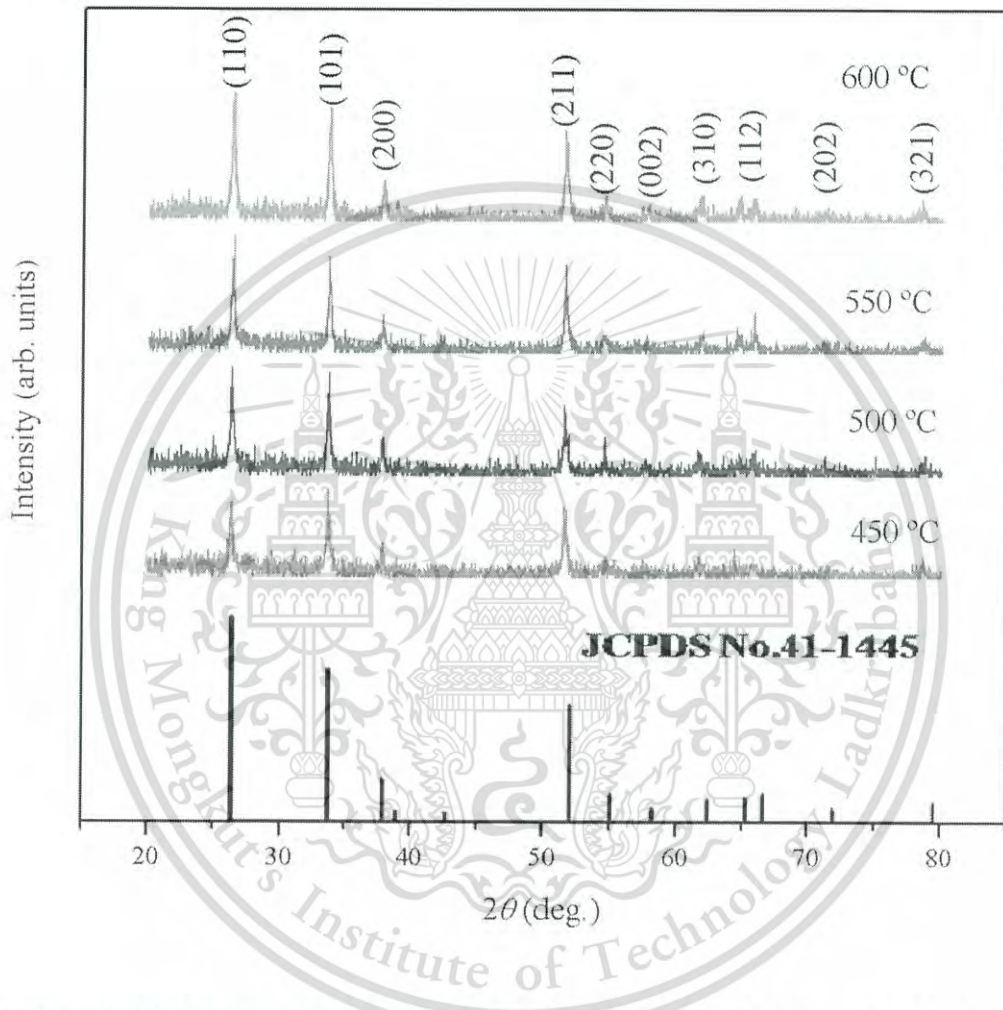


Figure 4.3 XRD patterns of the undoped  $\text{SnO}_2$  nanofibers calcined at various temperatures.

Figure 4.4 illustrates SEM images and the distribution of diameter of undoped  $\text{SnO}_2$  calcined at different temperatures. All of them show good arrangement of long continuous chain of  $\text{SnO}_2$  nanobeads. The SEM micrograph of  $\text{SnO}_2$  calcined at  $450^\circ\text{C}$  demonstrates more intensive and some part of fibers having the cumulative of  $\text{SnO}_2$  nanobeads. When the calcination temperature increases from  $500^\circ\text{C}$  to  $550^\circ\text{C}$ , the crystallite growth and rearrangement of  $\text{SnO}_2$  nanobeads and formation of fibers

This material is reserved for educational use only, not allowed for commercial use.

Forbidden to modify the content, and cite the document when use.

begins. As shown in SEM image, the long chain of porous  $\text{SnO}_2$  nanofibers structure was eventually obtained as the calcined temperature reached to  $600^\circ\text{C}$ . These results of the thermal analyses, XRD and SEM suggest that  $\text{SnO}_2$  nanofibers in form of distinguished long chain of  $\text{SnO}_2$  nanobeads can be obtained by the assistance of calcination process at certain temperature.

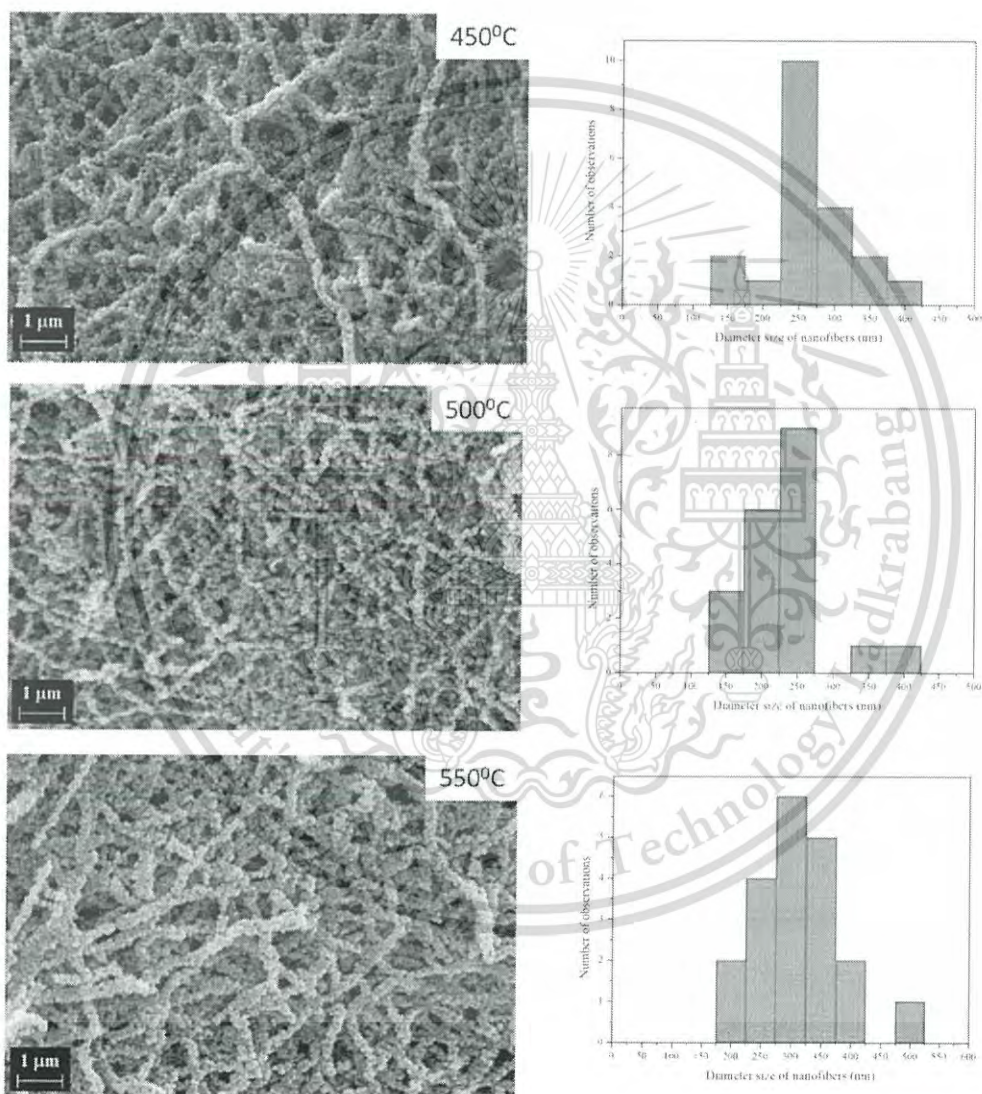


Figure 4.4 SEM images and the distribution of diameter of the undoped  $\text{SnO}_2$  nanofibers calcined at various temperatures.

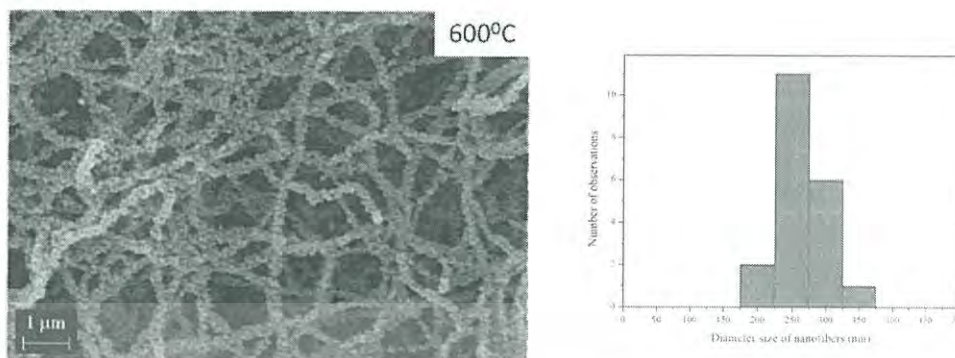


Figure 4.4 (Cont.) SEM images and the distribution of diameter of the undoped SnO<sub>2</sub> nanofibers calcined at various temperatures.

#### 4.1.3 Optimized concentration of PVP solutions of SnO<sub>2</sub> nanofibers

Figure 4.5 shows the SEM images of morphology (left) and the distribution of diameter (right) of as-spun fibers prepared from the polymer-inorganic solution with different concentrations of PVP. It can be seen that the fiber diameter noticeably increased as the concentration of PVP was elevated from 6 to 12 %wt. Moreover, the less bead fibers were observed in the sample prepared with higher concentration of PVP. Four critical concentrations of polymer solution can be explained for this result. At the lowest concentration, the solution was in low viscosity and high surface tension which was improper to form the dynamic polymer jet for electrospinning that can result in the mixture phase of beads and fibers in the mats. However, at higher polymer concentration, the helix shape of fiber would be obtained. It is suggested that the formation of nanofibers strongly depends on the polymer concentration [56]. From this work, it is advised that PVP concentration lower than 8%wt is insufficient to obtain well-defined continuous fibers with smooth surface. The average diameter of electrospun fibers as seen in SEM images 4.5(a) and 4.5(b) are approximately 80 and 127 nm, respectively. Meanwhile, the average diameter of as-spun fibers prepared from the precursor with high PVP concentration of 10%wt and 12%wt as observed SEM images 4.5(c) and 4.5(d) are about 167 and 335 nm, respectively. At this stage, it is suggested that the variation in morphology, continuity and size of as-spun fibers is directly dependent on the viscosity of the precursor due to the loading content of the polymer acting as a template for SnO<sub>2</sub> fibers.

This material is reserved for educational use only, not allowed for commercial use.

Forbidden to modify the content, and cite the document when use.

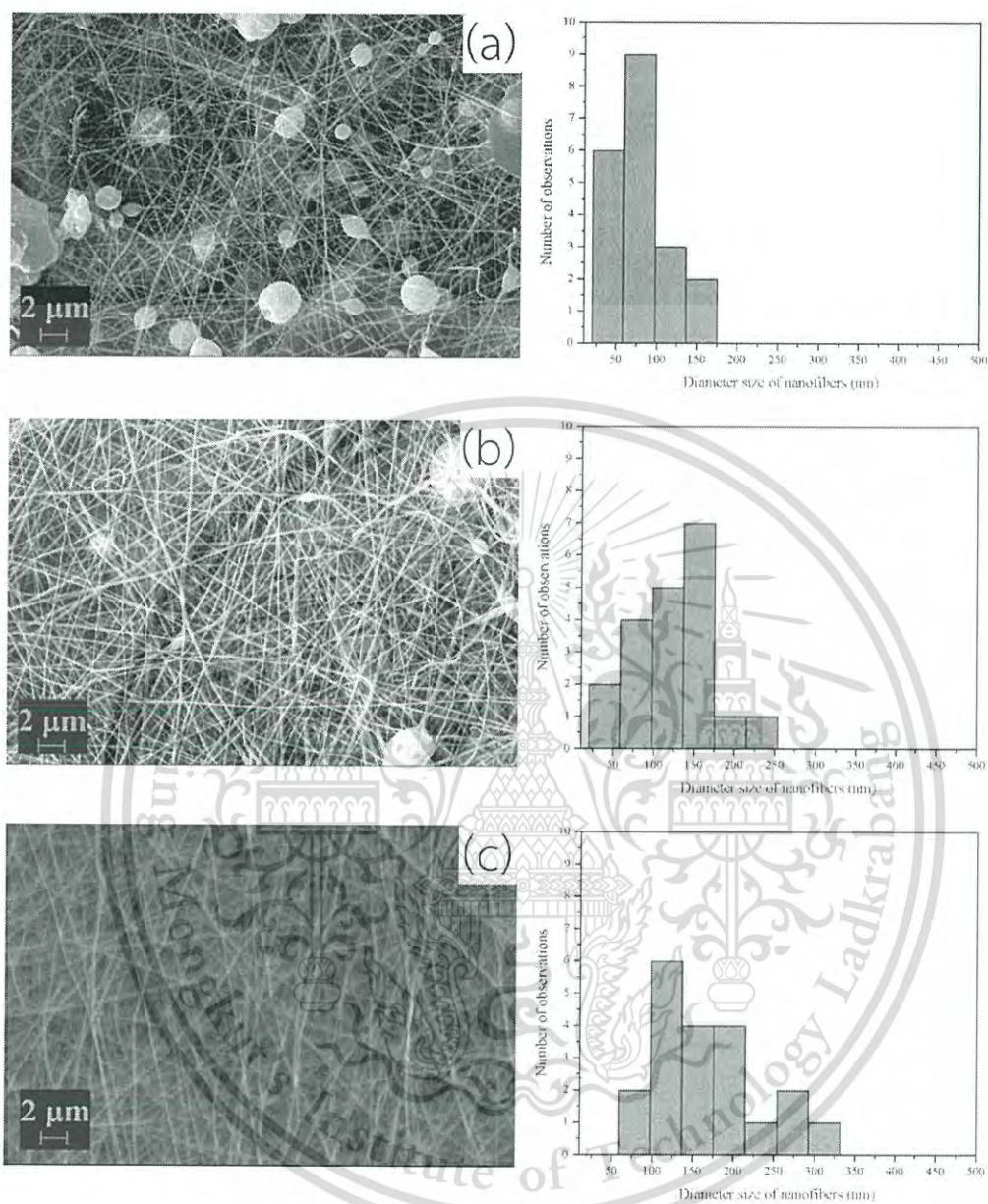


Figure 4.5 SEM images and the distribution of diameter of the as-spun SnO<sub>2</sub> fibers prepared from precursors with the different PVP concentrations; (a) 6 % (b) 8% (c) 10% and (d) 12%wt.

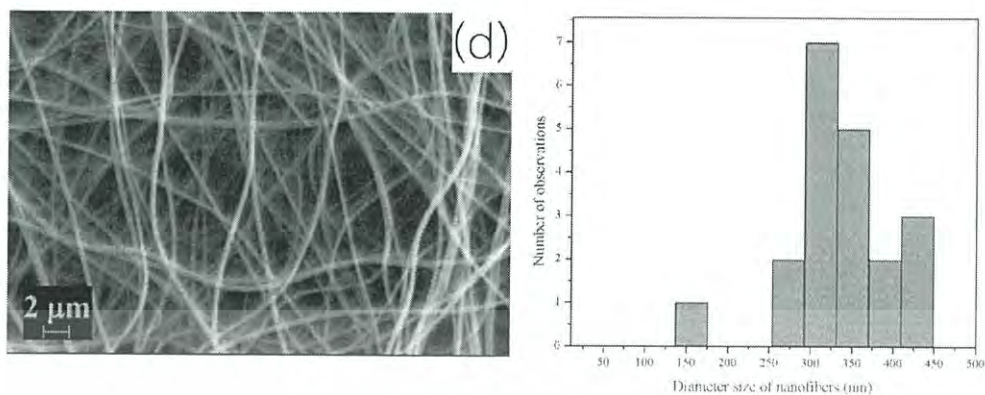


Figure 4.5 (Cont.) SEM images and the distribution of diameter of the as-spun  $\text{SnO}_2$  fibers prepared from precursors with the different PVP concentrations; (a) 6 % (b) 8% (c) 10% and (d) 12%wt.

Figure 4.6 shows the SEM images of the  $\text{SnO}_2$  nanostructures prepared from precursor with different PVP concentrations and calcined at  $600^\circ\text{C}$  for 3 hours. In typical, electrospinning process is used for fabrication of nanofibers and calcinations process was used for oxidization of Sn precursor. During electrospinning process, the rapid evaporation of absolute ethanol at the edge of the fiber and phase separation is occurred. This causes the transformation of Sn precursor to tin alkoxide and induce the precipitation of this intermediate product inside the fibers rather than the edge of the fibers leading to the form action of a solid-liquid interface in the fibers. During calcination process, the solvent trapped in the matrix is evaporated and PVP is gradually decomposed. As a result, it could provide volatile gas that may thermally diffuse to the outer surface of the fibers. The inner Sn precursor and PVP are thermally driven to the edge leading to the complete transformation of all liquid phase to solid phase and probable formation of hollow fibers. At this stage, PVP would be completely decomposed and tin alkoxide could be oxidized into  $\text{SnO}_2$  nanograins. Further calcination can result to the grain growth of  $\text{SnO}_2$  nanograins and agglomeration into big particles. However, it was reported that the decomposition of PVP played a key role in the formation of  $\text{SnO}_2$  nanofibers [57-59]. Figure 4.6(a) and 4.6(b) show corresponding SEM images of after-calcined  $\text{SnO}_2$  nanofibers prepared with 6%wt- and 6%wt-PVP precursors, respectively. These images disclose that the samples are

composed of SnO<sub>2</sub> nanograins of approximately 109 and 224 nm in diameter that well align in form of long nanofibers whose average diameters are in vicinity of 127 and 317 nm, respectively. These SEM images exhibit the tight adherence of many coordinate of uniform SnO<sub>2</sub> nanobeads to form SnO<sub>2</sub> nanofibers. The size of SnO<sub>2</sub> nanobeads tends to decrease with decreasing PVP content due to the ease of PVP decomposition at lower concentration while the growing and agglomeration of SnO<sub>2</sub> nanograins in liquid phase is incomplete. As a result, the small SnO<sub>2</sub> nanobeads was occurred and forced to move the edge of fibers. At higher PVP content, greater thermal energies is required to accomplish the decomposition of PVP. At this period, SnO<sub>2</sub> nanograins would have sufficient time to form the bigger SnO<sub>2</sub> nanobeads and lead to the rearrangement of SnO<sub>2</sub> nanobeads. When the concentration of PVP was raised to 10%wt, the strange morphology of SnO<sub>2</sub> was noticed. Its morphology abruptly changed to the continuous flat-sheet-like SnO<sub>2</sub> nanofibers. For this case, tin alkoxide may be accumulated in liquid phase rather than solid phase. When the calcination process began, PVP was decomposed and some tin alkoxide in solid phase was oxidized and transformed to the solid phase. In the same time, PVP inside fibers was sluggishly burnt out and Sn precursor was simultaneously agglomerated and oxidized to SnO<sub>2</sub> because it preferred to dissolve with absolute ethanol but PVP [60]. Thus, the flat sheets of SnO<sub>2</sub> nanofibers could be formed. As observed in Figure 4.6(d), further increase in PVP loading composition upto 12%wt results in the formation of cluster of flake-like SnO<sub>2</sub> structure. It is implied that the continuous straight of as-spun SnO<sub>2</sub> nanofibers were catastrophically destroyed after calcinations in the air. The cause of this phenomenon may originate from this mechanism. The higher PVP concentration in the solution beyond certain content may guide to the thick layer of solid phase in as-spun fibers. Thus, most of Sn precursor was aggregated inside the fiber at which it was unable to react with oxygen in the air until the PVP was burnt out [58]. This feature consequently retarded the oxidation of Sn precursors and induced the formation of flake-like structure of SnO<sub>2</sub>.

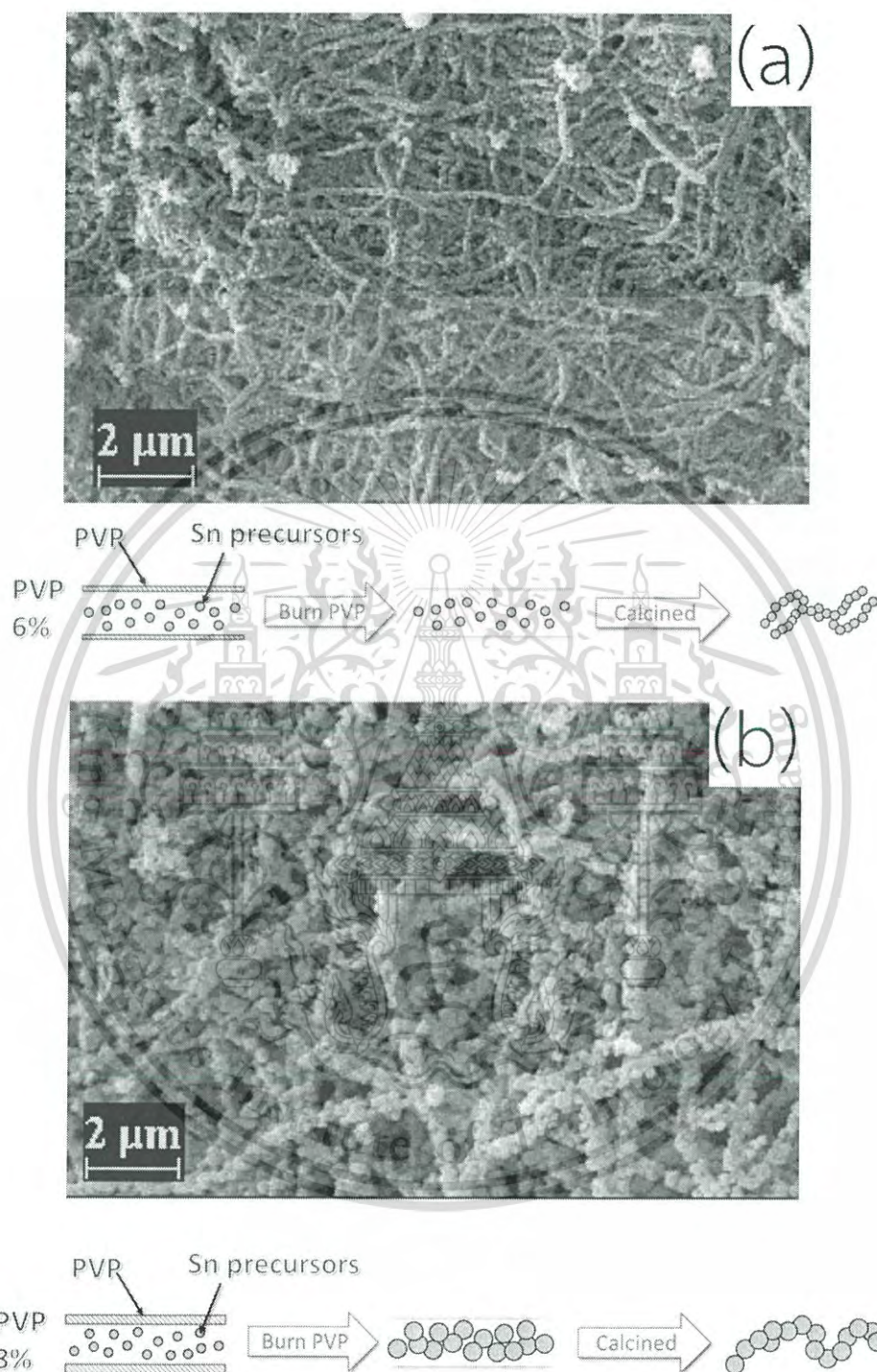


Figure 4.6 SEM images and phase diagram of formation of SnO<sub>2</sub> nanostructures prepared from precursors with the different PVP concentrations; (a) 6 % (b) 8% (c) 10% and (d) 12%wt.

This material is reserved for educational use only, not allowed for commercial use.

Forbidden to modify the content, and cite the document when use.

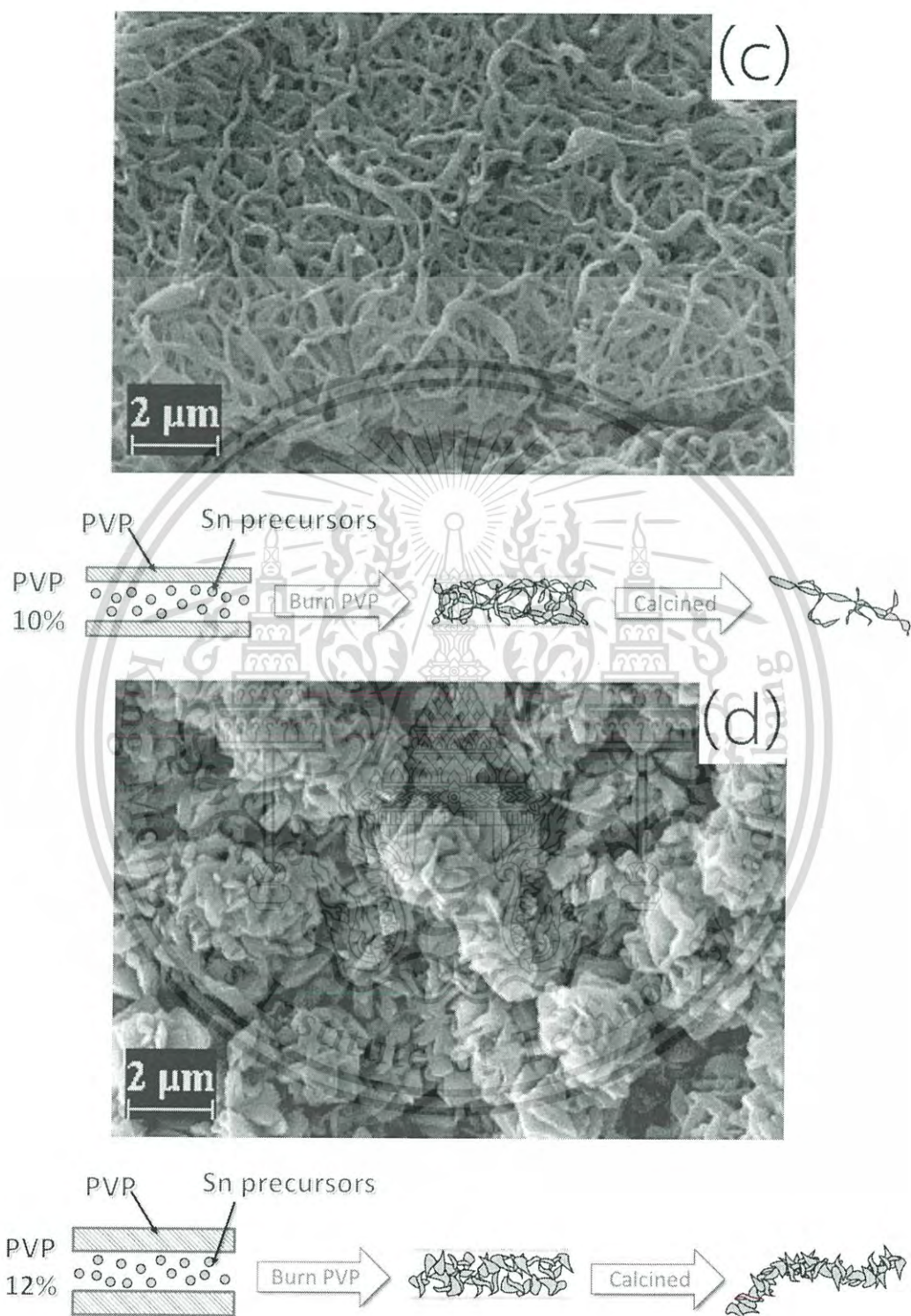


Figure 4.6 (Cont.) SEM images and phase diagram of formation of  $\text{SnO}_2$  nanostructures prepared from precursors with the different PVP concentrations; (a) 6 % (b) 8% (c) 10% and (d) 12%wt.

This material is reserved for educational use only, not allowed for commercial use.

Forbidden to modify the content, and cite the document when use.

EDX analyses of as-spun and after-calcined samples were performed to prove the composition of relevant elements of the fibers. The EDX spectrum (Figure 4.7a) of the as-spun  $\text{SnO}_2$  nanofibers possesses intense peaks of Sn, Cl, C and O displaying the composition in as-spun nanofibers. The signals of element come from the preparation solution between  $\text{SnCl}_4 \cdot 5\text{H}_2\text{O}$  and PVP. The EDX spectrum of the calcined  $\text{SnO}_2$  fiber was shown in Figure 4.7b. The peak can be assigned to Sn and O element only. The C signals may attribute to the supporting carbon tape. The EDX spectrum clearly confirms that PVP was completely decomposed and Sn precursors were oxidized to  $\text{SnO}_2$  nanostructure after calcination.

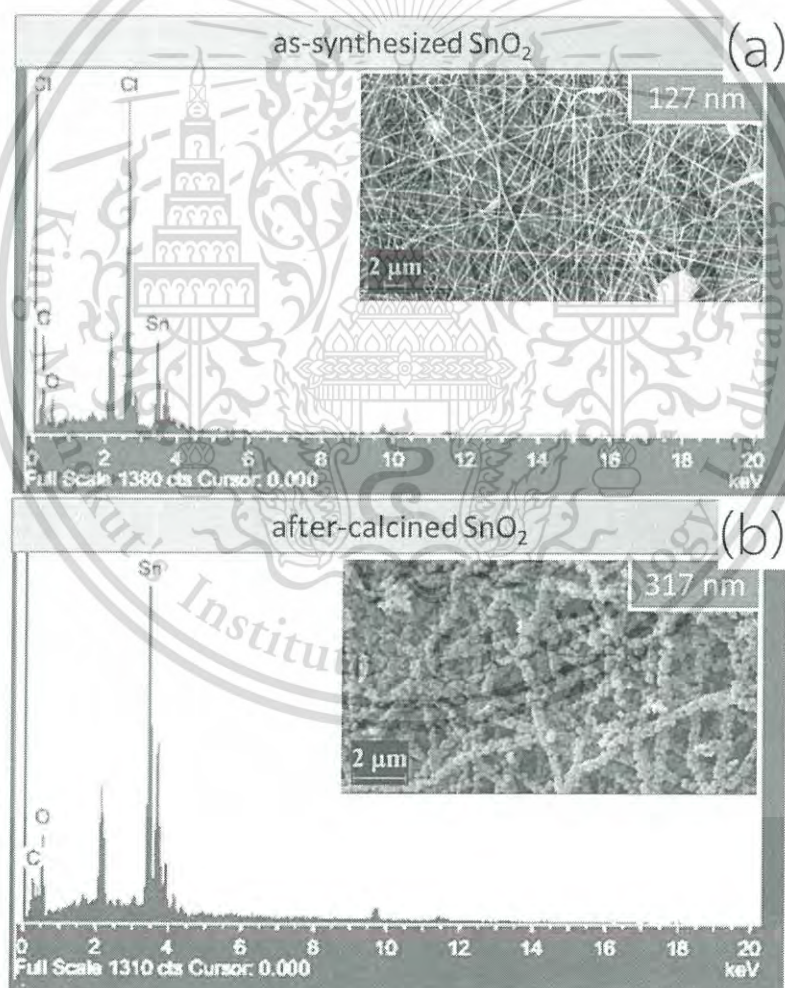


Figure 4.7 EDX spectrum and SEM images (Inset) of as-spun  $\text{SnO}_2$  nanofibers (a) before and (b) after calcination.

This material is reserved for educational use only, not allowed for commercial use.

Forbidden to modify the content, and cite the document when use.

The after-calcined products prepared from precursors with different PVP contents were characterized by XRD measurement and corresponding results are shown in Figure 4.8. The results confirm the formation and crystallinity of  $\text{SnO}_2$ . All the characteristic peaks are associated to (110), (101), (200), (211), (220), (002), (310), (112), (202) and (321) planes nicely indexed with rutile tetragonal structure of  $\text{SnO}_2$  crystal (JCPDS Card No. 41-1445) [54]. No other peaks were found in XRD patterns. This feature strongly confirms that the variation of PVP concentration in the precursor solution merely affects to the rearrangement of crystal structure and morphology of  $\text{SnO}_2$  without impurities in  $\text{SnO}_2$  crystallized phase.

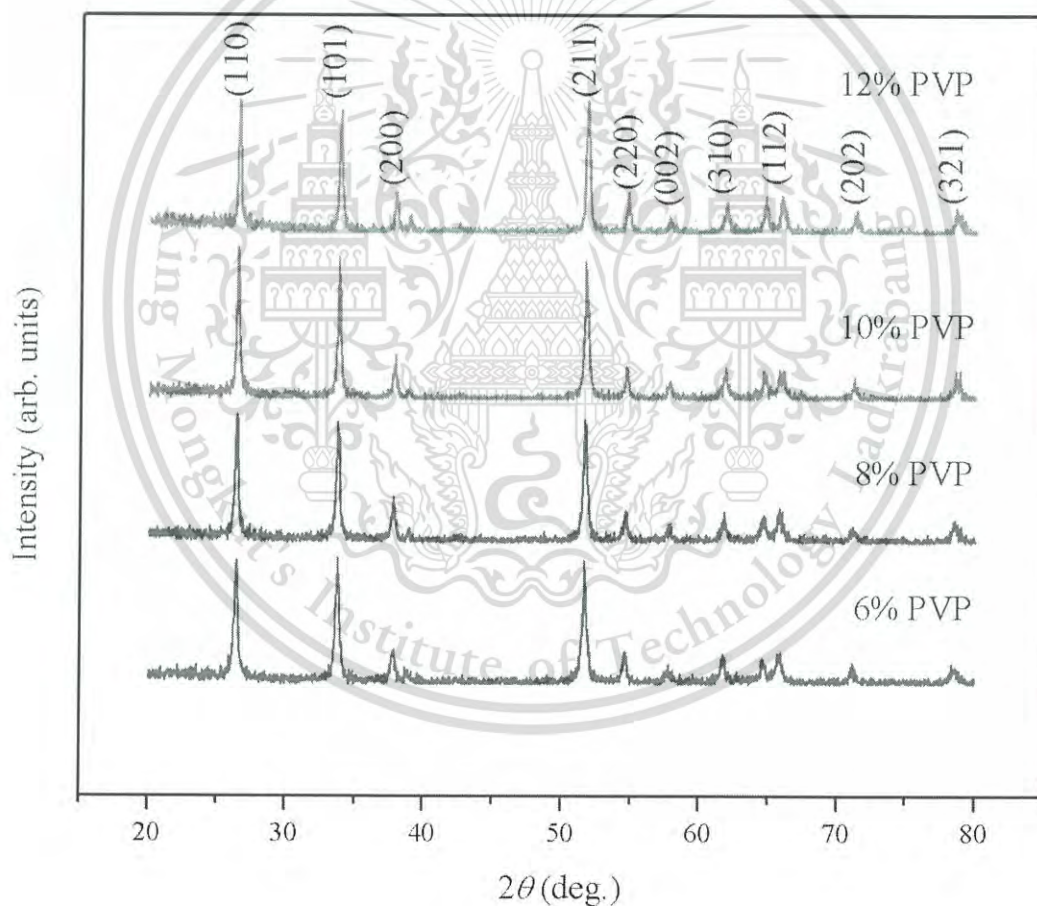


Figure 4.8 XRD pattern of after-calcined  $\text{SnO}_2$  nanostructures prepared from precursors with the different PVP concentrations.

#### 4.1.4 Synthesized Sb-doped SnO<sub>2</sub> (ATO) fibers

The difference of morphology and composition of the as-spun ATO nanofibers before and after calcination is illustrated in Figure 4.9. Figure 4.9a and 4.9b show corresponding spectra of EDX analysis of ATO nanofibers before and after calcination, respectively. The EDX spectrum shows that the as-spun nanofibers after calcination is composed of Sn, O and Sb implying the existence of major elements and formation of ATO nanofibers. The image of as-spun nanofibers in Figure 4.9a (Inset) shows the smooth surface with the average diameter about 200 nm. Consequently, after annealing at 600°C in air, SEM image in Figure 4.9b (Inset) shows an ATO nanocrystalline fibrous network morphology whose average diameter about 447 nm with rough surface. The after-calcined fibers comprise many small beads of tightly bound ATO nanoparticles arranging in form of well-defined and nanofibers with good uniformity in their size. [52]

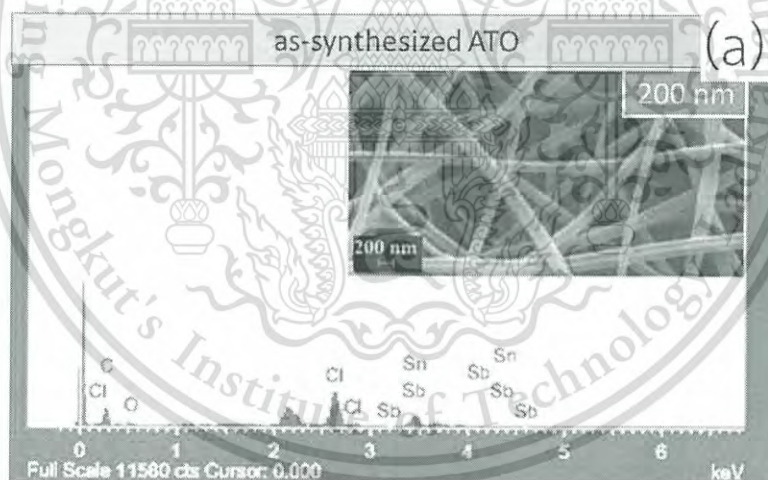


Figure 4.9 EDX spectrum and SEM images (Inset) of ATO nanofibers (a) before and (b) after calcination.

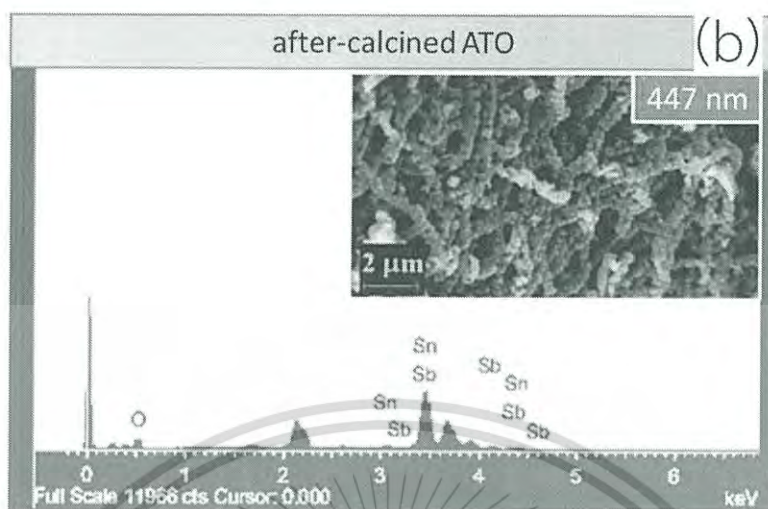


Figure 4.9 (Cont.) EDX spectrum and SEM images (Inset) of ATO nanofibers (a) before and (b) after calcination.

Figure 4.10 shows SEM images of ATO nanofibers with different Sb concentrations. It can be found that ATO nanofibers display high fibrous morphology with increasing Sb-doping concentration suggesting that Sb concentration plays a key role on the modification of  $\text{SnO}_2$  fiber formation. The relevant mechanism for the formation of ATO nanofiber with incorporation of Sb dopant can be addressed. During calcination process of as-spun ATO nanomats, the decomposition of PVP was occurred and provided volatile gas that could thermally diffuse to the surface of the fibers. Subsequently, the  $\text{SnO}_2$  nanoparticles would be nucleated, crystallized and aggregated at the surface of fibers [59]. In addition, doping of Sb could considerably interrupt the  $\text{SnO}_2$  crystalline growth [61] guiding to the deterioration in their particle size in the fibers. Furthermore, In case of 5% and 7% ATO as observed in Figure 4.10 (b) and 4.10 (c), high Sb content can prevent crystallization and agglomeration of  $\text{SnO}_2$  nanoparticles and part of Sn precursor may be separated and diffused to surface of fiber. The Sn precursor at surface templates was crystallized, but some of  $\text{SnO}_2$  could migrate to the core of fibers. When the Sb concentration increased to 10%, the dopant atom could cause the further reduction in particle size of  $\text{SnO}_2$  and initiate the firm adherence between tiny particles to form more fibrous morphologies as noticed in

Figure 4.10 (d). From this result, it is suggested that 7% ATO sample is optimized condition that simultaneously provide fibrous and porous morphology.

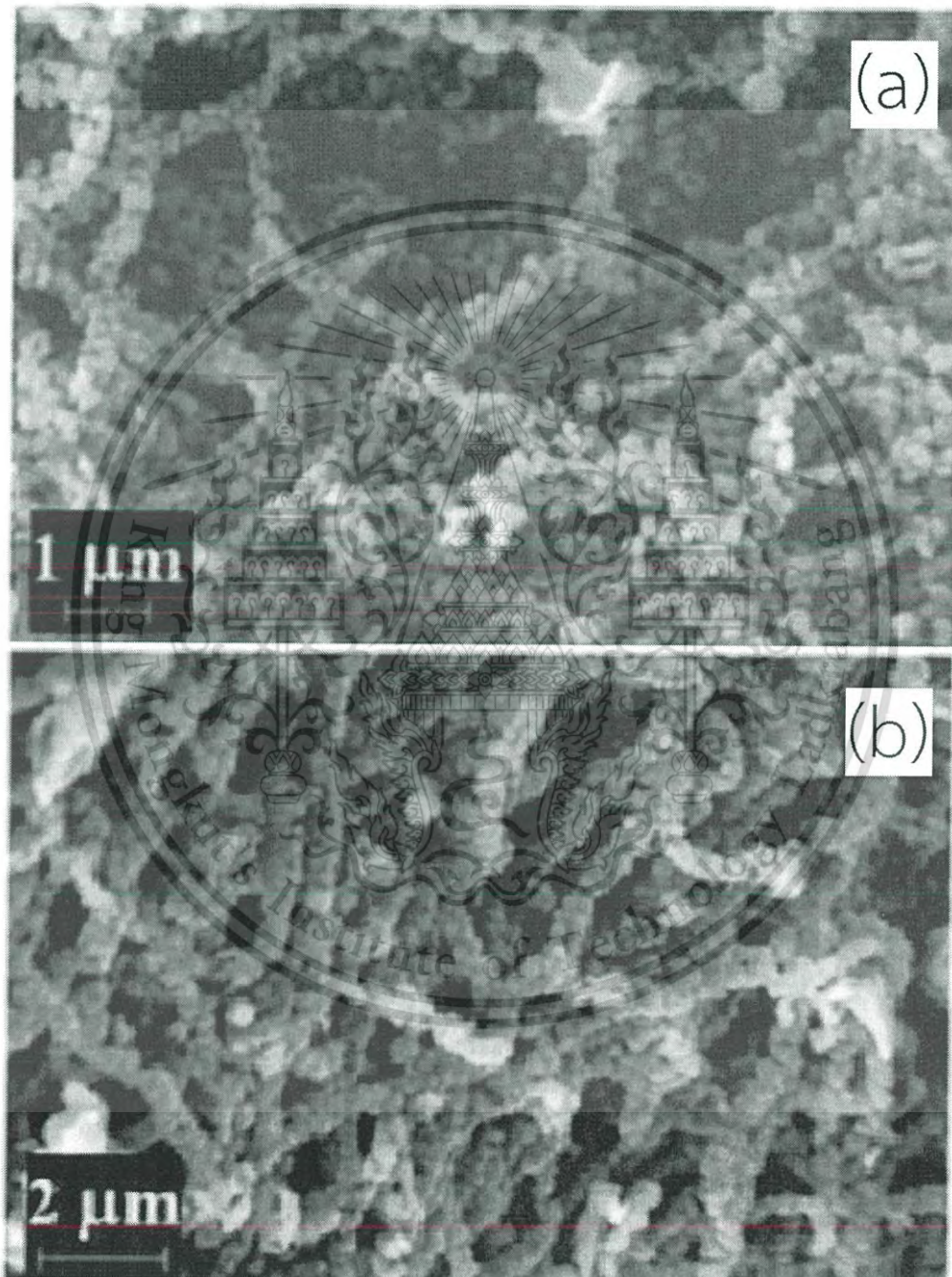


Figure 4.10 SEM image of SnO<sub>2</sub> nanofibers containing various Sb concentration (a) 3% (b) 5% (c) 7% and (d) 10%mol.

This material is reserved for educational use only, not allowed for commercial use.

Forbidden to modify the content, and cite the document when use.

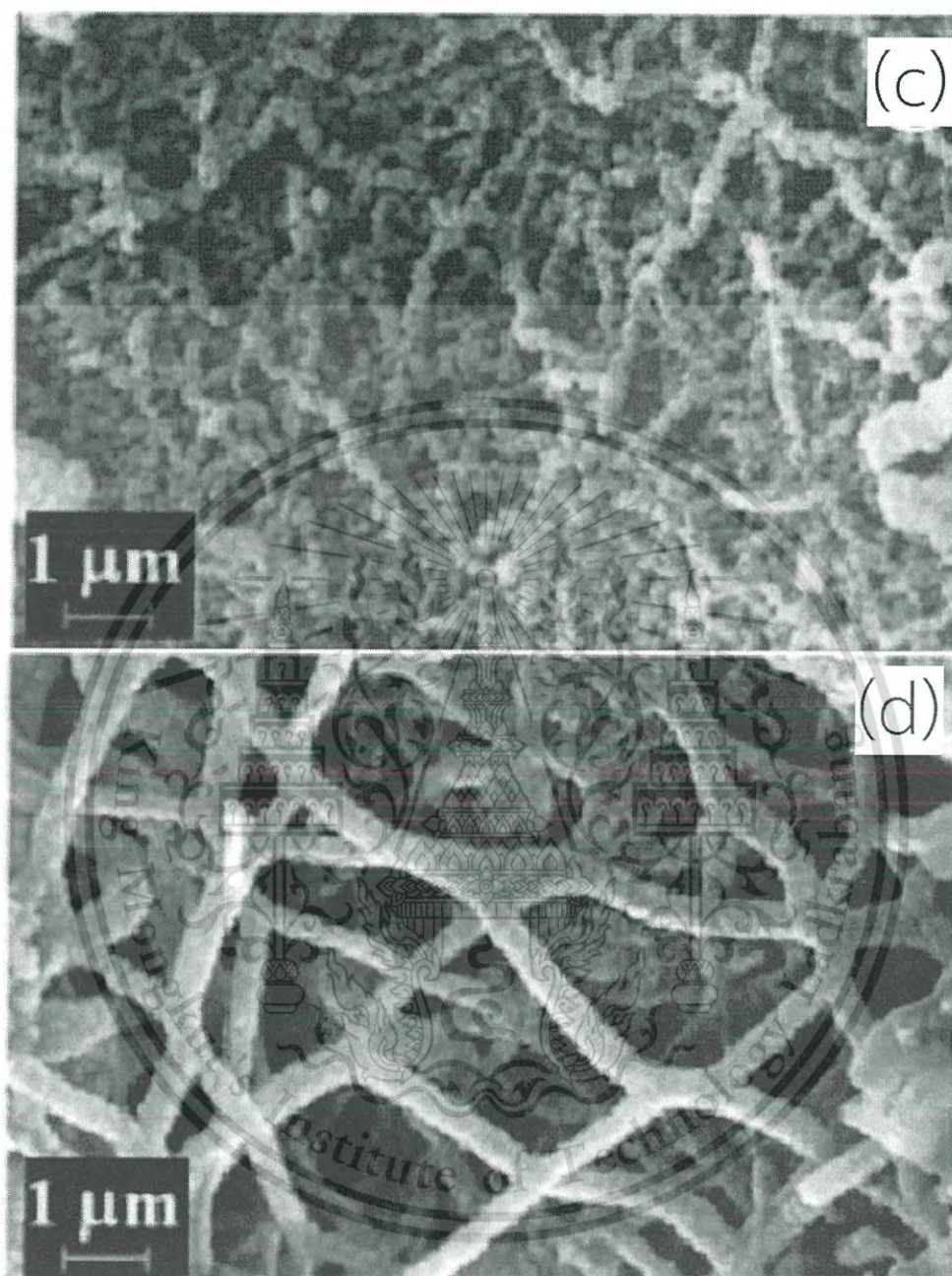


Figure 4.10 (Cont.) SEM image of  $\text{SnO}_2$  nanofibers containing varied Sb concentration (a) 3% (b) 5% (c) 7% and (d) 10% mol.

The XRD spectra of the pure  $\text{SnO}_2$  and ATO nanofibers are exhibited in Figure 4.11. After calcination at  $600^\circ\text{C}$  for 3 hours, all samples possess sharp and intense diffraction peaks that are well indexed to the tetragonal structure of  $\text{SnO}_2$  in JCPDS

This material is reserved for educational use only, not allowed for commercial use.

Forbidden to modify the content, and cite the document when use.

No. 41-1445. It can be further noticed that no strange peaks of impurity or separated phase due to the incorporation of Sb dopant is observed. This feature implies successful doping of Sb into  $\text{SnO}_2$  crystalline lattice.

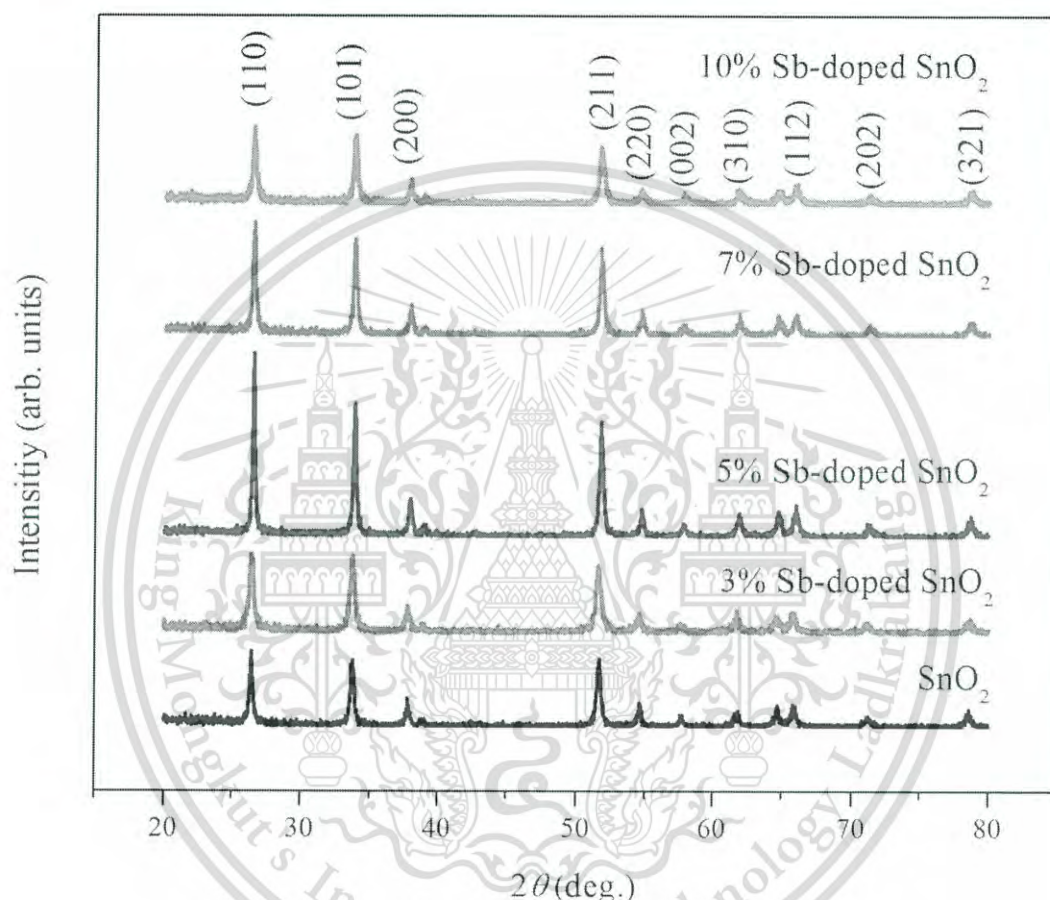


Figure 4.11 XRD patterns of  $\text{SnO}_2$  and Sb doped  $\text{SnO}_2$  (ATO) nanofibers with different Sb concentrations.

#### 4.1.5 Synthesized Sb/F doped $\text{SnO}_2$ (AFTO) fibers

The XRD patterns of AFTO nanofibers with different Sb concentrations are shown in Figure 4.12. It is observed that no impurity diffraction peak is detected in AFTO samples. It can be guided that the primary of co-doping Sb/F into  $\text{SnO}_2$  is accomplished by electrospinning technique and calcination process. The intensities of AFTO diffraction peaks reduce when compared with the FTO diffraction peaks (0% Sb).

5%F doped  $\text{SnO}_2$ ). Meanwhile, the intensities of diffraction peaks of AFTO exhibit significant increase with increasing Sb concentration. It is noticed that the crystallite sizes of AFTO are 24.13, 18.51, 19.82, and 22.61 nm for the samples with 0, 3, 5 and 10% mol of Sb doping content, respectively.  $\text{Sb}^{3+}$  ion can prevent the crystallization of  $\text{SnO}_2$  because the larger ionic radius of doping ion. As a result, part of  $\text{Sn}^{4+}$  precursors are collected at the surface of the fibers more than condensed at the center. After calcination in the air, the crystallization of AFTO nanoparticles was obtained and presented in porous fiber form.

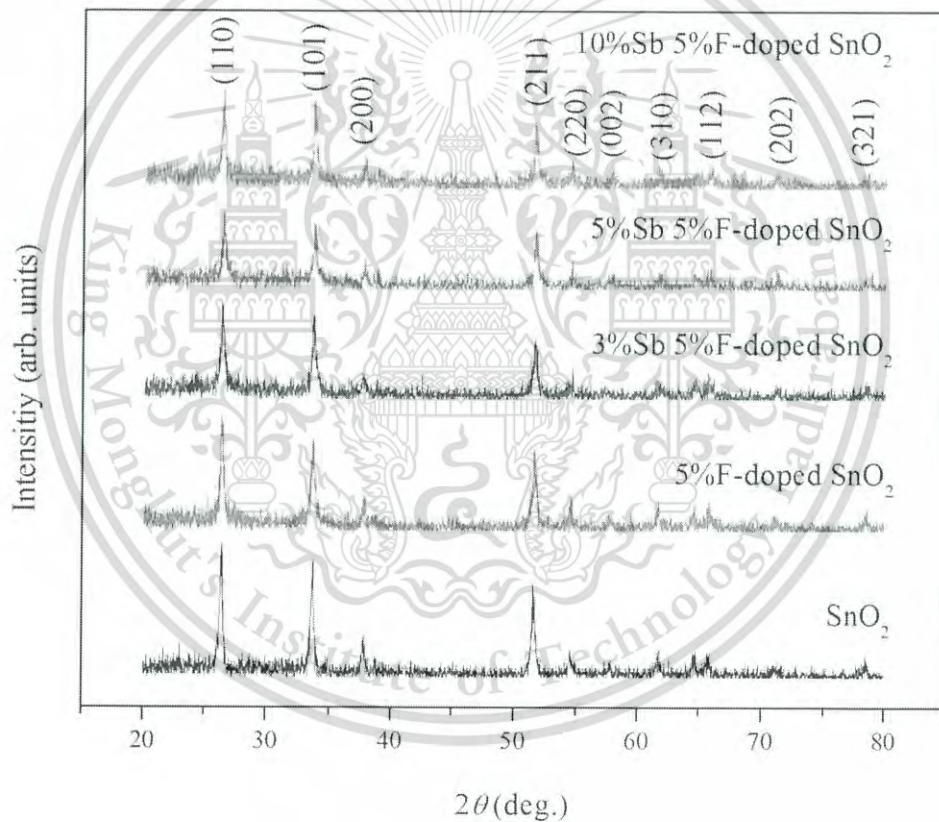


Figure 4.12 XRD patterns of the AFTO nanofibers with varied Sb concentration calcined at  $600^\circ\text{C}$ .

SEM images in Figure 4.13 reveal the morphologies of AFTO samples with different Sb doping concentrations. SEM image of FTO nanofibers (0%Sb) indicates ill-defined fibrous structures with poor uniformity in shape and size due to  $\text{NH}_3$  from F-precursor that may cause the modification of precursor during electrospinning process. The morphology of 3%Sb in AFTO shows more vigorous and well-defined fibrous structure than FTO nanofibers. It consists of clusters of small nanoparticles adhering to the fibers. SEM image of 5%Sb AFTO exhibits porous fibers with the crowd of AFTO nanobeads while SEM image of 10%Sb AFTO displays only the porous AFTO fibers. Moreover, it is observed that the diameter of AFTO nanofiber increases as well as the AFTO crystallite size.



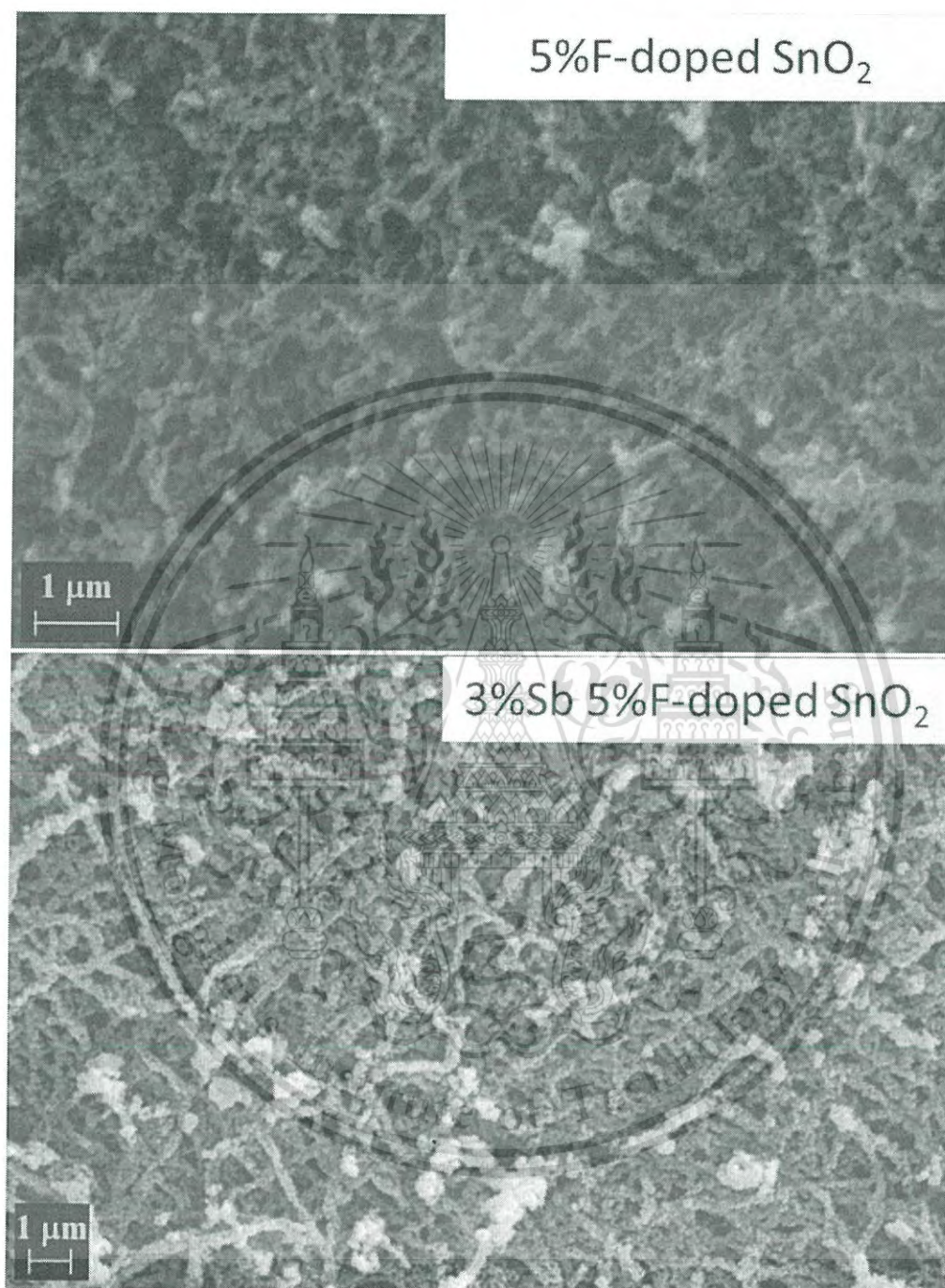


Figure 4.13 SEM images of the Sb/F co-doped SnO<sub>2</sub> (AFTO) nanofibers with varied Sb concentration calcined at 600°C.

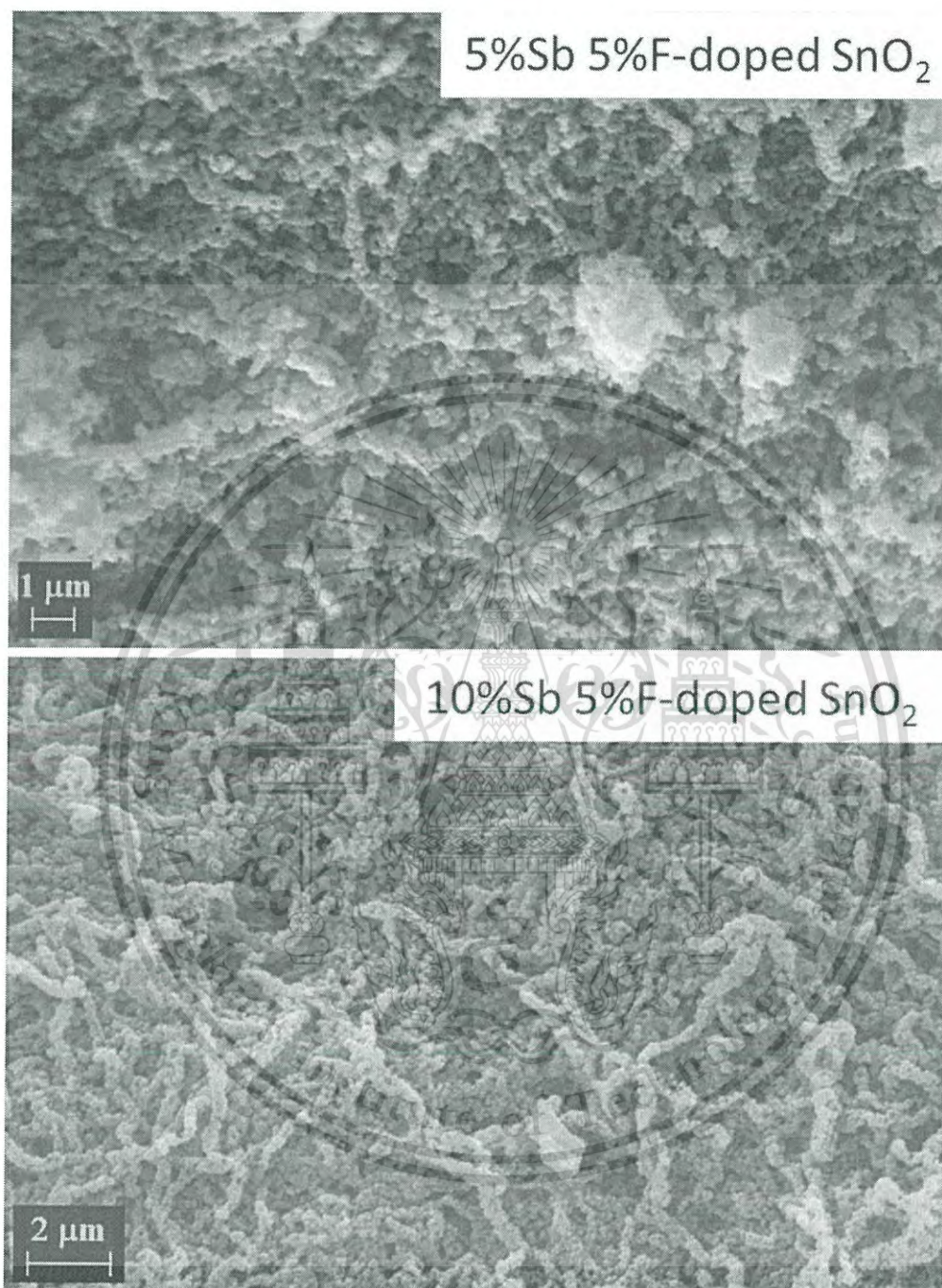


Figure 4.13 (Cont.) SEM images of the Sb/F co-doped SnO<sub>2</sub> (AFTO) nanofibers with varied Sb concentration calcined at 600°C.

The existence of relevant elements in the as-synthesized (a) and after calcined (b) AFTO nanofibers were confirmed by EDX spectrum as exhibited in Figure 4.14. The absence of Cl signal in after-calcined sample compared with as-synthesized sample was noticed, implying the successful doping and formation of AFTO nanofibers. SEM images of the as-synthesized and after-calcined AFTO nanofibers are shown as insets in Figure 4.14. The as-synthesized fibers have smooth surface while after calcined sample appears in rough surface. The average diameter of the as-synthesized AFTO nanofibers 209 nm while the average diameter of the obtained fibers after calcined at 600 °C are 422 nm.



Figure 4.14 EDX spectrum and SEM images (Inset) of AFTO nanofibers (a) before and (b) after calcination.

This material is reserved for educational use only, not allowed for commercial use.

Forbidden to modify the content, and cite the document when use.

#### 4.1.6 Comparison of material based on SnO<sub>2</sub> nanofibers

The XRD patterns of undoped SnO<sub>2</sub>, Sb-doped SnO<sub>2</sub>, F-doped SnO<sub>2</sub> and Sb/F doped SnO<sub>2</sub> nanofibers are illustrated in Figure 4.15. All samples possess the single polycrystalline of tetragonal structure with major crystal lattice planes of (110), (101) and (211) [62] without noticeable impurities. It could be advised that Sb ion and F ion would be suitably incorporated into the SnO<sub>2</sub> lattice in ATO, FTO and AFTO products. The substitution of Sb<sup>3+</sup> and F<sup>-</sup> ions at Sn<sup>4+</sup> and O<sup>2-</sup> sites in the SnO<sub>2</sub> lattice, respectively could enable the generation of extra electrons to the conduction band, resulting in the increase of conductivity of SnO<sub>2</sub>. [63, 64] The crystallite sizes of the products determined by full width at half maximum (FWHM) of a major diffraction peak (110) using a well-known Scherrer's equation. It is found that the values of the undoped SnO<sub>2</sub>, ATO, FTO and AFTO nanofibers are 24.22, 28.64, 24.13 and 19.82 nm, respectively. It is noticed that the crystallite size of the ATO is bigger than the undoped SnO<sub>2</sub>. This feature could be originated from the fact that the ionic radius of Sb<sup>3+</sup> ( $r = 0.76 \text{ \AA}$ ) is larger than Sn<sup>4+</sup> ( $r = 0.69 \text{ \AA}$ ) that would obstruct the crystallization of SnO<sub>2</sub>. As a result, some of Sn<sup>4+</sup> could diffuse and agglomerate to form fiber wall and generate the larger crystallite size of SnO<sub>2</sub>. On the other hand, the ionic radius of fluorine ion ( $1.33 \text{ \AA}$ ) was very close to oxygen ion ( $1.32 \text{ \AA}$ ). The substitution of O<sup>2-</sup> with F<sup>-</sup> is therefore insignificant make the variation of crystallite size of SnO<sub>2</sub>. The possible reason for the significant reduction in crystallite size of AFTO may originate from the synergistic of Sb<sup>3+</sup>-F<sup>-</sup> co-doped into SnO<sub>2</sub> lattice guiding to intercept the coagulation of Sn precursor and accelerate the formation of SnO<sub>2</sub> particles.

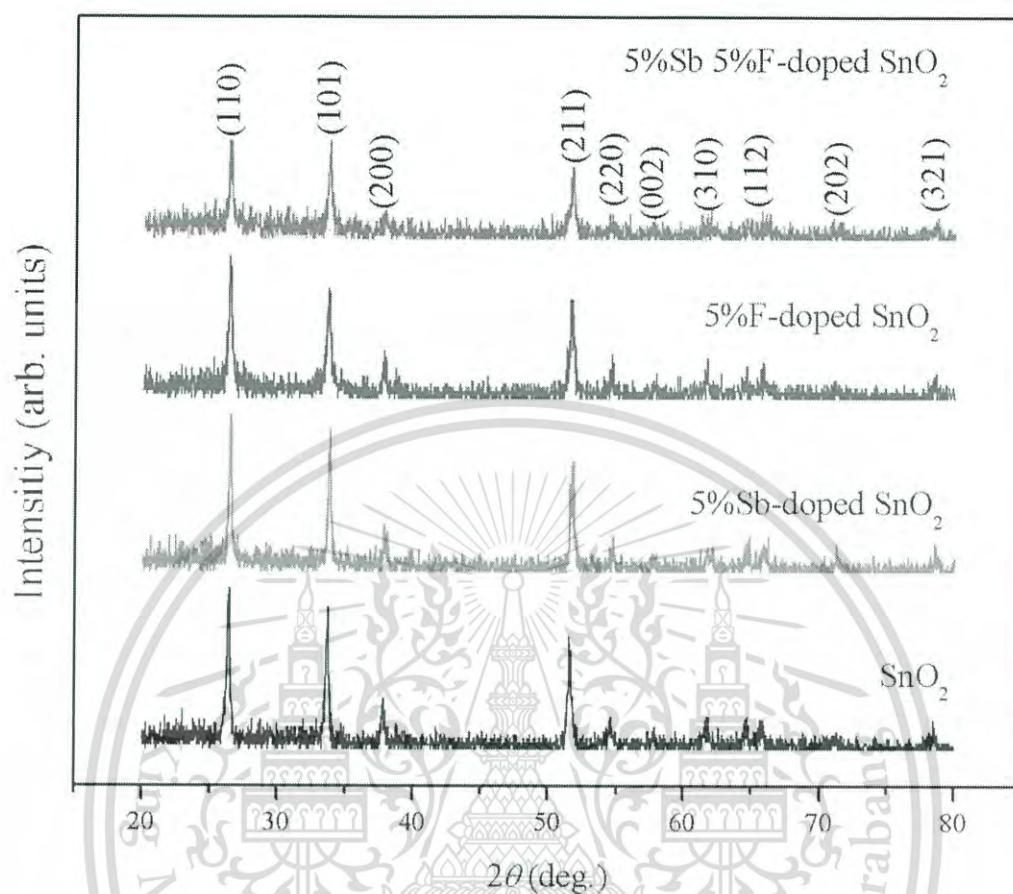


Figure 4.15 XRD patterns of the undoped  $\text{SnO}_2$ , ATO, FTO and AFTO nanofibers calcined at  $600^\circ\text{C}$ .

The FTIR measurements were carried out and relevant results were depicted in Figure 4.16, confirming the good formation of undoped and doped  $\text{SnO}_2$ . The absorption peaks at  $1641\text{ cm}^{-1}$ ,  $1453\text{ cm}^{-1}$  and  $1286\text{ cm}^{-1}$  of as-synthesized  $\text{SnO}_2$  sample can be ascribed to the C=O stretching,  $\text{CH}_2$  scissor and C-N stretching of PVP molecule that is a template for fiber formation during electrospinning process. [65] However, for the samples obtained after calcination at  $600^\circ\text{C}$ , Sn-O stretching of  $\text{SnO}_2$  bands in range of  $450 - 600\text{ cm}^{-1}$  are only found with disappearance of PVP bands. This feature strongly ascertains the simultaneously complete decomposition of PVP and formation of  $\text{SnO}_2$ , ATO, FTO and AFTO nanofibers after calcination beyond certain temperature of  $600^\circ\text{C}$ .

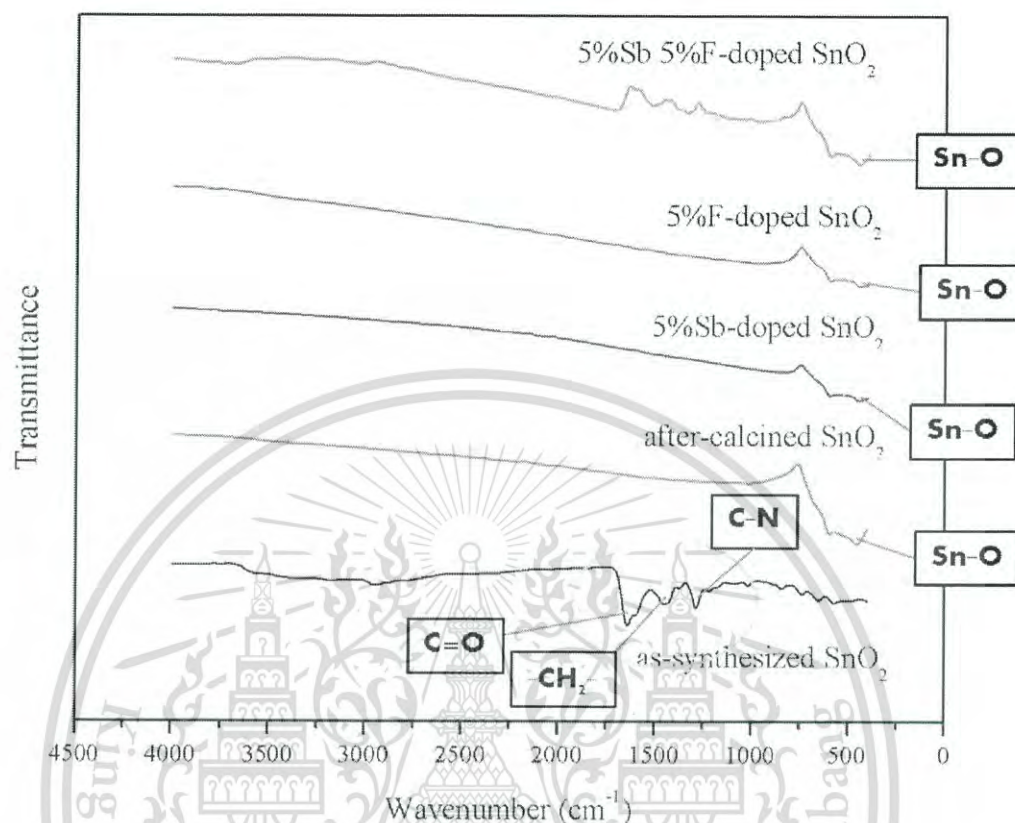


Figure 4.16 FTIR spectra of an as-synthesized and after-calcined  $\text{SnO}_2$ , ATO, FTO and AFTO nanofibers.

#### 4.1.7 Synthesized Ag doped $\text{SnO}_2$ ( $\text{Ag}/\text{SnO}_2$ ), Ag doped $\text{Sb}/\text{SnO}_2$ ( $\text{Ag}/\text{ATO}$ ) and Ag doped $\text{Sb}/\text{F}/\text{SnO}_2$ ( $\text{Ag}/\text{AFTO}$ ) fibers

Figure 4.17 shows the comparison of XRD patterns between  $\text{SnO}_2$  (a) and  $\text{Ag}/\text{SnO}_2$  (b) structure. The  $\text{SnO}_2$  fibers were treated at  $90^\circ\text{C}$  for 2 hours via hydrothermal process that is sufficient to crystallize  $\text{Ag}/\text{SnO}_2$  structure. The diffraction peaks of curve (a) is in good agreement with standard pattern of pure  $\text{SnO}_2$  (JCPDS Card No. 41-1445). Whereas in curve (b), the diffraction peaks of Ag appear that apart from the  $\text{SnO}_2$  peaks, (JCPDS no.: 04-0783) [66], indicating the introduction of Ag into the  $\text{SnO}_2$  phase.

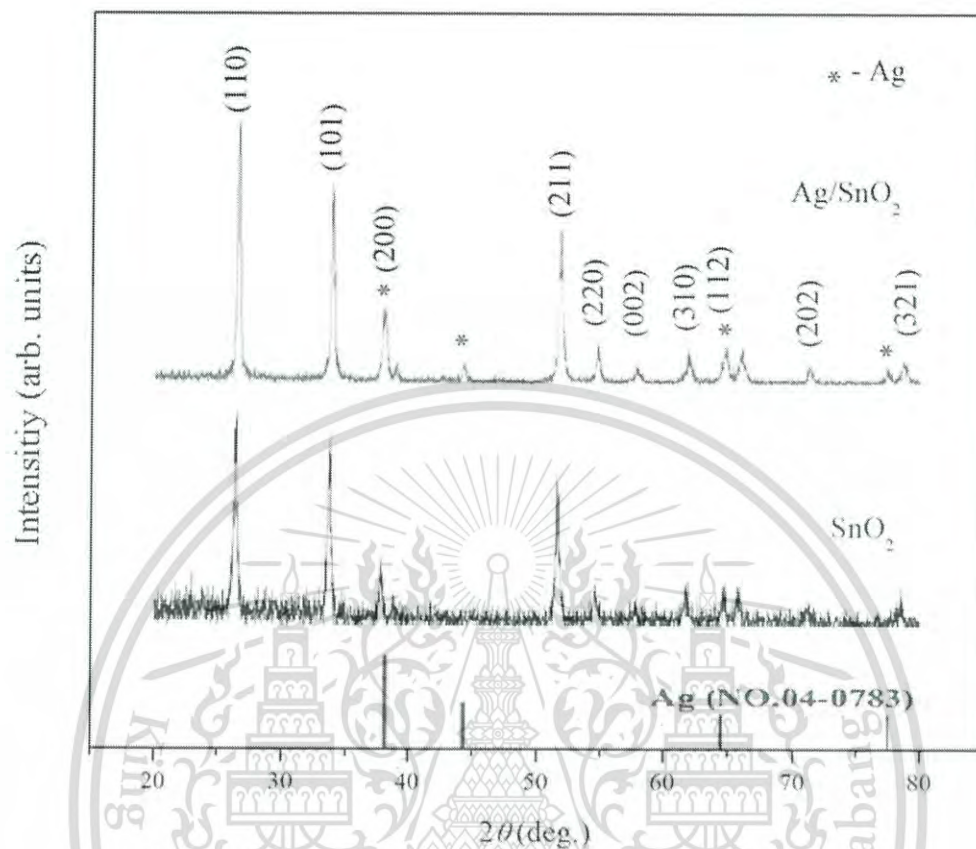


Figure 4.17 XRD patterns of the SnO<sub>2</sub> and Ag/SnO<sub>2</sub> structures.

The diffraction peaks of Ag/ATO prepared with the same method is shown in Figure 4.18. The diffraction peaks of Ag evidently appear in the Ag/ATO curve but is undetectable in the ATO curve. It can be concluded that the Ag/SnO<sub>2</sub> and the Ag/ATO fibers are successfully prepared via the simple hydrothermal process.

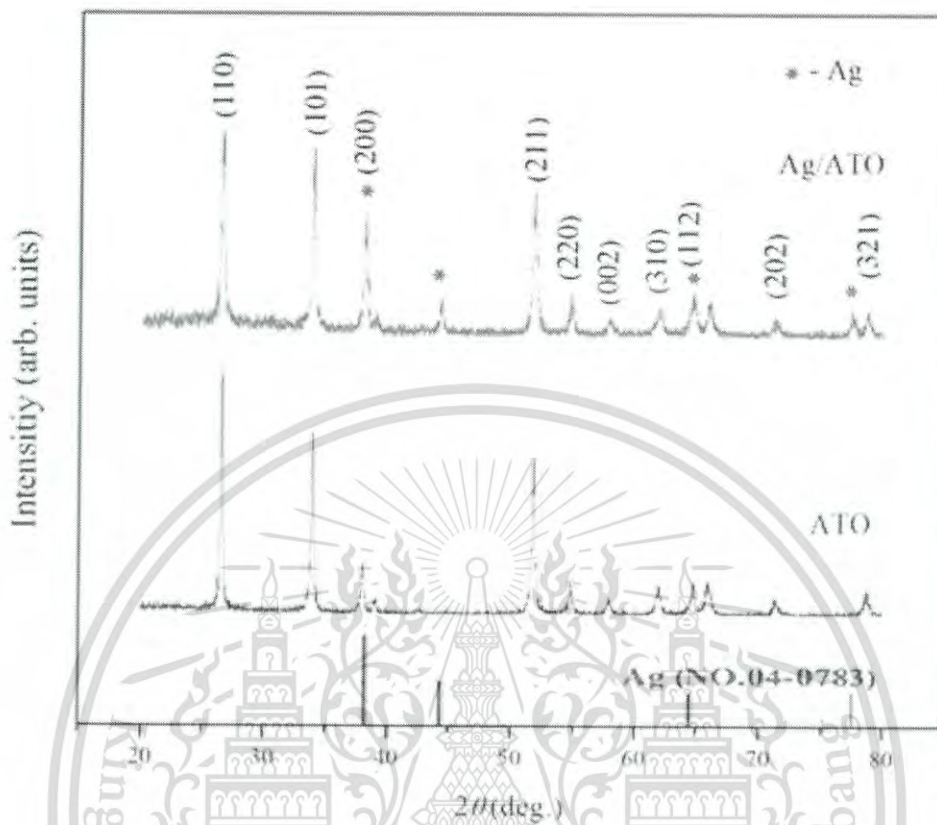


Figure 4.18 XRD patterns of the ATO and Ag/ATO structures.

The SEM results in Figure 4.19 show that the prepared catalysts ( $\text{Ag}/\text{SnO}_2$ ) via hydrothermal process had rough surface morphologies. Some of electrospun  $\text{SnO}_2$  beads in the backbones may be exploded leading to fracture of long chain  $\text{SnO}_2$  structure as seen in Figure 4.19 (a). An analysis of the elemental composition of  $\text{Ag}/\text{SnO}_2$  catalyst was performed using the EDX technique. It is constituted by Ag, Sn and O (Figure 4.19 inset (b)) whereas only Sn and O was detected in the  $\text{SnO}_2$  samples (Figure 4.19 inset (a)). Therefore, the  $\text{Ag}/\text{SnO}_2$  catalyst with the porous structure and high active surface area was successfully synthesized by combination of electrospinning technique and hydrothermal process.

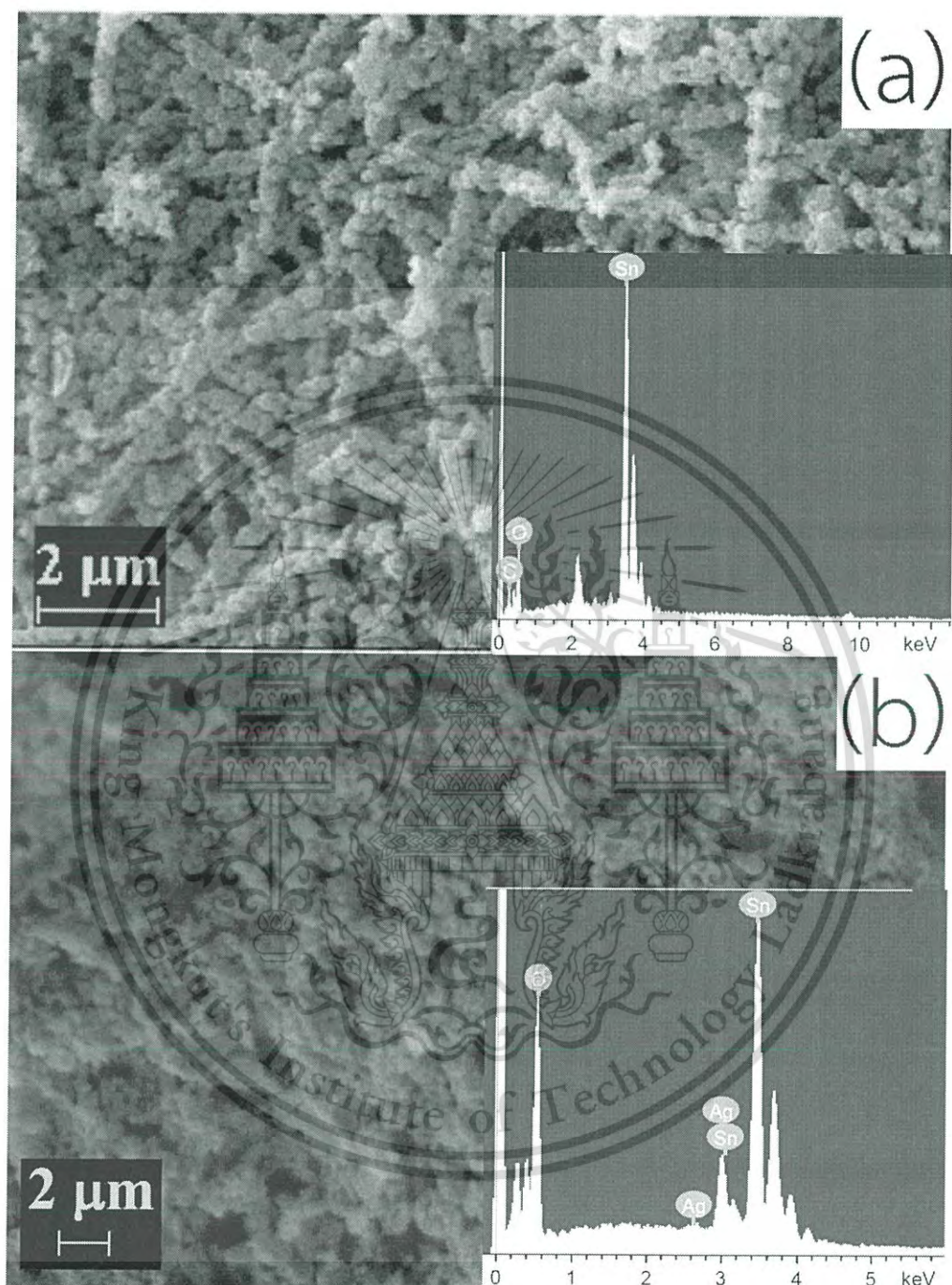


Figure 4.19 SEM images and EDX spectra (inset) of (a) the  $\text{SnO}_2$ , (b)  $\text{Ag/SnO}_2$  structures.

The SEM images of ATO and Ag/ATO are represented in Figure 4.20 (a) and (b), respectively. This result is similar to the SnO<sub>2</sub> and Ag/ SnO<sub>2</sub> catalyst. The long chain structure of ATO was destroyed under high pressure in the hydrothermal process. The EDX spectrum in Figure 4.20 inset (a) and (b) confirm the formation of ATO and Ag/ATO structures. The element of Sb, Sn and O were detected in the ATO samples whereas Ag, Sb, Sn and O were found in the Ag/ATO catalyst.



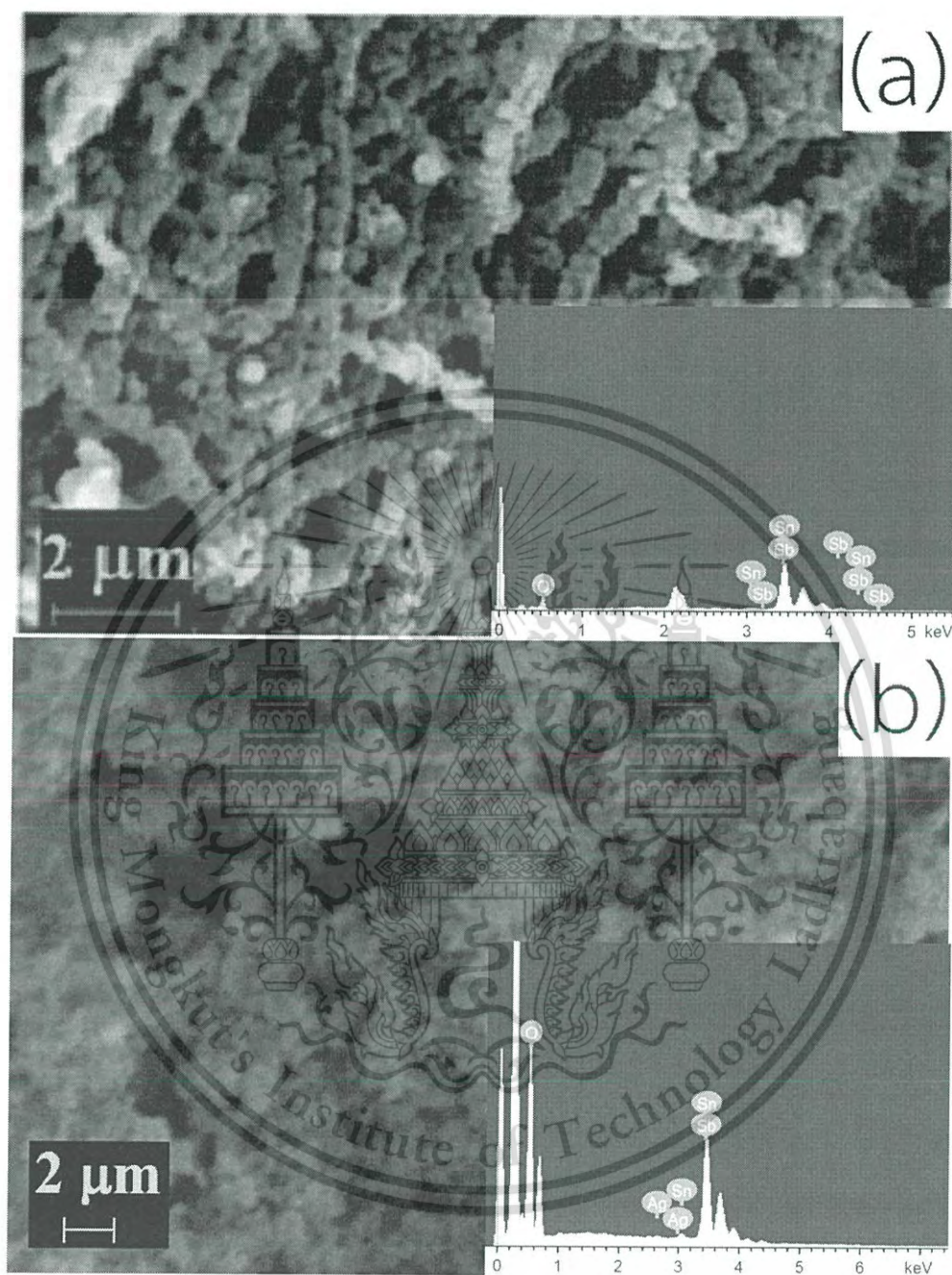


Figure 4.20 SEM images and EDX spectra (inset) of (a) the ATO, (b) Ag/ATO structures.

#### 4.1.8 Ethanol oxidation reaction based on Ag/SnO<sub>2</sub> electrocatalysts

Figure 4.21 shows voltammetric curves for ethanol oxidation over the Ag/SnO<sub>2</sub>/FTO, the SnO<sub>2</sub>/FTO and bare FTO electrode in a 1.0 M ethanol in 1.0 M H<sub>2</sub>SO<sub>4</sub> solution at room temperature. The rather weak reactivity of ethanol at the Ag/SnO<sub>2</sub>/FTO electrode is detected whereas no visible ethanol oxidation peak can be seen on the voltammogram for the SnO<sub>2</sub>/FTO and bare FTO electrode in 1.0 M H<sub>2</sub>SO<sub>4</sub> solution. For Ag/SnO<sub>2</sub>/FTO electrode, the oxidation wave of ethanol appears as potential is in the range of 0.2 and 0.4 V. Ag/AgCl electrode gives the current of approximately 1.5 μA. On the other hand, no visible oxidation wave can be seen on the voltammogram for SnO<sub>2</sub>/FTO electrode and bare FTO electrode.

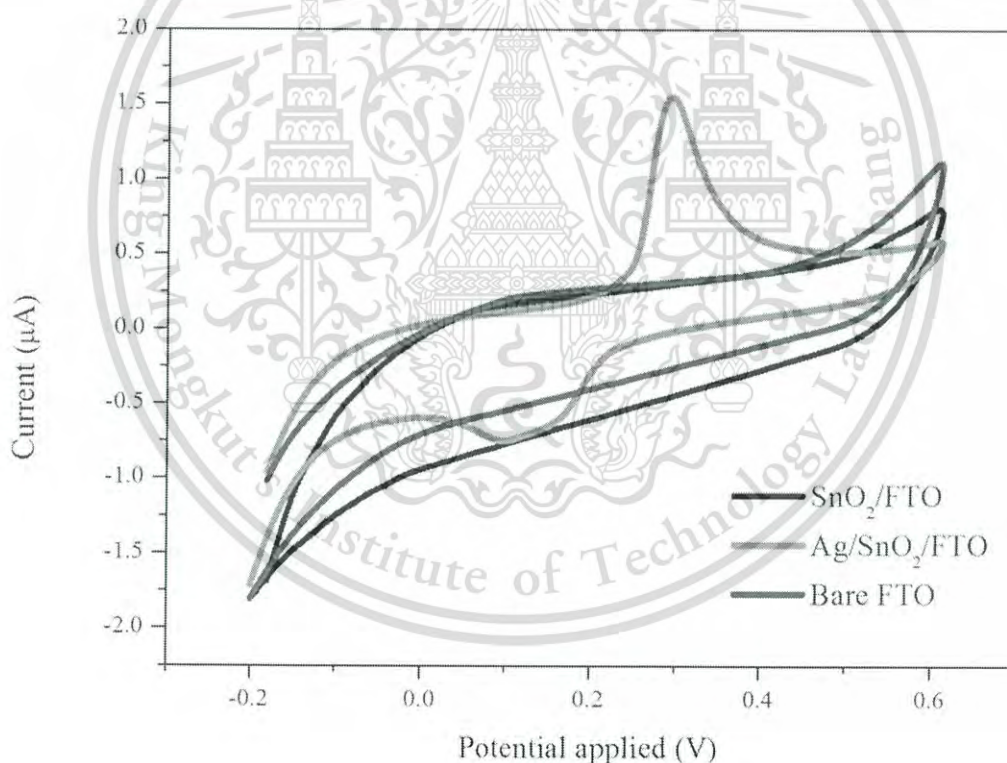
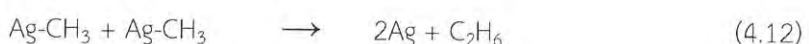
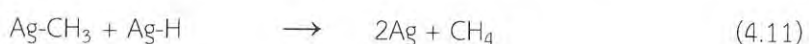
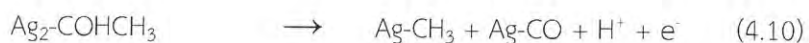
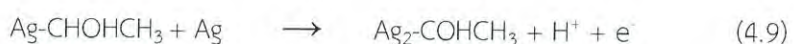
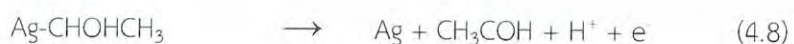
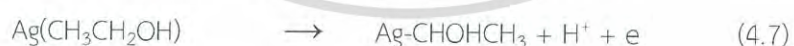


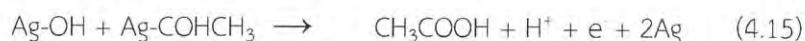
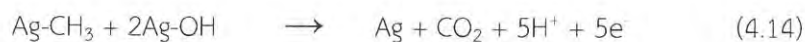
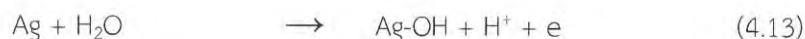
Figure 4.21 Comparison of voltammetric curves for Ag/SnO<sub>2</sub>, SnO<sub>2</sub> supported on FTO electrode and bare FTO electrode in 1.0 M ethanol with 1.0 M H<sub>2</sub>SO<sub>4</sub> solution. Scan rate: 50 mV/s.

One pathway of the oxidation of ethanol ( $\text{CH}_3\text{CH}_2\text{OH}$ ) in equation (4.3) is the complete oxidation of  $\text{CH}_3\text{CH}_2\text{OH}$  to  $\text{CO}_2$  by achieving 12 electrons. In fact, the unexpected pathway of partial oxidation of an ethanol molecule to acetaldehyde ( $\text{CH}_3\text{CHO}$ ) by achieving 2 electrons or to acetate ( $\text{CH}_3\text{COOH}$ ) by achieving 4 electrons can be occurred. Equation (4.3) shows the complete oxidation of ethanol whereas equation (4.4) and equation (4.5) indicate the partial oxidation of ethanol without the breaking of the C–C bond resulting in a significant decrease of the energy content. [67–68]



The oxidation of ethanol generates through different pathways on the electrocatalyst surface. The C–C bond in ethanol leads to a rather complicated reaction mechanism and formation of many intermediates. It should be noted that some intermediates are possible to leave the electrode surface to the solution as the incomplete by-products, such as  $\text{CH}_3\text{COOH}$ ,  $\text{CH}_3\text{CHO}$ ,  $\text{CH}_4$  and  $\text{CH}_3\text{CH}_3$  etc. Thus, it is more difficult to clarify the mechanism of ethanol electro-oxidation [69]. However, the estimate mechanism of the oxidation of ethanol via Ag catalyst could be proposed as following consecutive reactions:

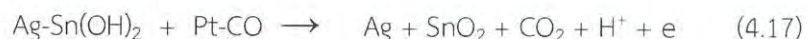




The first step of the oxidation of ethanol is the adsorption process with the silver surface as described by equation (4.6). Hydrogen atom at the  $\alpha$ -carbon of ethanol can be desorbed to generate the alcohol derivative ( $\text{Ag-CHOHCH}_3$ ) following equation (4.7). The alcohol derivative in equation (4.8) dehydrogenates to final product of stable acetaldehyde ( $\text{CH}_3\text{COH}$ ). As a result, the electrooxidation of ethanol may discontinue by achieving 2 electrons. On the other hand, the alcohol derivative in equation (4.9) can deprotonate to acetaldehyde and break of C-C bond could be occurred to achieve adsorbed methyl ( $\text{Ag-CH}_3$ ) and carbon monoxide ( $\text{Ag-CO}$ ) on Ag electrocatalyst as expressed in equation (4.10). From this situation, the adsorbed methyl group existed in equation (4.10) can combine with another methyl groups to form ethane ( $\text{C}_2\text{H}_6$ ) (Eq. 4.12) or the proton to form methane ( $\text{CH}_4$ ) (Eq. 4.11). However, the  $\text{CH}_x$  species and CO species could destroy the electrocatalyst surface and reduce the charge transfer rate of the ethanol oxidation reaction. In equation (4.14), the -OH species from the water dissociation (Eq. 4.13) on the active surface site could react with the adsorbed methyl species to obtain the complete ethanol oxidation reaction. On the other hand, the adsorbed OH species can react with the adsorbed acetaldehyde species to give acetic acid (Eq. 4.15) which is the product of partial ethanol oxidation reaction. [70, 71] In fact, the complete oxidation of ethanol into  $\text{CO}_2$  via C-C bond cleavage is dramatically difficult. The electrooxidation of ethanol via several electrocatalysts is almost produced from partial oxidation of ethanol to acetaldehyde or acetic acid. Only 1 % of ethanol is completely oxidized into  $\text{CO}_2$  on the electrocatalyst surface at room temperature [72, 73].

The addition  $\text{SnO}_2$  nanoparticles as a support catalyst with the Ag electrocatalyst leads to significantly enhanced activity.  $\text{SnO}_2$  can remove the adsorbed intermediates and improve Ag surface area for the quick dissociation of ethanol. The equation (4.16)

shows the dissociation water with SnO<sub>2</sub> particles to form -OH species at the Ag surface area.



Sn(OH)<sub>2</sub> species at the Ag surface was introduced to increase the partial oxidation products which leads to increasing current densities. The formation of Sn(OH)<sub>2</sub> species from equation (4.16) on the electrocatalyst surface leads to a removal the adsorbed CO and increases the Ag surface area as mentioned in equation (4.17). After that, the reaction barrier for C-C bond splitting of ethanol and CO<sub>2</sub> production is increased. Therefore, the presence of SnO<sub>2</sub> support catalyst could induce significant increase in catalytic activity of Ag electrocatalyst to catalyze the full oxidation of ethanol. However, the single SnO<sub>2</sub> support catalyst is insufficient for the electrooxidation of ethanol. [74, 75]

Figure 4.22 shows voltammetric curves for ethanol oxidation over the Ag/ATO/FTO, the ATO/FTO and bare FTO electrode in a 1.0 M ethanol in 0.1 M H<sub>2</sub>SO<sub>4</sub> solution at room temperature. For Ag/ATO/FTO electrode, the oxidation peak of ethanol appears for potential range of 0.2-0.3 V. Ag/AgCl electrode, then gives the current about 1.0 μA. Furthermore, the noticeable oxidation wave appears around 0.5 V. On the other hand, no visible oxidation peak can be seen on the voltammogram for ATO electrode as same as SnO<sub>2</sub> electrode.

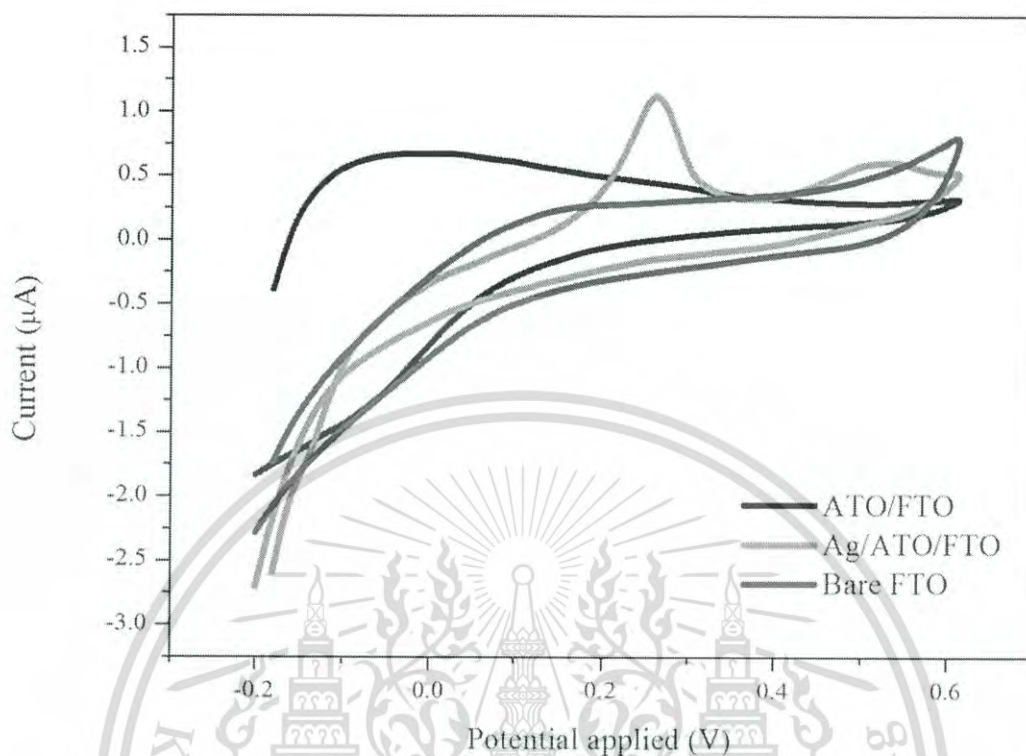


Figure 4.22 Comparison of voltammetric curves for Ag/ATO, ATO supported on FTO electrode and bare FTO electrode in 1.0 M ethanol with 1.0 M  $\text{H}_2\text{SO}_4$  solution. Scan rate: 50 mV/s.

Figure 4.23 shows voltammetric curves for ethanol oxidation over the  $\text{Ag}/\text{SnO}_2/\text{FTO}$ , the  $\text{Ag}/\text{ATO}/\text{FTO}$  and  $\text{Ag}/\text{AFTO}/\text{FTO}$  electrode in a 1.0 M ethanol in 1.0 M  $\text{H}_2\text{SO}_4$  solution at room temperature. For  $\text{Ag}/\text{SnO}_2/\text{FTO}$  and  $\text{Ag}/\text{ATO}/\text{FTO}$  electrode, they give current of the oxidation peak approximately 1.5 and 1.0  $\mu\text{A}$  as potential is swept between 0.2 and 0.4 V vs.  $\text{Ag}/\text{AgCl}$  electrode, respectively. Although antimony doped tin oxide (ATO) generated the larger number of oxygen vacancies to promote the electro-oxidation of CO intermediate species, the current of the ethanol oxidation peak of  $\text{Ag}/\text{SnO}_2/\text{FTO}$  and  $\text{Ag}/\text{ATO}/\text{FTO}$  electrode are insignificantly distinguished. On the other hand, no visible oxidation peak can be seen on the voltammogram for  $\text{Ag}/\text{AFTO}/\text{FTO}$  electrode. The possible reason is the intensive of AFTO cluster structure that obscure Ag metal atom to catalyze the ethanol oxidation reaction.

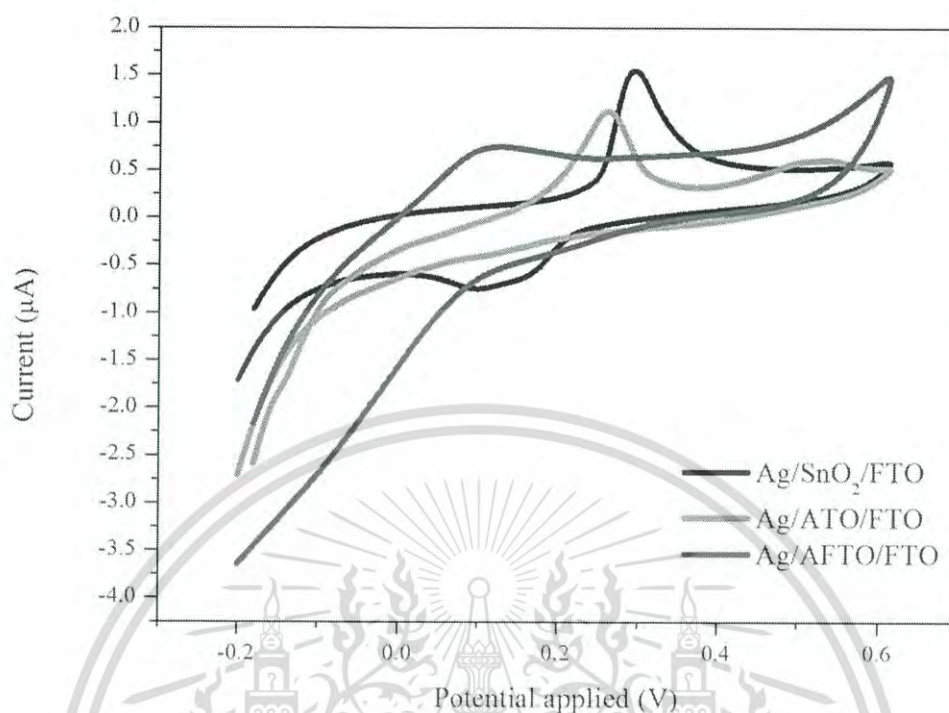


Figure 4.23 Comparison of voltammetric curves for Ag/SnO<sub>2</sub>, Ag/ATO and Ag/AFTO electrode in 1.0 M ethanol with 1.0 M H<sub>2</sub>SO<sub>4</sub> solution. Scan rate: 50 mV/s.

The stability of Ag/SnO<sub>2</sub>, Ag/ATO and Ag/AFTO catalysts were investigated by chronoamperometry technique. The chronoamperometry curves of Ag/SnO<sub>2</sub>, Ag/ATO and Ag/AFTO catalysts were recorded at a constant potential in a solution containing 1.0 M Ethanol with 1.0 M H<sub>2</sub>SO<sub>4</sub> as shown in Figure 4.24.

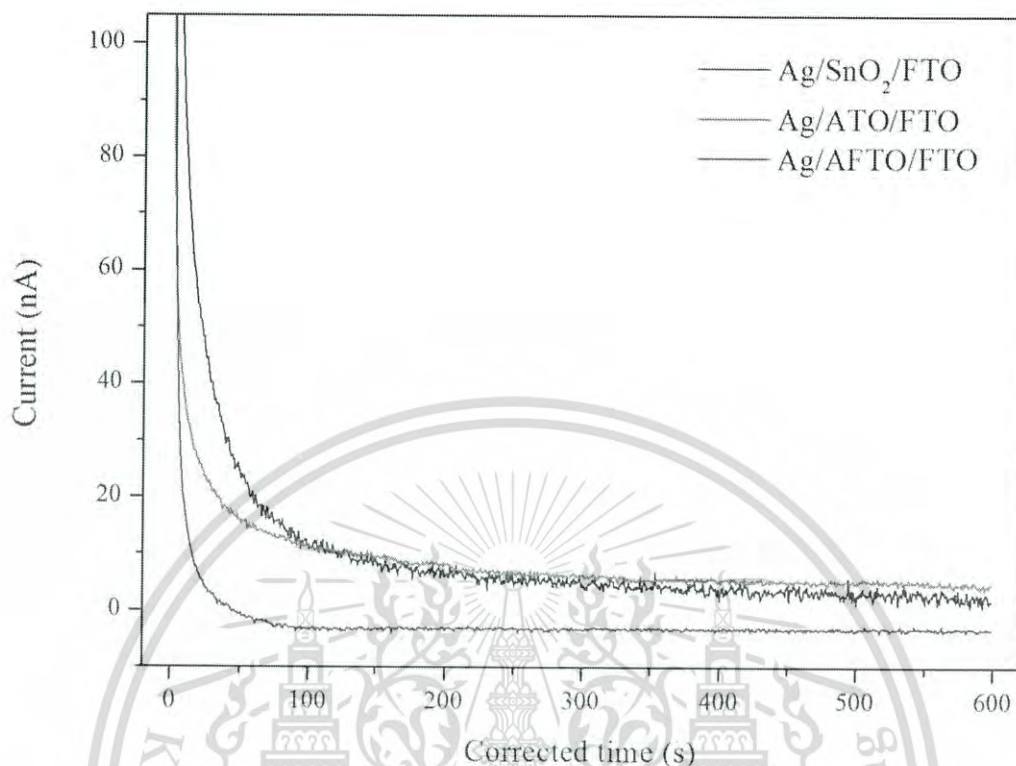


Figure 4.24 Chronoamperograms of Ag/SnO<sub>2</sub>/FTO, Ag/ATO/FTO and Ag/AFTO/FTO electrode at 0.25 V in 1.0 M ethanol with 1.0 M H<sub>2</sub>SO<sub>4</sub> solution.

At the preliminary stage, the current of these catalysts dropped rapidly but the current of Ag/SnO<sub>2</sub> and Ag/ATO were obviously higher than Ag/AFTO after 100 s at a fixed potential. At 600 s, Ag/SnO<sub>2</sub> and Ag/ATO was approximately 10 times higher than Ag/AFTO. Based on correlated theory, the ethanol oxidation reaction gave some intermediate species such as CO that can be accumulated on the surface of Ag catalysts. If the intermediate species were slowly removed, the current will drop rapidly. A slow depreciate of current with time implies that the electrocatalyst has excellent anti-poisoning ability. As a result, Ag metal atoms on the surface of SnO<sub>2</sub> or ATO also are expected to accelerate the oxidation reaction of ethanol. Hence, the increase of SnO<sub>2</sub> or ATO dispersed clusters is helpful to improve the stability of the Ag catalyst.

## Chapter 5

# Conclusions and Suggestions

### 5.1 Conclusion

Ag/ SnO<sub>2</sub> and Ag/ ATO catalyst were successfully synthesized by combining two techniques which is easy to operate with cost-effectiveness. The first step was conducted on the fabrication of support catalyst based on SnO<sub>2</sub> by electrospinning technique followed by calcination process. The obtained fibers were treated with hydrothermal reaction to provide the candidate of electrooxidation ethanol catalyst. Difference of PVP concentrations in precursor solution and antimony doping concentrations were investigated to acknowledge the appropriate morphologies. The morphologies of the as-spun nanofibers were in the form of long chains of smooth nanofibers. The average diameter of fibers increased and the beads in fibers were lower when the polymer concentration was increased. The polymer template was burnt out while Sn precursor was oxidized by calcination process. All of characterization results advised that tin-based precursors were completely transformed into SnO<sub>2</sub> when the products were calcined at 600 °C for 3 hours. The morphologies of the fibers were found to be dense with uniform contribution of nanobeads in form of porous fibrous structure. It implies that the solvent evaporation, decomposition of polymer and phase separation plays a key role in the formation of SnO<sub>2</sub> with different morphologies. The EDX spectra and XRD patterns confirmed the existence of relevant elements and the formation of SnO<sub>2</sub> synthesized by these processes. Sb-doped SnO<sub>2</sub> (ATO) nanofibers have been comfortably synthesized by electrospinning technique and suitable calcination. Varying Sb concentration in doping process has the significant influence on morphologies of ATO nanofibers. The higher Sb doping concentration in ATO nanofiber has more fibrous network morphology while it still possesses good crystalline structure. The obtained Ag/SnO<sub>2</sub> and Ag/ATO catalyst from hydrothermal reaction showed a rough surface and porous structure that could be utilized to catalyze in ethanol oxidation reaction. The electrocatalytic activity of Ag/SnO<sub>2</sub> and Ag/ATO catalyst for ethanol electrooxidation was evaluated in acidic

medium. The obtained current of the oxidation peak approximately about 1.5 and 1.0  $\mu\text{A}$  at the potentials range of 0.2- 0.4 V vs. Ag/AgCl electrode for Ag/SnO<sub>2</sub>/FTO and Ag/ATO/FTO electrode, respectively. The electrocatalytic activity and stability of Ag/SnO<sub>2</sub> and Ag/ATO for ethanol electrooxidation was greater than that of Ag/AFTO catalyst. It can conclude that, Ag on the surface of SnO<sub>2</sub> or ATO support catalyst can be used to oxidize ethanol. The enhanced electrochemical properties of SnO<sub>2</sub> or ATO support catalyst could be interpreted by the bi-functional mechanism.

## 5.2 Suggestions

The Ag/SnO<sub>2</sub> and Ag/ATO catalyst may be synthesized in form bimetallic catalyst to improve the electrocatalytic activity for ethanol electrooxidation.



## References

- [1] A. Kirubakaran, S. Jain and R.K. Nema, 2009. "A review on fuel cell technologies and power electronic interface". *Renewable and Sustainable Energy Reviews*, 13, 2430–2440.
- [2] H. Bahrami and A. Faghri, 2013. "Review and advances of direct methanol fuel cells: Part II: Modeling and numerical simulation". *Journal of Power Sources*, 230, 303–320.
- [3] H. Gharibi, S. Sadeghi and F. Golmohammadi, 2016. "Electrooxidation of Ethanol on highly active and stable carbon supported PtSnO<sub>2</sub> and its application in passive direct ethanol fuel cell: Effect of tin oxide synthesis method". *Electrochimica Acta*, 190, 1100–1112.
- [4] M.A.F. Akhairi and S.K. Kamarudin, 2016. "Catalysts in direct ethanol fuel cell (DEFC): An overview". *International Journal of Hydrogen Energy*, 41, 4214–4228.
- [5] S.P.S. Badwal, S. Giddey, A. Kulkarni, J. Goel and S. Basu, 2015. "Direct ethanol fuel cells for transport and stationary applications – A comprehensive review". *Applied Energy*, 145, 80–103.
- [6] W.J. Zhou, S.Q. Song, W.Z. Li, G.Q. Sun, Q. Xin, S. Kontou, K. Pouliaitis and P. Tsiakaras, 2004. "Pt-based anode catalysts for direct ethanol fuel cells". *Solid State Ionics*, 175, 797–803.
- [7] M.Z.F. Kamarudin, S.K. Kamarudin, M.S. Masdar and W.R.W. Daud, 2013. "Review: Direct ethanol fuel cells". *International Journal of Hydrogen Energy*, 38, 9438–9453.
- [8] D.-J. Guo, 2011. "Electrooxidation of ethanol on novel multi-walled carbon nanotube supported platinum–antimony tin oxide nanoparticle catalysts". *Journal of Power Sources*, 196, 679–682.
- [9] Z.L. Liu, X.Y. Ling, X.D. Su and J.Y. Lee, 2004. "Carbon-supported Pt and PtRu nanoparticles as catalysts for a direct methanol fuel cell". *Journal of Physical Chemistry B*, 108, 8234–8240.

- [10] E.S. Steigerwalt, G.A. Deluga, D.E. Cliffel and C.M. Lukehart, 2001. "A Pt-Ru/Graphitic Carbon Nanofiber Nanocomposite Exhibiting High Relative Performance as a Direct-Methanol Fuel Cell Anode Catalyst". *Journal of Physical Chemistry B*, 105, 8097–8101.
- [11] C. Lamy, S. Rousseau, E. Belgsir, C. Coutanceau and J.-M. Léger, 2004. "Recent progress in the direct ethanol fuel cell: development of new platinum–tin electrocatalysts". *Electrochimica Acta*, 49, 3901–3908.
- [12] H.J. Kim, D.Y. Kim, H. Han and Y.J. Shul, 2006. "PtRu/C-Au/TiO<sub>2</sub> electrocatalyst for a direct methanol fuel cell". *Journal of Power Sources*, 159, 484–490.
- [13] P. Justin and R.G. Ranga, 2009. "Enhanced activity of methanol electro-oxidation on Pt–V<sub>2</sub>O<sub>5</sub>/C catalysts". *Catalysis Today*, 141, 138–143.
- [14] Y.X. Bai, J.J. Wu, J.Y. Xi, J.S. Wang, W.T. Zhu, L.Q. Chen, X.P. Qiu and D.J. Guo, 2005. "Electrochemical oxidation of ethanol on Pt–ZrO<sub>2</sub>/C catalyst". *Electrochemistry Communications*, 7, 1087–1090.
- [15] M.S. Saha, R.Y. Li and X.L. Sun, 2007. "Composite of Pt–Ru supported SnO<sub>2</sub> nanowires grown on carbon paper for electrocatalytic oxidation of methanol". *Electrochemistry Communications*, 9, 2229–2234.
- [16] X.Z. Chui, F.M. Cui, Q.J. He, L.M. Guo, M.L. Ruan and J.L. Shi, 2010. "Graphitized mesoporous carbon supported Pt–SnO<sub>2</sub> nanoparticles as a catalyst for methanol oxidation". *Fuel*, 89, 372–377.
- [17] X. Zhang, H. Zhu, Z. Guo, Y. Wei and F. Wang, 2010. "Design and preparation of CNT@ SnO<sub>2</sub> core-shell composites with thin shell and its application for ethanol oxidation". *International Journal of Hydrogen Energy*, 35, 8841–8847.
- [18] L. Jiang, L. Colmenares, Z. Jusys, G. Sun and R. Behm, 2007. "Ethanol electrooxidation on novel carbon supported Pt/SnO<sub>x</sub>/C catalysts with varied Pt: Sn ratio". *Electrochimica Acta*, 53, 377–389.

- [19] R. Noonuruk, N. Vittayakorn, W. Mekprasart, J. Sritharathikhun and W. Pecharapa, 2015. "Sb-doped SnO<sub>2</sub> nanoparticles synthesized by sonochemical-assisted precipitation process". *Journal of nanoscience and nanotechnology* 15, 2564-2569.
- [20] C. Pan, Y. Li, Y. Ma, X. Zhao and Q. Zhang, 2011. "Platinum-antimony doped tin oxide nanoparticles supported on carbon black as anode catalysts for direct methanol fuel cells". *Journal of Power Sources*, 196, 6228-6231.
- [21] M. Batzill and U. Diebold, 2005. "The surface and materials science of tin oxide". *Progress in Surface Science*, 79, 47-154.
- [22] Q. Wali, A. Fakharuddin and R. Jose, 2015. "Tin oxide as a photoanode for dye-sensitised solar cells: Current progress and future challenges". *Journal of Power Sources*, 293, 1039-1052.
- [23] S. Ramakrishna, K. Fujihara, W.-E. Teo, T.-C. Lim and Z. Ma, 2005. *An introduction to electrospinning and nanofibers*. New York : World Scientific Publishing.
- [24] N. Bhardwaj and S.C. Kundu, 2010. "Electrospinning: A fascinating fiber fabrication technique". *Biotechnology Advances*, 28, 325-347.
- [25] Z.-M. Huang, Y.-Z. Zhang, M. Kotaki and S. Ramakrishna, 2003. "A review on polymer nanofibers by electrospinning and their applications in nanocomposites". *Composites Science and Technology*, 63, 2223-2253.
- [26] J. Doshi and D.H. Reneker, 1995. "Electrospinning process and applications of electrospun fibers", *Journal of Electrostatics*, 35, 151-160.
- [27] Z. Li and C. Wang, 2013. *One-dimensional nanostructures electrospinning technique and unique nanofibers*. Heidelberg : Springer Publishing.
- [28] W.K. Son, J.H. Youk, T.S. Lee and W.H. Park, 2004. "The effects of solution properties and polyelectrolyte on electrospinning of ultrafine poly(ethylene oxide) fibers". *Polymer*, 45, 2959-2966.

- [29] J.M. Deitzel, J. Kleinmeyer, D. Harris and N.C.B. Tan, 2001. "The effect of processing variables on the morphology of electrospun nanofibers and textiles". *Polymer*, 42, 261–272.
- [30] J. Muangban and P. Jaroenapibal, 2014. "Effects of precursor concentration on crystalline morphologies and particle sizes of electrospun  $\text{WO}_3$  nanofibers". *Ceramics International*, 40, 6759– 6764.
- [31] S.P.S. Badwal, S. Giddey, A. Kulkarni, J. Goel and S. Basu, 2015. "Direct ethanol fuel cells for transport and stationary applications – A comprehensive review". *Applied Energy*, 145, 80–103.
- [32] P. Barbaro and C. Bianchini, 2009. *Catalysis for sustainable energy production*. Weinheim : WILEY-VCH Publishing.
- [33] H.R. Corti and E.R. Gonzalez, 2014. *Direct alcohol fuel cells*. Dordrecht : Springer Publishing.
- [34] X. Li and A. Faghri, 2013. "Review and advances of direct methanol fuel cells (DMFCs) part I: Design, fabrication, and testing with high concentration methanol solutions". *Journal of Power Sources*, 226, 223-240.
- [35] W. Zhou, Z. Zhou, S. Song, W. Li, G. Sun, P. Tsiakaras and Q. Xin, 2003. "Pt based anode catalysts for direct ethanol fuel cells". *Applied Catalysis B: Environmental*, 46, 273–285.
- [36] Y. Wang, S. Zou and W.-B. Cai, 2015. "Recent advances on electro-oxidation of ethanol on Pt- and Pd-based catalysts: from reaction mechanisms to catalytic Materials". *catalysts*, 5, 1507-1534.
- [37] L. Cheng, S.Y. Ma, T.T. Wang, X.B. Li, J. Luo, W.Q. Li, Y.Z. Mao and D.J. GZ, 2014. "Synthesis and characterization of  $\text{SnO}_2$  hollow nanofibers by electrospinning for ethanol sensing properties". *Materials Letters*, 131, 23–26.
- [38] L. Li, X. Yin, S. Liu, Y. Wang, L. Chen and T. Wang, 2010. "Electrospun porous  $\text{SnO}_2$  nanotubes as high capacity anode materials for lithium ion batteries". *Electrochemistry Communications*, 12, 1383–1386.

- [39] W.Q. Li, S.Y. Ma, J. Luo, Y.Z. Mao, L. Cheng, D.J. Gengzang, X.L. Xu and S.H. Yan, 2014. "Synthesis of hollow SnO<sub>2</sub> nanobelts and their application in acetone sensor". *Materials Letters*, 132, 338–341.
- [40] Y. Zhang, J. Li, G. An and X. He, 2010. "Highly porous SnO<sub>2</sub> fibers by electrospinning and oxygen plasma etching and its ethanol-sensing properties". *Sensors and Actuators B: Chemical*, 144, 43–48.
- [41] X. Wang, H. Fan and P. Ren, 2013. "Electrospinning derived hollow SnO<sub>2</sub> microtubes with highly photocatalytic property". *Catalysis Communications*, 31, 37–41.
- [42] Y.-E Miao, S. He, Y. Zhong, Z. Yang, W. W. Tjiu and T. Liu, 2013. "A novel hydrogen peroxide sensor based on Ag/SnO<sub>2</sub> composite nanotubes by electrospinning". *Electrochimica Acta*, 99, 117–123.
- [43] P. Zhang, L. Wang, X. Zhang, C. Shao, J. Hu and G. Shao, 2015. "SnO<sub>2</sub>-core carbon-shell composite nanotubes with enhanced photocurrent and photocatalytic performance". *Applied Catalysis B: Environmental*, 166–167, 193–201.
- [44] A.B. Suryamas, G.M. Anilkumar, S. Sago, T. Ogi and K. Okuyama, 2013. "Electrospun Pt/SnO<sub>2</sub> nanofibers as an excellent electrocatalysts for hydrogen oxidation reaction with ORR-blocking characteristic". *Catalysis Communications*, 33, 11–14.
- [45] X. Wang, H. Fan and P. Ren, 2013. "Self-assemble flower-like SnO<sub>2</sub>/Ag heterostructures: Correlation among composition, structure and photocatalytic activity". *Colloids and Surfaces A: Physicochem. Eng. Aspects*, 419, 140–146.
- [46] F. Zhang, Z. Cheng, L. Kang, L. Cui, W. Liu, X. Xu, G. Hou and H. Yang, 2015. "A novel preparation of Ag-doped TiO<sub>2</sub> nanofibers with enhanced stability of photocatalytic activity†". *The Royal Society of Chemistry*, 5, 32088–32091.
- [47] D.-J. Guo, 2011. "Electrooxidation of ethanol on novel multi-walled carbon nanotube supported platinum–antimony tin oxide nanoparticle catalysts". *Journal of Power Sources*, 196, 679–682.

- [48] C. Pan, Y. Li, Y. Ma, X. Zhao and Q. Zhang, 2011. "Platinum–antimony doped tin oxide nanoparticles supported on carbon black as anode catalysts for direct methanol fuel cells". *Journal of Power Sources*, 196, 6228–6231.
- [49] J. Flórez-Montaño, G. García, O. Guillén-Villafuerte, J.L. Rodríguez, G.A. Planes and E. Pastor, 2016. "Mechanism of ethanol electrooxidation on mesoporous Pt electrode in acidic medium studied by a novel electrochemical mass spectrometry set-up". *Electrochimica Acta*, 209, 121–131.
- [50] R.M. Antonias, A. Oliveira Neto, M. Linardi and E.V. Spinace, 2013. "The effect of acetaldehyde and acetic acid on the direct ethanol fuel cell performance using PtSnO<sub>2</sub>/C electrocatalysts". *International journal of hydrogen energy*, 38, 2069–2077.
- [51] J.W. Magee, W.-P. Zhou and M.G. White, 2014. "Promotion of Pt surfaces for ethanol electro-oxidation by the addition of small SnO<sub>2</sub> nanoparticles: Activity and mechanism". *Applied Catalysis B: Environmental*, vol. 152–153, 397–402.
- [52] J. Selva, S.E. Martinez, D. Buceta, M.J. Rodriguez-Vazquez, M.C. Blanco, M.A. Lopez-Quintela, and G. Egea, 2010. "Silver Sub-nanoclusters Electrocatalyze Ethanol Oxidation and Provide Protection against Ethanol Toxicity in Cultured Mammalian Cells". *Journal of American Chemical Society*, 132, 6947–6954.
- [53] N. Bhardwaj and S.C. Kundu, 2010. "Electrospinning: A fascinating fiber fabrication technique". *Biotechnology Advances*, 28, 325–347.
- [54] X. Xia, X. J. Dong, Q. F. Wei, Y. B. Cai, and K. Y. Lu, 2012. "Formation mechanism of porous hollow SnO<sub>2</sub> nanofibers prepared by one-step electrospinning". *EXPRESS Polymer Letters*, 6, 169–176.
- [55] H. H. Son and W. G. Lee, 2012. "Annealing effects for calcination of tin oxide powder prepared via homogeneous precipitation". *Journal of Industrial and Engineering Chemistry*. 18, 317-320.
- [56] Z. Li and C. Wang, 2013. *One-Dimensional nanostructures Electrospinning Technique and Unique Nanofibers*. Springer Briefs in Materials.

- [57] W. Q. Li, S. Y. Man, J. Luo, Y. Z. Mao, L. Cheng, D. J. Gengzang, X. L. Xu and S. H. Yan, 2014. "Synthesis of hollow SnO<sub>2</sub> nanobelts and their application in acetone sensor". *Materials Letters*, 132, 338–341.
- [58] X. Wang, H. Fan and P. Ren, 2013 "Electrospinning derived hollow SnO<sub>2</sub> microtubes with highly photocatalytic property". *Catalysis Communications*, 31, 37–41.
- [59] J. Wua, Q. Huang, D. Zeng, S. Zhang, L. Yang, D. Xia, Z. Xiong and C. Xie, 2014. "Al-doping induced formation of oxygen-vacancy for enhancing gas-sensing properties of SnO<sub>2</sub> NTs by electrospinning". *Sensors and Actuators B*, 198, 62–69.
- [60] W. Wang, J. Zhou, S. Zhang, J. Song, H. Duan, M. Zhou, C. Gong, Z. Bao, B. Lu, X. Li, W. Lan and E. Xie, 2010. "A novel method to fabricate silicananotubes based on phase separation effect". *Journal of Materials Chemistry*, 20, 9068–9072.
- [61] R. Noonuruk, N. Vittayakorn, W. Mekprasart, J. Sriharathikhun and W. Pecharapa, 2015. "Sb-doped SnO<sub>2</sub> nanoparticles synthesized by sonochemical-assisted precipitation process". *Journal of nanoscience and nanotechnology* 15, 2564–2569.
- [62] N. Dharmaraj, C. H. Kim, K. W. Kim, H. Y. Kim, E. K. Suh, and K. Y. Lu, 2006. "Spectral studies of SnO<sub>2</sub> nanofibres prepared by electrospinning method". *Spectrochimica Acta Part A*, 64, 136–140.
- [63] Y. Li, J. Wang, B. Feng, K. Duan, and J. Weng, 2015. "Synthesis and characterization of antimony-doped tin oxide (ATO) nanoparticles with high conductivity using a facile ammonia-diffusion co-precipitation method". *Journal of Alloys and Compounds*, 634, 37 – 42.
- [64] E. Elangovan and K. Ramamurthiand, 2005. "A study on low cost-high conducting fluorine and antimony-doped tin oxide thin films". *Applied Surface Science*, 249, 183–196.

- [65] A. M. Abdelghany, M. S. Mekhail, E. M. Abdelrazek, and M. M. Aboud, 2015. "Combined DFT/FTIR structural studies of monodispersed PVP/Gold and silver nano particles". *Journal of Alloys and Compounds*, 646, 326–332.
- [66] X. Wang, H. Fan and P. Ren, 2013. "Self-assemble flower-like SnO<sub>2</sub> /Ag heterostructures: Correlation among composition, structure and photocatalytic activity". *Colloids and Surfaces A: Physicochem. Eng. Aspects*, 419,140–146.
- [67] Y. Wang, S. Zou and W.-B. Cai, 2015. "Recent Advances on Electro-Oxidation of Ethanol on Pt- and Pd-Based Catalysts: From Reaction Mechanisms to Catalytic Materials" *Catalysts*, 5, 1507-1534.
- [68] J. Friedl and U. Stimming, 2013. "Model catalyst studies on hydrogen and ethanol oxidation for fuel cells". *Electrochimica Acta*, 101, 41–58.
- [69] W. Zhou, Z. Zhou, S. Song, W. Li, G. Sun, P. Tsiakaras and Q. Xin, 2003. "Pt based anode catalysts for direct ethanol fuel cells". *Applied Catalysis B: Environmental*, 46, 273–285.
- [70] L. Han, H. Ju and Y. Xu, 2012. "Ethanol electro-oxidation: Cyclic voltammetry, electrochemical impedance spectroscopy and galvanostatic oscillation". *International journal of hydrogen energy*, 37, 15156-15163.
- [71] G. Tremiliosi-Filho, E.R. Gonzalez, A.J. Motheo, E.M. Belgsir, J.-M. Le´ger and C. Lamy, 1998. "Electro-oxidation of ethanol on gold: analysis of the reaction products and mechanism". *Journal of Electroanalytical Chemistry*, 444, 31–39.
- [72] H. Wang, Z. Jusys and R.J. Behm, 2006. "Ethanol electro-oxidation on carbon-supported Pt, PtRu and Pt<sub>3</sub>Sn catalysts: A quantitative DEMS study". *Journal of Power Sources*, 154, 351–359.
- [73] A. Brouzgou, A. Podias and P. Tsiakaras, 2013. "PEMFCs and AEMFCs directly fed with ethanol: a current status comparative review" *Journal of Applied Electrochemistry*, 43, 119–136.
- [74] J.W. Magee, W.-P. Zhou and M.G. White, 2014. "Promotion of Pt surfaces for ethanol electro-oxidation by the addition of small SnO<sub>2</sub> nanoparticles: Activity and mechanism". *Applied Catalysis B: Environmental*, 152–153, 397–402.

- [75] X. Li, J. Wei, Y. Chai and S. Zhang, 2015. "Carbon nanotubes/tin oxide nanocomposite-supported Pt catalysts for methanol electro-oxidation". *Journal of Colloid and Interface Science*, 450, 74–81.





Appendix/Appendices

This material is reserved for educational use only, not allowed for commercial use.

Forbidden to modify the content, and cite the document when use.



This material is reserved for educational use only, not allowed for commercial use.

Forbidden to modify the content, and cite the document when use.

## PVP-assisted Sb-doped SnO<sub>2</sub> nanofibers synthesized by electrospinning process

Somtop Santibenchakul<sup>1,a\*</sup>, Suwan Chaiyasith<sup>1,b</sup> and Wisanu Pecharapa<sup>2,c</sup>

<sup>1</sup> Department of Chemistry, Faculty of Science, King Mongkut's Institute of Technology Ladkrabang, Bangkok 10520, Thailand

<sup>2</sup> College of Nanotechnology, King Mongkut's Institute of Technology Ladkrabang, Bangkok 10520, Thailand

<sup>a</sup>knotchem@hotmail.com, <sup>b</sup>kcsuwan@kmitl.ac.th, <sup>c</sup>kpewisan@gmail.com

**Keywords:** ATO nanofibers; Electrospinning; Polyvinylpyrrolidone (PVP)

**Abstract.** Well-defined Sb-doped tin oxide (ATO) nanofibers were synthesized by electrospinning technique. Polyvinylpyrrolidone (PVP), SnCl<sub>4</sub>·5H<sub>2</sub>O and SbCl<sub>3</sub> were chosen as suitable precursors for preparing ATO nanofibers. All of precursors were homogeneously dissolved with the mixture solvent of dimethylformamide (DMF) and absolute ethanol. Electrospinning process was carried out at applied voltage of 10 kV and distance between needle tip to aluminium foil collector was fixed at 10 cm. The injection rate of precursor solution was controlled at 0.5 ml/hr. The as-spun nanofibers were calcined at 600°C with heating rate of 5 °C/min in order to remove the PVP template and improve the crystallinity of ATO structure. Effect of Sb doping concentration on their crystal structure was investigated. The morphology and crystal structure of the electrospun fibers were analyzed by scanning electron microscope (SEM) and X-ray diffraction (XRD). In this work, the obtained ATO nanofibers had average range diameter from 150 to 350 nm with rough surface. Sb doping concentration in ATO nanofibers plays a key role on their network morphology. The excellent doping concentration of Sb that offered the continuous fibrous and porous ATO nanofibers was 7%.

### Introduction

Tin Oxide (SnO<sub>2</sub>) is one of main key functional semiconductors applied in various applications such as chemical sensor [1], lithium-ion battery [2], photocatalyst [3], solar cell [4] and gas sensor [5,6]. It is an n-type metal oxide with the high chemical stability, non-toxicity, low cost, and excellent electrical properties. However, SnO<sub>2</sub> powder itself has some drawback because of its slow response and low sensitivity. Developing materials based on SnO<sub>2</sub> with rapid response and high sensitivity is currently in focus. Increasing surface to volume ratio and doping process are the potential methods to develop and enhance their properties [7, 8]. As an effective synthesis of SnO<sub>2</sub> with high surface to volume ratio, electrospinning is a good choice to produce a large amount of SnO<sub>2</sub> nanofibers. Recently, many researchers have reported the effective dopants in SnO<sub>2</sub> nanofibers including Ag [1], P [2], Fe [5], Al [6] and alkali earth [8]. It is proven that doping strategy is an effective process to improve response and sensitivity of metal oxide nanofibers. Antimony (Sb) is a candidate element for doping into the tin oxide lattice because Sb<sup>3+</sup> has close ionic radius to Sn<sup>4+</sup>, so it could suitably substitute into Sn site in tin oxide lattice. The substitution of Sn<sup>4+</sup> by Sb<sup>5+</sup> may lead to a creation of conducting carrier-oxygen vacancies and the extra electrons generated into the conduction band [9]. Regarding this truth, ATO product should be a high conductive material that can be utilized in fabrication of novel devices in various sensing applications. However, the synthesis of Sb-doped SnO<sub>2</sub> nanofibers via electrospinning has been rarely reported. In this research, we employed the facile and easy route to synthesize Sb-doped SnO<sub>2</sub> nanofibers via electrospinning process and calcination technique. Effect of Sb concentration on crystallinity and morphology of SnO<sub>2</sub> nanofibers were investigated.

### Experimental

All chemicals used in this work were analytical grade and used without further purification. In a typical synthesis, 8% w/w of PVP solution was prepared and dissolved in the solvent mixture between *N,N*-dimethylformamide (DMF) and absolute ethanol. 2 mmol  $\text{SnCl}_4 \cdot 5\text{H}_2\text{O}$  and a certain amount of  $\text{SbCl}_3$  was dissolved in the polymer solution with designated mol content of  $\text{SbCl}_3$  of 0%, 3%, 5%, 7% and 10%, followed by strong stirring until a viscous solution was achieved. The precursor solution was subsequently loaded into a 10 mL syringe with a metal needle tip for electrospinning. The Al foil was selected as a collector and the distance between the needle tip and the collector was fixed at 10 cm. The voltage was applied at 10 kV and the injection rate of the precursor solution was controlled at 0.5 mL/hr by a syringe pump. The obtained fiber mats were afterward calcined at 600°C in air for 3 hr with the heating rate of 5 °C/min. The morphologies of the nanofibers were observed by SEM (ZEISS, EVO MA10). Chemical composition of the nanofibers was investigated by energy-dispersive X-ray Spectrophotometer (EDS, Oxford instruments X-Max<sup>N</sup>). The crystallinity of the nanofibers was characterized by XRD (Panalytical x'Pert pro MPD) using  $\text{Cu-K}\alpha$  radiation in the  $2\theta$  range of 20° to 80° with a scanning rate of 0.02° s<sup>-1</sup>.

### Results and Discussion

Fig. 1 shows the SEM images of PVP nanofibers and the as-spun  $\text{SnO}_2$  nanofibers. It is clearly observed that average diameter of PVP nanofibers is larger than the PVP +  $\text{SnCl}_4$  as-spun nanofibers. The average diameter of pure polymer nanofibers and the salt-polymer nanofibers is approximately 850 and 300 nm, respectively. The first possible mechanism taking important roles on this difference is the low conductivity and high viscosity of polymer solution. Addition of  $\text{SnCl}_4$  into the PVP solution is able to increase the conductivity of the solution. The net surface charge density of the solution jet consequently increases leading the significant decrease in the diameter of as-prepared fibers. The appearance of salt in polymer solution can additionally reduce the liquid jet viscosity resulting in the ease of fiber fabrication and the reduction in their size [10].

The difference of morphology and composition of the as-spun ATO nanofibers before and after calcination is illustrated in Fig. 2. Fig. 2A shows the image of as-spun nanofibers with smooth surface and the diameter range from 90 to 250 nm. After annealing at 600°C in air, SEM image Fig. 2B shows a  $\text{SnO}_2$  nanocrystalline fibrous network morphology whose diameters ranging from 150 to 350 nm with rough surface. The after-calcined fibers comprise many small beads of tightly bound  $\text{SnO}_2$  nanoparticles arranging in form of well-defined and nanofibers with good uniformity in their size. Figure 2C and 2D are corresponding spectra of EDX analysis of ATO nanofibers before and after calcination, respectively. The EDX Spectrum (Fig. 2D) shows that the as-spun nanofibers after calcinations is composed of Sn, O and Sb implying the existence of major elements and formation of ATO nanofibers. Fig. 3 shows SEM images of ATO nanofibers with different Sb concentrations. It can be found that ATO nanofibers display high fibrous morphology with increasing Sb-doping concentration suggesting that Sb concentration plays a key role on the modification of  $\text{SnO}_2$  fiber formation. The relevant mechanism for the formation of ATO nanofiber with incorporation of Sb dopant can be addressed. During calcination process of as-spun ATO nanomats the decomposition of PVP was occurred and provided volatile gas that could thermally diffuse to the surface of the fibers. Subsequently, the  $\text{SnO}_2$  nanoparticles would nucleated, crystallized and aggregated at the surface of fibers [6].

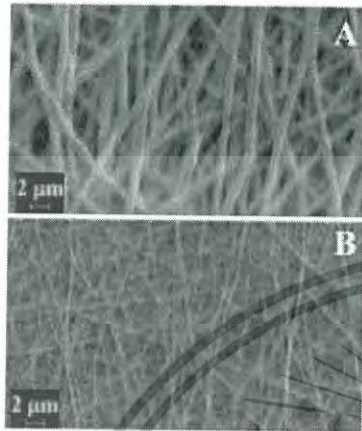


Fig. 1 SEM images of (A) PVP nanofibers and (B) as-spun  $\text{SnO}_2$  nanofibers containing PVP +  $\text{SnCl}_4 \cdot 5\text{H}_2\text{O}$ .

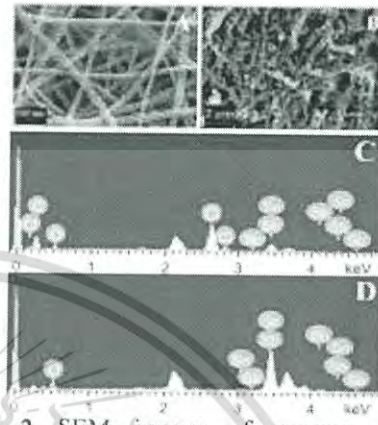


Fig. 2 SEM images of as-spun ATO nanofibers (A) before and (B) after calcination and EDX spectra of as-spun nanofibers (C) before and (D) after calcination.

In addition, doping of Sb could considerably interrupt the  $\text{SnO}_2$  crystalline growth [9] guiding to the deterioration in their particle size in the fibers. Furthermore, In case of 5% and 7% ATO as observed in Fig. 3B and 3C, high Sb content can prevent crystallization and agglomeration of  $\text{SnO}_2$  nanoparticles and part of Sn precursor may be separated and diffused to surface of fiber. The Sn precursor at surface templates was crystallized, but some of  $\text{SnO}_2$  could migrate to the core of fibers. When the Sb concentration increased to 10%, the dopant atom could cause the further reduction in particle size of  $\text{SnO}_2$  and initiate the firm adherence between tiny particles to form more fibrous morphologies as noticed in Fig. 3D. From this result, it is suggested that 7% ATO sample is optimized condition that simultaneously provide fibrous and porous morphology.

The XRD spectra of the pure  $\text{SnO}_2$  and ATO nanofibers are exhibited in Fig. 4. After calcination at  $600^\circ\text{C}$  for 3 hr, all samples possess sharp and intense diffraction peaks that are well indexed to the tetragonal structure of  $\text{SnO}_2$  in JCPDS No. 41-1445. It can be further noticed that no strange peaks of impurity or separated phase due to the incorporation of Sb dopant is observed. This feature implies successful doping of Sb into  $\text{SnO}_2$  crystalline lattice.

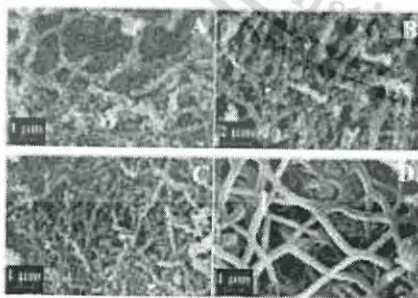


Fig. 3 SEM image of  $\text{SnO}_2$  nanofibers containing varied Sb concentration (A) 3% (B) 5% (C) 7% and (D) 10%.

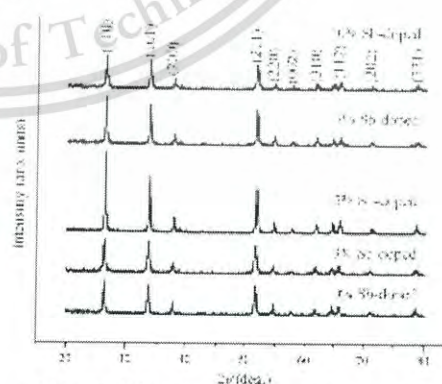


Fig. 4 XRD patterns of pure and ATO nanofibers with different Sb concentrations.

### Conclusions

Sb-doped  $\text{SnO}_2$  nanofibers have been comfortably synthesized by electrospinning technique and suitable calcination. Varying Sb concentration in doping process has the significant influence on morphologies of ATO nanofibers. The higher Sb doping concentration in ATO nanofiber has more

fibrous network morphology while it still possesses good crystalline structure. It can be concluded that the excellent network of ATO nanofibers were prepared by uncomplicated technique.

#### Acknowledgments

This work has been supported by Rajamangala University of Technology Tawan-Ok with the Ph.D. scholarship. The author would like to thank Rajamangala University of Technology Thanyaburi (RMUTT) for XRD analysis.

#### References

- [1] Y.E. Miao, S. He, Y. Zhong, Z. Yang, W.W. Tjiu, T. Liu, A novel hydrogen peroxide sensor based on Ag/SnO<sub>2</sub> composite nanotubes by electrospinning, *Electrochim. Acta* 99 (2013) 117 – 123.
- [2] X. Liu, D. Teng, T. Li, Y. Yu, X. Shao, X. Yang, Phosphorus-doped tin oxides/carbon nanofibers webs as lithium-ionbattery anodes with enhanced reversible capacity, *J. Power Sources* 272 (2014) 614 – 621.
- [3] P. Zhang, L. Wang, X. Zhang, C. Shao, J. Hu, G. Shao, SnO<sub>2</sub>-core carbon-shell composite nanotubes with enhanced photocurrent and photocatalytic performance, *Appl. Catal. B: Environ* 166–167 (2015) 193–201.
- [4] Y.F. Wang, X.F. Li, D.J. Li, Y.W. Sun, X.X. Zhang, Controllable synthesis of hierarchical SnO<sub>2</sub> microspheres for dye sensitized solar cells, *J. Power Sources* 280 (2015) 476 – 482.
- [5] Z. Wang, L. Liu, Synthesis and ethanol sensing properties of Fe-doped SnO<sub>2</sub> nanofibers, *Mater Lett* 63 (2009) 917–919.
- [6] J. Wu, Q. Huang, D. Zeng, S. Zhang, L. Yang, D. Xia, Z. Xiong, C. Xie, Al-doping induced formation of oxygen-vacancy for enhancing gas-sensing properties of SnO<sub>2</sub> NTs by electrospinning, *Sens. Actuators B* 198 (2014) 62–69.
- [7] X.L. Xu, Y. Chen, S.Y. Ma, W.Q. Li, Y.Z. Mao, S.H. Yan, T. Wang, Facile synthesis of SnO<sub>2</sub> mesoporous tubular nanostructure with high sensitivity to ethanol, *Mater Lett* 143 (2015) 55–59.
- [8] S. Xu, K. Kan, Y. Yang, C. Jiang, J. Gao, L. Jing, P. Shen, L. Li, K. Shi, Enhanced NH<sub>3</sub> gas sensing performance based on electrospun alkaline-earth metals composited SnO<sub>2</sub> nanofibers, *J. Alloys Comp* 618 (2015) 240–247.
- [9] R. Noonuruk, N. Vittayakorn, W. Mekprasart, J. Sritharathikhun, W. Pecharapa, Sb-doped SnO<sub>2</sub> nanoparticles synthesized by sonochemical-assisted precipitation process, *J. nanosci. Nanotechnol.* 15 (2015) 2564-2569.
- [10] V. Beachley, X. Wen, Effect of electrospinning parameters on the nanofiber diameter and length, *Mater. Sci. Eng., C* 29 (2009) 663–668.



This material is reserved for educational use only, not allowed for commercial use.

Forbidden to modify the content, and cite the document when use.



Copyright © 2016 American Scientific Publishers  
All rights reserved  
Printed in the United States of America

Article

Journal of  
Nanoscience and Nanotechnology  
Vol. 16, 13001–13006, 2016  
www.aspbs.com/jnn

## Sb/F-Codoped SnO<sub>2</sub> Nanofibers Synthesized by Electrospinning

Somtop Santibenchakul<sup>1,\*</sup>, Suwan Chaiyasith<sup>1</sup>, and Wisanu Pecharapa<sup>2</sup>

<sup>1</sup> Department of Chemistry, Faculty of Science, King Mongkut's Institute of Technology Ladkrabang, Bangkok 10520, Thailand

<sup>2</sup> College of Nanotechnology, King Mongkut's Institute of Technology Ladkrabang, Bangkok 10520, Thailand

In this present work, metal and non-metal doping in tin oxide nanofibers was fabricated by electrospinning technique. Sb/F co-doped SnO<sub>2</sub> nanofibers was synthesized by using polyvinylpyrrolidone as polymer precursor and SnCl<sub>4</sub> · 5H<sub>2</sub>O, SbCl<sub>5</sub>, NH<sub>4</sub>F as tin, antimony and fluorine source, respectively. The concentration of polyvinylpyrrolidone and stannic chloride dissolved with mixture solvent of Dimethylformamide and absolute Ethanol were fixed at 8 and 10%w/w and used as starting precursors. Electrospinning process was carried out at 10 kV of applied voltage by maintaining tip to collector distance of 10 cm and the feeding speed of mixed precursor was controlled at 0.5 ml/h. The as-spun nanofibers mats were calcined in air at 600 °C for 3 hours to obtain the doped-SnO<sub>2</sub> nanofibers. Thermogravimetric and X-ray diffraction results support that the optimized calcined temperature to remove polyvinylpyrrolidone template and oxidize Sn precursor is 600 °C. The morphologies of Sb/F co-doped SnO<sub>2</sub> nanofibers appear in rough surface with rearrangement of Sb/F doped SnO<sub>2</sub> porous nanobeads. The average diameter of Sb/F doped SnO<sub>2</sub> nanofibers is 422 nm with the crystallite size about 22 nm. Fourier-transform infrared and energy-dispersive X-ray spectroscopy results indicate states of transformation of starting precursors to the formation of Sb/F doped SnO<sub>2</sub> nanofibers.

**Keywords:** Sb/F Co-Doped SnO<sub>2</sub>, Nanofibers, Electrospinning.

### 1. INTRODUCTION

Among the wide band gap metal oxide semiconductors, undoped (SnO<sub>2</sub>) and doped tin oxide (SnO<sub>2</sub>) as a famous semiconductor have been fabricated as a component of technological applications in gas sensors,<sup>1,2</sup> transparent conducting electrode,<sup>3,4</sup> and solar cells.<sup>5,6</sup> Furthermore, SnO<sub>2</sub> has been extensively utilized as oxidation catalytic and photocatalytic for alcohol and phenol compounds, respectively.<sup>7,8</sup> Three major aspects of undoped SnO<sub>2</sub> properties is typically expected for practical applications. The first is high electrical conductivity with optical transparency that is a key role for optoelectronic applications. The second is catalytic activity with supported metal catalyst for catalytic materials. The final is its electrical properties with excellent sensitivity towards oxidizing and reducing gases.<sup>9</sup> Nevertheless, applications based on undoped SnO<sub>2</sub> are lack of selectivity, low of sensitivity and

low of responsibility.<sup>10</sup> Otherwise, these outstanding properties of SnO<sub>2</sub> would be worthless without high surface area.<sup>11</sup> This drawback could be solved by doping process and design method to improve surface area.<sup>12,13</sup> Among doping elements, antimony and fluorine have been recognized as crucial dopants for enhancing electrical and gas sensing properties of undoped SnO<sub>2</sub>. The doping of Sb into the SnO<sub>2</sub> could effectively decreases its resistance, leading to the increase in its conductivity and sensitivity.<sup>14,15</sup> In the case of the fluorine dopant, it might substitute an oxygen site in the SnO<sub>2</sub> lattice, leading to the improvement in its optical reflectivity.<sup>16</sup> All of above the reasons, it can be predicted that the incorporation of both dopants may heighten its properties that can meet desired functions and applications. Up to now, various methods such as sonochemical,<sup>17</sup> radio frequency magnetron sputtering,<sup>18</sup> sol-gel dip coating,<sup>19</sup> co-precipitation,<sup>20</sup> and electrospinning<sup>21</sup> have been employed to synthesize SnO<sub>2</sub>-based nanostructures. It was reported that one dimension porous SnO<sub>2</sub> nanofibers with high surface active area was

\*Author to whom correspondence should be addressed

fabricated by one-step electrospinning method accompanying calcination process.<sup>22</sup>

In this research, Electrospinning method and calcination process were jointly used to synthesize the novel antimony-fluorine co-doped tin oxide (AFTO) nanofibers. Undoped tin oxide (SnO<sub>2</sub>), antimony doped tin oxide (ATO) and fluorine doped tin oxide (FTO) were also synthesized for comparison purpose. Effect of calcination temperature and antimony concentration on crystallinity and morphology of undoped SnO<sub>2</sub> and AFTO nanofibers were investigated. The obtained nanofibers were characterized by means of thermogravimetric analysis (TGA), Fourier transform infrared spectrometer (FTIR), X-ray diffractometer (XRD), scanning electron microscope (SEM) and energy-dispersive X-ray Spectrophotometer (EDX).

## 2. EXPERIMENTAL DETAILS

Stannic chloride pentahydrate (SnCl<sub>4</sub> · 5H<sub>2</sub>O), antimony chloride (SbCl<sub>3</sub>) and ammonium fluoride (NH<sub>4</sub>F) were used as starting precursors for Sn, Sb and F, respectively. Electrospinning precursor was prepared by weighing Polyvinylpyrrolidone (PVP,  $M_w = 1,300,000 \text{ g} \cdot \text{mol}^{-1}$ ) 1.6 g and soluted in solvent mixture of absolute ethanol and *N,N*-dimethylformamide (DMF) in ratio 1:1 by weight. Afterward (5.7- $x$ - $y$ ) mmol of SnCl<sub>4</sub> · 5H<sub>2</sub>O,  $x = (0-10\% \text{ mol of SbCl}_3 \times 5.7)/100$  and  $y = (5\% \text{ mol of NH}_4\text{F} \times 5.7)/100$  was added into polymer solution followed by magnetic stirring until homogeneous solution was achieved. In this work, the concentration of fluorine doping was set at 5% mol and the concentration of antimony was varied from 0 to 10% mol. The precursor solution was consecutively electrospun from the metal needle tip with an electrostatic voltage of 10 kV while the speed of precursor solution was designated at 0.5 ml · h<sup>-1</sup> and the distance between the needle and the aluminium foil collector was kept at 10 cm. The fibrous mats of electrospun precursor were collected on a Al collector and calcined at 600 °C for 3 h with a heating rate of 0.5 °C/min. Effect of calcined temperature of undoped SnO<sub>2</sub> was studied in range 450–600 °C. SEM (ZEISS, EVO MA10) was used to observe the morphologies and chemical composition was investigated by energy-dispersive X-ray Spectrophotometer (EDS, Oxford instruments X-Max<sup>8</sup>). The thermogravimetric analyses of the polymer template and SnO<sub>2</sub> were carried out by pyris 1 TGA (Perkin). The crystal structure analysis was characterized by XRD (Panalytical x'Pert pro MPD) using Cu-K<sub>α</sub> radiation in the 2θ range of 20° to 80° with a scanning rate of 0.02° s<sup>-1</sup>. Fourier-transform infrared (FTIR) spectra of the product were obtained on the NICOLET 6700 (Thermo scientific) with the scanning range of 400–4000 cm<sup>-1</sup> and the resolution of 1 cm<sup>-1</sup>.

## 3. RESULTS AND DISCUSSION

The XRD patterns of the undoped SnO<sub>2</sub> nanofibers calcined at different temperatures were shown in Figure 1.

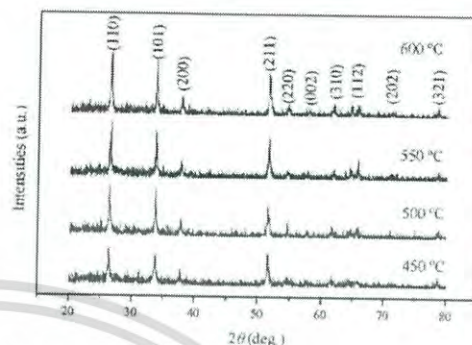


Figure 1. XRD patterns of the undoped SnO<sub>2</sub> nanofibers calcined at various temperatures.

The X-ray diffraction peak positions nicely fit with the values of rutile SnO<sub>2</sub> phases (JCPDS 41-1445). The crystallization of SnO<sub>2</sub> has initiated at 450 °C accompanying broad diffraction peak. At elevated temperatures the diffraction peaks of SnO<sub>2</sub> became much sharper and more intense suggesting that the crystal growth of SnO<sub>2</sub> was continued with an increasing calcination temperature.<sup>23</sup> Figure 2 illustrates SEM images of undoped SnO<sub>2</sub> with calcination at 450 °C to 600 °C. All of them show good arrangement of long continuous chain of SnO<sub>2</sub> nanobeads. The SEM micrograph of SnO<sub>2</sub> calcined at 450 °C demonstrates more intensive and some part of fibers has the cumulative of SnO<sub>2</sub> nanobeads. When the calcination temperature was increased from 500 °C to 550 °C, the crystalline growth and rearrangement of SnO<sub>2</sub> nanobeads and formation of fibers begun. Eventually, the long chain of porous SnO<sub>2</sub> nanofibers structure was obtained as shown in SEM image of the undoped SnO<sub>2</sub> nanofibers calcined at 600 °C.

The thermal behaviors of as-spun SnO<sub>2</sub> and pure PVP nanofibers were performed using TGA and corresponding results are exhibited in Figure 3. The TGA curves

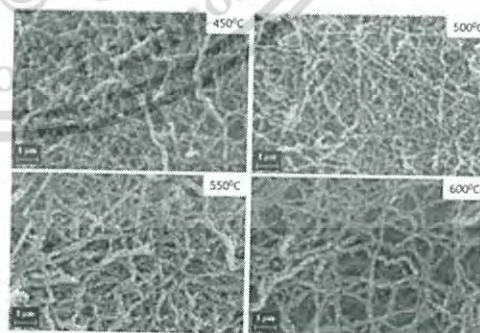


Figure 2. SEM images of the undoped SnO<sub>2</sub> nanofibers calcined at various temperatures.

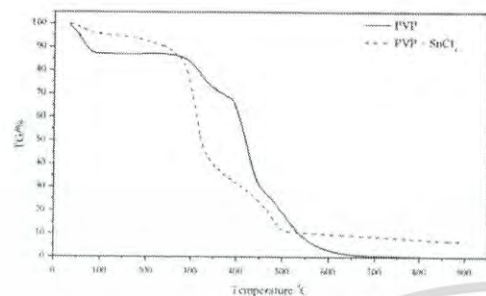


Figure 3. TGA graph of thermal decomposition of electrospun PVP/SnO<sub>2</sub> composite and PVP nanofibers.

of as-spun SnO<sub>2</sub> nanofibers show three steps weight loss with increasing temperature. The first weight loss of about 5% may be due to the evaporation of solvent mixture in the SnCl<sub>4</sub>-PVP nanofibers. The 63% weight of the as-spun nanofibers was burnt out in the second step because of decomposition of PVP. The third step of about 25% weight loss was the complete decomposition and oxidation of Sn precursor resulting the formation of SnO<sub>2</sub> nanofibers.<sup>22</sup> The possible mechanism for the formation of SnO<sub>2</sub> is proposed following Eqs. (1) and (2). Sn precursor can react with absolute ethanol solvent to form tin alkoxide and consequently transforms to SnO<sub>2</sub>-based compounds after calcined at 600 °C in air.



The TGA curves of pure PVP shows that the complete disintegration of PVP occurs in the vicinity of 600 °C. These results of the XRD, SEM and thermal analyses suggest that SnO<sub>2</sub> nanofibers in form of distinguished long chain of SnO<sub>2</sub> nanobeads can be obtained by the assistance of calcination at certain temperature.

The XRD patterns of undoped SnO<sub>2</sub>, Sb-doped SnO<sub>2</sub>, F-doped SnO<sub>2</sub> and Sb/F doped SnO<sub>2</sub> nanofibers are displayed in Figure 4. All samples possess the single polycrystalline of tetragonal structure with major crystal lattice planes of (110), (101) and (211)<sup>24</sup> without noticeable impurities. It could be advised that Sb ion and F ion were suitably incorporated into the SnO<sub>2</sub> lattice in ATO, FTO and AFTO products. The substitution of Sb<sup>3+</sup> and F<sup>-</sup> ions at Sn<sup>4+</sup> and O<sup>2-</sup> sites in the SnO<sub>2</sub> lattice, respectively could enable the generation of extra electrons to the conduction band, resulting in the increase of conductivity of SnO<sub>2</sub>.<sup>20-25</sup> Table I demonstrates the crystallite sizes of the products determined by full width at half maximum (FWHM) of diffraction peak (110) using a well-known Scherrer's equation. It is found that the values of the undoped SnO<sub>2</sub>, ATO, FTO and AFTO nanofibers are 24.22, 28.64, 24.13 and 19.82 nm, respectively.

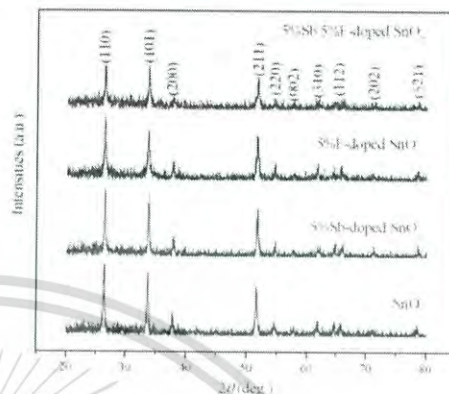


Figure 4. XRD patterns of the undoped SnO<sub>2</sub>, ATO, FTO and AFTO nanofibers calcined at 600 °C.

The crystallite size of the ATO is bigger than the undoped SnO<sub>2</sub>. This feature could be originated from the fact that the ionic radiuses of Sb<sup>3+</sup> ( $r = 0.76 \text{ \AA}$ ) is larger than Sn<sup>4+</sup> ( $r = 0.69 \text{ \AA}$ ) that would obstruct the crystallization of SnO<sub>2</sub>.<sup>17</sup> As a result, some of Sn<sup>4+</sup> could diffuse and agglomerate to form the fiber wall and generate the larger crystallite size of SnO<sub>2</sub>. On the other hand, the ionic radius of fluorine ion (1.33 Å) was very close to oxygen ion (1.32 Å). The substitution of O<sup>2-</sup> with F<sup>-</sup> is therefore insignificant to make the variation of crystallite size of SnO<sub>2</sub>. The possible reason for the significant reduction in crystallite size of AFTO may originate from the synergistic of Sb<sup>3+</sup>-F<sup>-</sup> co-doped into SnO<sub>2</sub> lattice guiding to intercept the coagulation of Sn precursor and accelerate the formation of SnO<sub>2</sub> particles.

The FTIR measurements were carried out and relevant results are depicted in Figure 5, confirming the good formation of undoped and doped SnO<sub>2</sub>. The absorption peaks at 1641 cm<sup>-1</sup>, 1453 cm<sup>-1</sup> and 1286 cm<sup>-1</sup> of as-synthesized SnO<sub>2</sub> sample can be ascribed to the C=O stretching, CH<sub>2</sub> scissor and C-N stretching of PVP molecule that is a template for fiber formation during electrospinning process.<sup>26</sup> However, for the sample obtained after calcination at 600 °C, Sn-O stretching of SnO<sub>2</sub> bands in range of 600–450 cm<sup>-1</sup> were only found with disappearance of PVP bands. This feature strongly ascertains the simultaneous complete decomposition of PVP and formation of

Table I. Crystallite size of the undoped SnO<sub>2</sub>, ATO, FTO and AFTO calcined at 600 °C.

Materials	Crystallite size (nm)
SnO <sub>2</sub>	24.22
ATO	28.64
FTO	24.13
AFTO	19.82

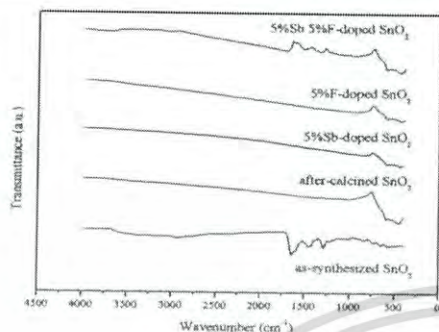


Figure 5. FTIR spectra of an as-synthesized and after-calcined SnO<sub>2</sub>, ATO, FTO and AFTO nanofibers.

SnO<sub>2</sub>, ATO, FTO and AFTO nanofibers after calcination beyond certain temperature of 600 °C.<sup>24</sup>

Effect of Sb concentration in co-doped SnO<sub>2</sub> nanofibers was investigated. The XRD patterns of AFTO nanofibers with different Sb concentration are shown in Figure 6. It is observed that no impurity diffraction peak is detected in AFTO samples. It can be guided that the primary of co-doping Sb/F into SnO<sub>2</sub> were accomplished by electrospinning technique and calcination process. The intensities of AFTO diffraction peaks reduce when compared with the FTO diffraction peaks (0%Sb 5%F doped SnO<sub>2</sub>). Meanwhile, the intensities of diffraction peaks of AFTO exhibits significant increment with increasing Sb concentration. Effect of Sb concentration on crystallite size of AFTO nanofiber is shown in Table II. It is noticed that the crystallite sizes of AFTO are 24.13, 18.51, 19.82, and 22.61 nm for the samples with 0, 3, 5 and 10% mol of Sb doping content, respectively. Sb<sup>3+</sup> ion can prevent the crystallization of SnO<sub>2</sub> because the larger ionic radius of doping ion. As a result, part of Sn<sup>4+</sup> precursors are collected at the surface of the fibers more than condensed at

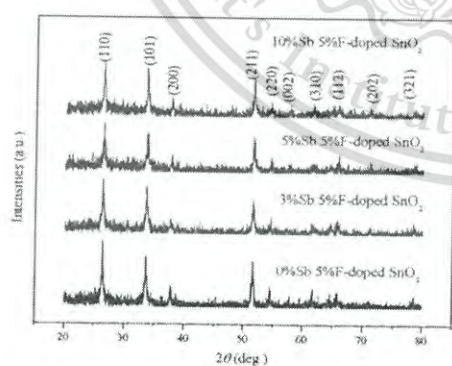


Figure 6. XRD patterns of the AFTO nanofibers with varied Sb concentration calcined at 600 °C

Table II. Crystallite size of the AFTO with varied %Sb in co-doped SnO<sub>2</sub> calcined at 600 °C.

%Sb in co-doped SnO <sub>2</sub> (fix 5%F)	Crystallite size (nm)
0	24.13
3	18.51
5	19.82
10	22.61

the center. After calcination in the air, the crystallization of AFTO nanoparticles was obtained and composed in porous fiber form. Therefore, the crystal growth of co-doped SnO<sub>2</sub> increased when the amount of doping was increased.

SEM images in Figure 7 reveal the morphologies of AFTO samples with different Sb doping concentrations. SEM image of FTO nanofibers (0%Sb) indicates ill-defined fibrous structures with poor uniformity in shape and size due to NH<sub>4</sub><sup>+</sup> from F-precursor that may cause the modification of precursor during electrospinning process. The morphology of 3%Sb in AFTO shows more vigorous and well-defined fibrous structure than FTO nanofibers. It consists of clusters of small nanoparticles adhering to the fibers. SEM image of 5%Sb AFTO exhibits porous fibers with the crowd of AFTO nanobeads while SEM image of 10%Sb AFTO displays only the porous AFTO fibers. Moreover, it is observed that the diameter of AFTO nanofiber increases as same as the AFTO crystallite size as shown in Table II.

The existence of relevant elements in the as-synthesized (left) and after calcined (right) of the undoped SnO<sub>2</sub> and AFTO nanofibers were confirmed by EDX spectra as exhibited in Figure 8. From the EDX results of undoped SnO<sub>2</sub>, the Sn, Cl, C and O were observed in as-synthesized sample while only Sn and O elements were monitored in after-calcined sample, suggesting the complete decomposition of PVP template and formation of SnO<sub>2</sub> nanofibers. The appearance of C in EDX spectra may originate from the supporting carbon tape during measurement. For AFTO samples, the absence of Cl signal

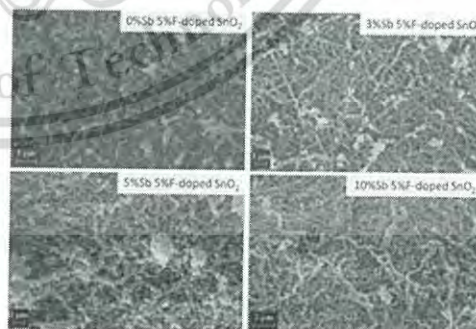


Figure 7. SEM images of the AFTO nanofibers with varied Sb concentration calcined at 600 °C.

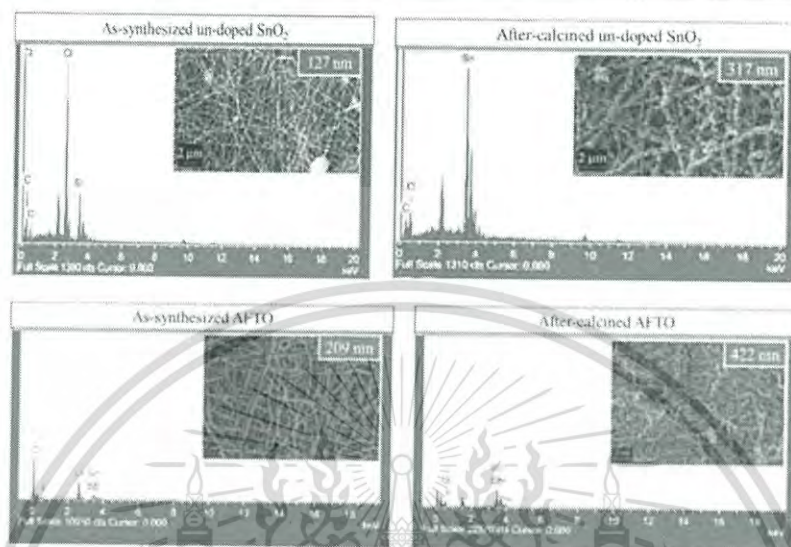


Figure 8. EDX spectra and SEM images (inset) of as-synthesized (left) and after calcined (right) of undoped SnO<sub>2</sub> and AFTO nanofibers.

in after-calcined samples compared with as-synthesized sample was noticed, implying the successful doping and formation of AFTO nanofibers. SEM images of the as-synthesized and after calcined undoped SnO<sub>2</sub> and AFTO nanofibers were shown as insets in Figure 8. The as-synthesized fibers had smooth surface while after calcined samples appeared in rough surface. The average diameter of the as-synthesized undoped SnO<sub>2</sub> and AFTO nanofibers are 127 and 209 nm while the average diameter of the obtained fibers after calcined at 600 °C are 317 and 422 nm, respectively. The possible formation of SnO<sub>2</sub> fibers can be explained that the PVP template was burnt out with gave the diffusion of Sn precursors to surface area of the fibers. As a result, the oxidation of metal oxide was occurred giving the porosity and rough surface metal oxide fibers after calcination.<sup>22</sup>

#### 4. CONCLUSION

The novel Sb/F doped SnO<sub>2</sub> nanofibers were successfully synthesized by a facile electrospinning method via single solvent system of PVP/Sn, Sb, F precursors. The polymer template was burnt out while Sn precursor was oxidized by calcination process. All of characterization results advice that tin-based precursors were completely transformed into SnO<sub>2</sub> when calcined at 600 °C for 3 hours. The morphology of the fibers was found to be dense with uniform contribution of nanobeads in form of porous fibrous structure. The results demonstrate that the doping of Sb and F into the SnO<sub>2</sub> crystalline phase was succeeded. This material will be extendable to fabricate for

specific potential applications in electrochemical and gas sensor.

**Acknowledgments:** This work has been supported by Rajamangala University of Technology Tawan-Ok through the Ph.D. scholarship. This work has partially been supported by the National Nanotechnology Center (NANOTEC), NSTDA, Ministry of Science and Technology, Thailand, through its program of Center of Excellence Network and King Mongkut's Institute of Technology Ladkrabang (KMUTL) Research Fund. The author would like to thank Rajamangala University of Technology Thanyaburi (RMUTT) for XRD analysis.

#### References and Notes

1. S. E. Moon, H. K. Lee, N. J. Choi, J. Lee, W. S. Yang, J. Kim, J. J. Jong, and D. J. Yoo, *J. Nanosci. Nanotechnol.* 12, 5543 (2012).
2. W. Chen, Q. Li, L. Xu, and W. Zeng, *J. Nanosci. Nanotechnol.* 15, 1245 (2015).
3. S. J. Hong, Y. H. Kim, S. J. Cha, and Y. S. Kim, *J. Nanosci. Nanotechnol.* 15, 7997 (2015).
4. J. Lim, B. Y. Jeong, H. G. Yoon, S. N. Lee, and J. Kim, *J. Nanosci. Nanotechnol.* 12, 1675 (2012).
5. Y. F. Wang, X. F. Li, D. J. Li, Y. W. Sun, and X. X. Zhang, *J. Power Sources* 280, 476 (2015).
6. J. W. Bae, B. R. Koo, H. R. An, and H. J. Ahn, *Ceram. Int.* 41, 14668 (2015).
7. X. Li, J. Wei, Y. Chai, and S. Zhang, *J. Colloid Inert. Sci.* 450, 74 (2015).
8. A. M. Al-Handi, M. Sillanpää, and J. Dutta, *J. Alloys Compd.* 618, 366 (2015).
9. M. Batrill and U. Diebold, *Prog. Surf. Sci.* 79, 47 (2005).
10. L. Liu, T. Zhang, L. Wang, and S. Li, *Mater. Lett.* 63, 2041 (2009).
11. S. Sago, A. B. Suryamas, G. M. Anilkumar, T. Ogi, and K. Okuyama, *Mater. Lett.* 105, 202 (2013).

12. C. M. Ghimbeu, M. Lumbreras, M. Siadat, R. C. van Landschoot, and J. Schoonman, *Sens. Actuators, B* 133, 694 (2008).
13. X. L. Xu, Y. Chen, S. Y. Ma, W. Q. Li, Y. Z. Mao, S. H. Yan, and T. Wang, *Mater. Lett.* 143, 55 (2015).
14. R. R. Kumar, K. N. Rao, K. Rajanna, and A. R. Phani, *Mater. Lett.* 106, 164 (2013).
15. J. Ma, Y. Liu, H. Zhang, P. Ai, N. Gong, Y. Wu, and D. Yu, *Sens. Actuators B Chem.* 216, 72 (2015).
16. B. Zhang, Y. Tian, J. X. Zhang, and W. Cai, *Mater. Lett.* 64, 2707 (2010).
17. R. Noonuruk, N. Vittayakorn, W. Mekprasart, J. Sriharathikhun, and W. Pecharapa, *J. Nanosci. Nanotechnol.* 15, 2564 (2015).
18. J. Saadeddin, B. Pecquenard, J. P. Manaud, R. Decourt, C. Labrègue, T. Buffeteau, and G. Campet, *Appl. Surf. Sci.* 253, 5240 (2007).
19. Q. P. Tran, J. S. Fang, and T. S. Chin, *Mater. Sci. Semicond. Process.* 40, 664 (2015).
20. Y. Li, J. Wang, B. Feng, K. Duan, and J. Weng, *J. Alloys Compd.* 634, 37 (2015).
21. S. Xu, K. Kan, Y. Yang, C. Jiang, J. Gao, J. Jing, P. Shen, L. Li, and K. Shi, *J. Alloys Compd.* 618, 240 (2015).
22. X. Xia, X. J. Dong, Q. F. Wei, Y. B. Cai, and K. Y. Lu, *Express Polym. Lett.* 6, 169 (2012).
23. H. H. Son and W. G. Lee, *J. Ind. Eng. Chem.* 18, 317 (2012).
24. N. Dharmaraj, C. H. Kim, K. W. Kim, H. Y. Kim, E. K. Suh, and K. Y. Lu, *Spectrochim. Acta, Part A* 64, 136 (2006).
25. E. Elangovan and K. Ramamurthiand, *Appl. Surf. Sci.* 249, 183 (2005).
26. A. M. Abdelghany, M. S. Mekhail, E. M. Abdelrazek, and M. M. Aboud, *J. Alloys Compd.* 646, 326 (2015).

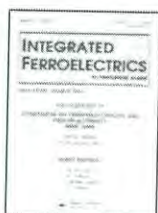
Received: 21 January 2016. Accepted: 29 June 16.



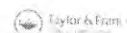


This material is reserved for educational use only, not allowed for commercial use.

Forbidden to modify the content, and cite the document when use.



**Integrated Ferroelectrics**  
An International Journal



ISSN: 1058-4587 (Print) 1607-8489 (Online) Journal homepage: <http://www.tandfonline.com/loi/ginf20>



## Effect of PVP concentration on microstructure and physical properties of electrospun SnO<sub>2</sub> nanofibers

S. Santibenchakul, S. Chaiyasith & W. Pecharapa



To cite this article: S. Santibenchakul, S. Chaiyasith & W. Pecharapa (2016) Effect of PVP concentration on microstructure and physical properties of electrospun SnO<sub>2</sub> nanofibers, *Integrated Ferroelectrics*, 175:1, 130-137, DOI: 10.1080/10584587.2016.1203222

To link to this article: <http://dx.doi.org/10.1080/10584587.2016.1203222>

 Published online: 12 Aug 2016.

 [Submit your article to this journal](#) 

 [View related articles](#) 

 [View Crossmark data](#) 



Full Terms & Conditions of access and use can be found at  
<http://www.tandfonline.com/action/journalInformation?journalCode=ginf20>

Download by: [King Mongkut's Inst of Technology Ladkrabang], [Wisanu Pecharapa]

Date: 13 August 2016, At: 21:51

## Effect of PVP concentration on microstructure and physical properties of electrospun SnO<sub>2</sub> nanofibers

S. Santibenchakul<sup>a</sup>, S. Chaiyasith<sup>a</sup>, and W. Pecharapa<sup>b</sup>

<sup>a</sup>Department of Chemistry, Faculty of Science, King Mongkut's Institute of Technology Ladkrabang, Bangkok, Thailand; <sup>b</sup>College of Nanotechnology, King Mongkut's Institute of Technology Ladkrabang, Bangkok, Thailand

### ABSTRACT

The various exceptional crystalline morphologies of tin oxide (SnO<sub>2</sub>) nanofibers were fabricated using conventional electrospinning and calcination process. Polyvinylpyrrolidone (PVP) was used as polymer template and tin (IV) chloride (SnCl<sub>4</sub>·5H<sub>2</sub>O) was chosen as starting material for electrospun SnO<sub>2</sub> nanofibers. The concentration of PVP was varied from 6%w/w to 12%w/w while the concentration of SnCl<sub>4</sub>·5H<sub>2</sub>O was kept constantly. The diameter of the as-spun SnO<sub>2</sub> nanofiber was ranging from 154 to 464 nm. After calcination at 600°C for 3 h, the crystal structure can be identified to the tetragonal structure of SnO<sub>2</sub> with various morphologies. The EDX analysis confirmed the existence of major elements and formation of SnO<sub>2</sub> from starting precursor. SEM results revealed that low PVP concentration led to the formation of porous SnO<sub>2</sub> nanofibers comprising long chain of SnO<sub>2</sub> nanobeads. When the PVP concentration was reached to 12%w/w, the arrangement of crystalline of SnO<sub>2</sub> became the cluster of SnO<sub>2</sub> plates.

### ARTICLE HISTORY


Received 28 November 2015  
Accepted 28 March 2016

### KEYWORDS

Polyvinylpyrrolidone (PVP);  
tin oxide (SnO<sub>2</sub>);  
electrospinning

### 1. Introduction

Due to exceptional physical, optical and electrical properties, low dimensional tin oxide (SnO<sub>2</sub>) nanostructure has recently been well-recognized as potential material for diversely practical applications including gas sensing application [1–2], anodes for lithium-ion batteries [3] and photocatalyst for dye solution degradation [4]. SnO<sub>2</sub> has been synthesized or fabricated in various low dimensional structures such as nanorods [5–6], nanowires [7–8], nanotubes [9–10] and nanoparticles [11–12]. It is realized that nanofibers in form of one-dimensional structure can provide relatively high surface area to volume ratio accompanying small pore size. One efficient method to fabricate well-defined one-dimensional metal oxide nanostructure is an electrospinning technique. In conventional electrospinning process, the charge of precursor solution jet is induced by electric field. When the electric field is increased, the surface of solution at the tip forms the Taylor cone. It is ejected from a needle tip

CONTACT W. Pecharapa  [kpewisan@gmail.com](mailto:kpewisan@gmail.com)

© 2016 Taylor & Francis Group, LLC

This material is reserved for educational use only, not allowed for commercial use.

Forbidden to modify the content, and cite the document when use.

toward to the opposite charged collector in the air while the solvent was rapidly evaporated. Thus, the continuous fibers can be collected on the metal screen [13–14]. The structure and the morphology of as-spun polymer-salt nanofibers are highly dependent on process parameters of electrospinning such as solution properties, applied voltage, speed rate of solution jet and the distance between the needle tip and the collector. It has been acknowledged that the solution properties play crucial role on the transformation of inorganic-organic solution into as-spun nanofibers [15–16]. In typical, the mixing solution of polymer and inorganic precursor has to be considered to optimize the viscosity of solution jet [17]. However, there are few recent reports focusing on the effect of polymer concentration on the morphology and the structure of the electrospun  $\text{SnO}_2$  nanofibers.

In this work, The  $\text{SnO}_2$  well-defined structures were synthesized by electrospinning technique and calcination method. The as-spun nanofibers were calcined in the air at specific temperature to decompose the polymer and crystallize the metal oxide. Effect of PVP concentration on their morphologies was investigated.

## 2. Experimental details

Tin (IV) chloride pentahydrate ( $\text{SnCl}_4 \cdot 5\text{H}_2\text{O}$ ) and polyvinylpyrrolidone (PVP) was used as the starting precursor and the polymer template, respectively. The solution for spinning process was prepared by mixing  $\text{SnCl}_4 \cdot 5\text{H}_2\text{O}$  and PVP in the solvent mixture of absolute ethanol and N,N-dimethylformamide (DMF) in weight ratio 1:1. The concentrations of PVP in the polymer/inorganic solutions were varied from 6 to 12%wt.  $\text{SnCl}_4 \cdot 5\text{H}_2\text{O}$  was set at 10%wt and dissolved in polymer solution. The mixed solution was stirred until the homogeneity of solution was reached. This precursor was subsequently loaded into a syringe with a metal needle tip for the fabrication of the fibers. The electrospinning parameters were set up as follows; the applied voltage was kept at 10 kV, the distance between the needle tip and the Al foil collector was fixed at 10 cm and the feeding rate of the precursor solution was designated at 0.5 mL/h. The obtained as-spun  $\text{SnO}_2$  fiber mats were calcined at  $600^\circ\text{C}$  in air for 3 h with the heating rate of  $5^\circ\text{C}/\text{min}$ . The morphology and the crystallinity of the  $\text{SnO}_2$  nanofibers was characterized by scanning electron microscope (ZEISS, EVO MA10) and X-ray diffraction (Panalytical x' Pert pro MPD) using  $\text{Cu-K}_\alpha$  radiation in the  $2\theta$  range of  $20^\circ$  to  $80^\circ$  with a scanning rate of  $0.02^\circ \text{ s}^{-1}$ , respectively. Chemical composition of the nanofibers was investigated by energy-dispersive X-ray Spectrophotometer (EDS, Oxford instruments X-Max<sup>N</sup>).

## 3. Results and discussion

Figure 1 shows the SEM images of morphology (left) and the distribution of diameter (right) of as-spun fibers prepared from the polymer-inorganic solution with different concentrations of PVP. It can be seen that the fiber diameter noticeably increased as the concentration of PVP was elevated from 6 to 12%wt. Moreover,

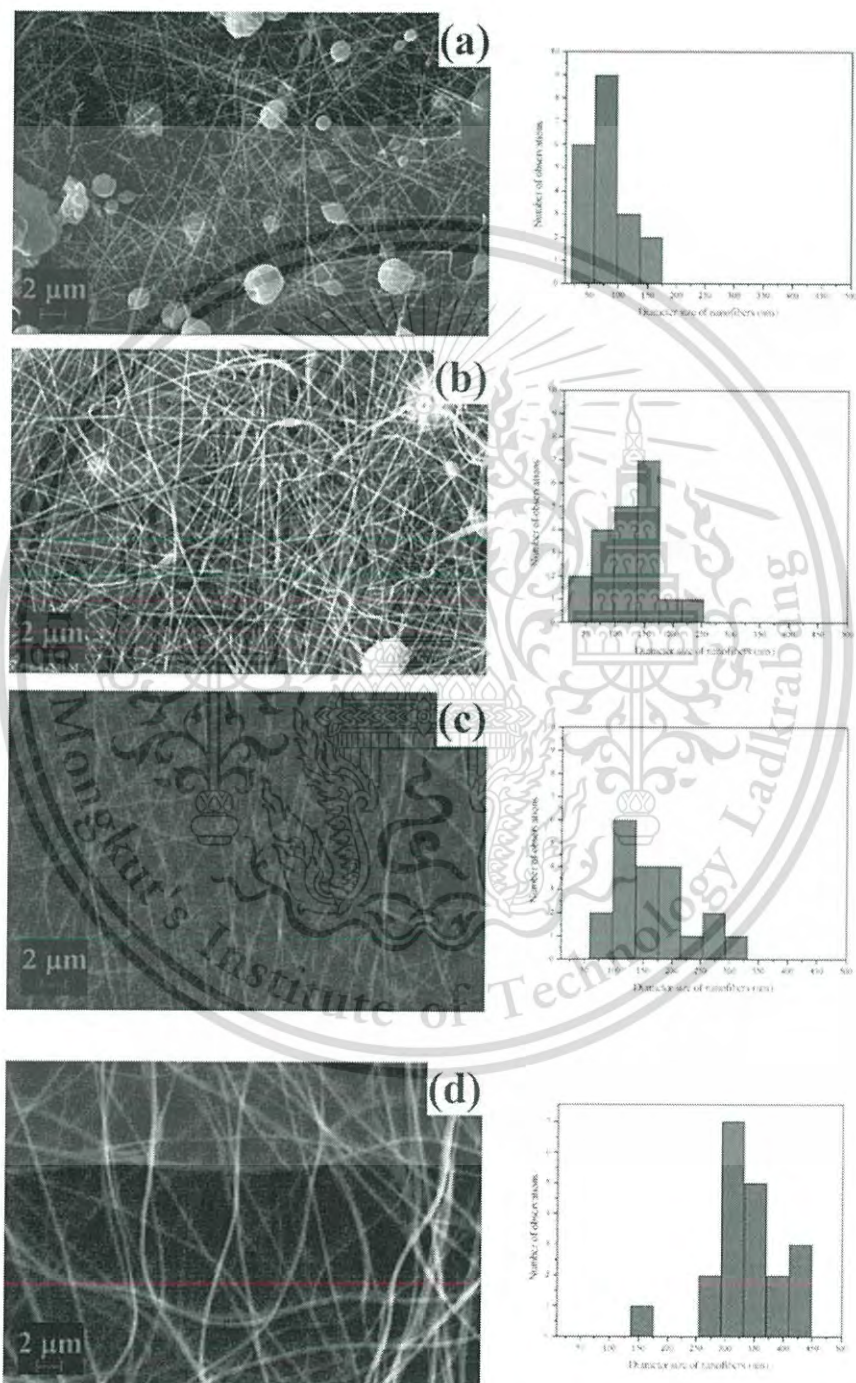
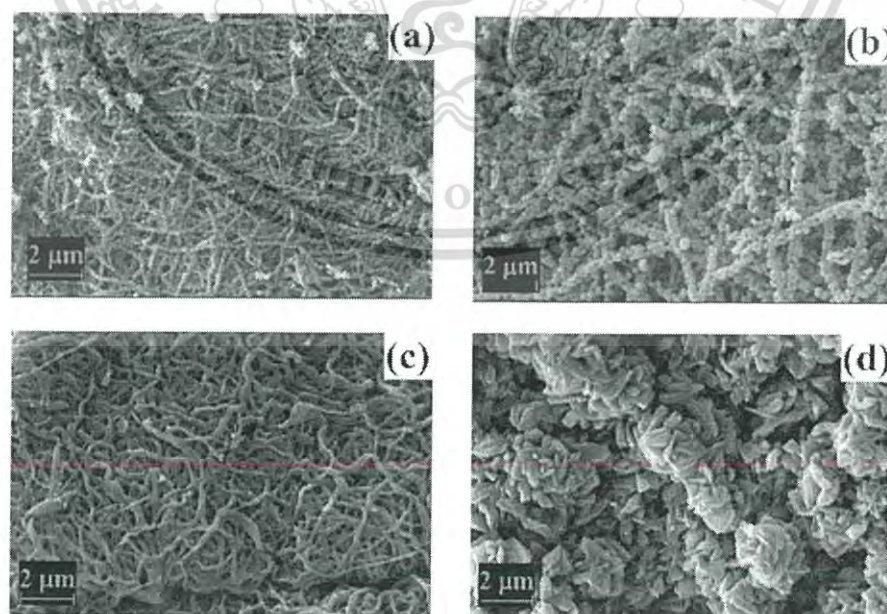


Figure 1. SEM images and the distribution of diameter of the as-spun  $\text{SnO}_2$  fibers prepared from precursors with the different PVP concentrations; (a) 6% (b) 8% (c) 10% and (d) 12%wt.

the less bead fibers were observed in the sample prepared with higher concentration of PVP. Four critical concentrations of polymer solution can be explained for this result. At the lowest concentration, the solution was in low viscosity and high surface tension which was improper to form the dynamic polymer jet for electrospinning that can result in the mixture phase of beads and fibers in the mats. However, at higher polymer concentration, the helix shape of fiber would be obtained. It is suggested that the formation of nanofibers strongly depends on the polymer concentration [18]. From this work, it is advised that PVP concentration lower than 8%wt is insufficient to obtain well-defined continuous fibers with smooth surface. The average diameter of electrospun fibers as seen in SEM images 1(a) and 1(b) are approximately 80 and 127 nm, respectively. Meanwhile, the average diameter of as-spun fibers prepared from the precursor with high PVP concentration of 10%wt and 12%wt as observed SEM images 1(c) and 1(d) are about 167 and 335 nm, respectively. At this stage, it is suggested that the variation in morphology, continuity and size of as-spun fibers is directly dependent on the viscosity of the precursor due to the loading content of the polymer acting as a template for SnO<sub>2</sub> fibers.

Figure 2 shows the SEM images of the SnO<sub>2</sub> nanostructures prepared from precursor with different PVP concentrations and calcined at 600°C for 3 h. Typically, electrospinning process is used for fabrication of nanofibers and calcinations process was used for oxidization of Sn precursor. During electrospinning process, the rapid evaporation of absolute ethanol at the edge of the fiber and phase separation is occurred. This happening can initiate the transformation of Sn precursor to tin alkoxide and induce the precipitation of this intermediate product inside the fibers



**Figure 2.** SEM images of after-calcined SnO<sub>2</sub> nanostructures prepared from precursors with the different PVP concentrations; (a) 6% (b) 8% (c) 10% and (d) 12%wt.

rather than the edge of the fibers and consequently form a solid-liquid interface in the fibers. During calcination process, the inner solvent is evaporated and PVP is gradually decomposed. As a result, it could provide volatile gas that may thermally diffuse to the outer surface of the fibers. The inner Sn precursor and PVP are thermally driven to the edge leading to the complete transformation of all liquid phase to solid phase and probable formation of hollow fibers. At this stage, PVP would be completely decomposed and tin alkoxide could be oxidized into SnO<sub>2</sub> nanograins. Further calcination can result to the grain growth of SnO<sub>2</sub> nanograins and agglomeration into big particles. However, it was reported that the decomposition of PVP played a key role in the formation of SnO<sub>2</sub> nanofibers [19–22]. Fig. 2(a) and 2(b) show corresponding SEM images of after-calcined SnO<sub>2</sub> nanofibers prepared with 6%wt- and 6%wt-PVP precursors, respectively. These images disclose that the samples are composed of SnO<sub>2</sub> nanograins of approximately 109 and 224 nm in diameter that well align in form of long nanofibers whose average diameters are in vicinity of 132 and 317 nm, respectively. These SEM images exhibit the tight adherence of many coordinate of uniform SnO<sub>2</sub> nanobeads to form SnO<sub>2</sub> nanofibers. The size of SnO<sub>2</sub> nanobeads tends to decrease with decreasing PVP content due to the ease of PVP decomposition at lower concentration while the growing and agglomeration of SnO<sub>2</sub> nanograins in liquid phase is incomplete. As a result, the small SnO<sub>2</sub> nanobeads was occurred and forced to move the edge of fibers. At higher PVP content, greater thermal energies is required to accomplish the decomposition of PVP. At this period, SnO<sub>2</sub> nanograins would have sufficient time to form the bigger SnO<sub>2</sub> nanobeads and lead to the rearrangement of SnO<sub>2</sub> nanobeads. When the concentration of PVP was raised to 10%wt, the strange morphology of SnO<sub>2</sub> was noticed. Its morphology abruptly changed to the continuous flat-sheet-like SnO<sub>2</sub> nanofibers. For this case, tin alkoxide may be accumulated in liquid phase rather than solid phase. When the calcination process began, PVP was decomposed and some tin alkoxide in solid phase was oxidized and transformed to the solid phase. In the same time, PVP inside fibers was sluggishly burnt out and Sn precursor was simultaneously agglomerated and oxidized to SnO<sub>2</sub> because it preferred to dissolve with absolute ethanol but PVP [23]. Thus, the flat sheets of SnO<sub>2</sub> nanofibers could be formed. As observed in Fig. 2(d), further increase in PVP loading composition upto 12%wt results in the formation of cluster of flake-like SnO<sub>2</sub> structure. It is implied that the continuous straight of as-spun SnO<sub>2</sub> nanofibers were catastrophically destroyed after calcinations in the air. The cause of this phenomenon may originate from this mechanism. The higher PVP concentration in the solution beyond certain content may guide to the thick layer of solid phase in as-spun fibers. Thus, most of Sn precursor was aggregated inside the fiber at which it was unable to react with oxygen in the air until the PVP was burnt out [20]. This feature consequently retarded the oxidation of Sn precursors and induced the formation of flake-like structure of SnO<sub>2</sub>.

EDS analyses of as-spun and after-calcined samples were performed to prove the composition of relevant elements of the fibers. The EDS spectrum (Fig. 3a) of the as-spun SnO<sub>2</sub> nanofibers possesses intense peaks of Sn, Cl, C and O displaying the composition in as-spun nanofibers. The signals of element come from the

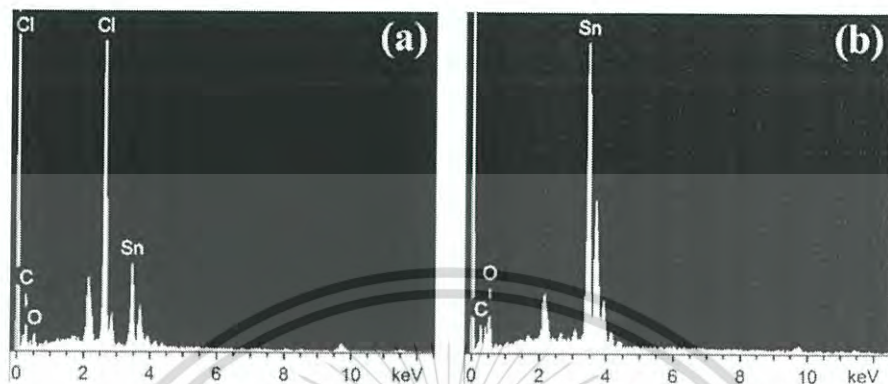


Figure 3. EDS spectra of as-spun  $\text{SnO}_2$  nanofibers (a) before and (b) after calcination.

preparation solution between  $\text{SnCl}_4 \cdot 5\text{H}_2\text{O}$  and PVP. The EDS spectrum of the calcined  $\text{SnO}_2$  fiber was shown in Fig 3b. The peak can be assigned to Sn and O element only. The C signals may attribute to the supporting carbon tape. The EDS spectrum clearly confirms that PVP was completely decomposed and Sn precursors were oxidized to  $\text{SnO}_2$  nanostructure after calcination.

The after-calcined products prepared from precursors with different PVP contents were characterized by XRD measurement and corresponding results are shown in Fig. 4. The results confirm the formation and crystallinity of  $\text{SnO}_2$ . All the characteristic peaks are associated to (110), (101), (200), (211), (220), (002), (310), (112), (202) and (321) planes nicely indexed with rutile tetragonal structure of  $\text{SnO}_2$  crystal (JCPDS Card No. 41-1445)[21]. No other peaks were found in XRD patterns. This feature strongly confirm that the variation of PVP concentration in the precursor solution merely affects to the rearrangement of crystal structure and morphology of  $\text{SnO}_2$  without impurities in  $\text{SnO}_2$  crystallized phase.

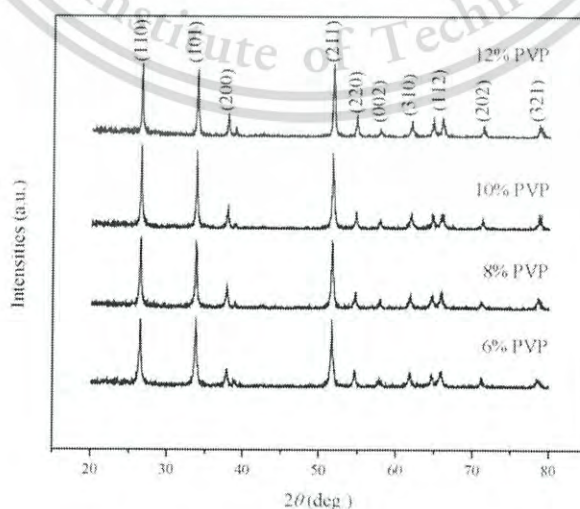


Figure 4. XRD pattern of after-calcined  $\text{SnO}_2$  nanostructures prepared from precursors with the different PVP concentrations.

This material is reserved for educational use only, not allowed for commercial use.

Forbidden to modify the content, and cite the document when use.

#### 4. Conclusion

In this work, the various structures of SnO<sub>2</sub> were synthesized by electrospinning technique and calcination process starting from the precursor with different PVP concentrations. The morphologies of the as-spun nanofibers was in the form of long chain smooth nanofibers. The average diameter of fiber increased and the beads in fibers were lower when the polymer concentration was increased. The structure of as-spun nanofibers was transformed to SnO<sub>2</sub> fiber-like structure after calcined at 600°C for 3 h. The solvent evaporation, decomposition of polymer and phase separation plays a key role in the formation of SnO<sub>2</sub> with different morphologies including nanobeads, nanosheets or flake-like structure. The EDS spectra and XRD patterns confirmed the existence of relevant elements and the formation of SnO<sub>2</sub> synthesized by these processes.

#### Acknowledgments

This work has been supported by Rajamangala University of Technology Tawan-Ok with the Ph.D. scholarship. The author would like to thank Rajamangala University of Technology Thanyaburi (RMUTT) for XRD analysis. This work is financially supported by King Mongkut's Institute of Technology Ladkrabang Research Fund.

#### References

1. B. H. Jang, O. Landau, S. J. Choi, J. Shin, A. Rothschild, I. D. Kim, Selectivity enhancement of SnO<sub>2</sub> nanofiber gas sensors by functionalization with Pt nanocatalysts and manipulation of the operation temperature, *Sens Actuators B.*, **188**, 156–168 (2013).
2. J. P. Cheng, B. B. Wang, M. G. Zhao, F. Liu, X. B. Zhang, Nickel-doped tin oxide hollow nanofibers prepared by electrospinning for acetone sensing, *Sens Actuators B.*, **190**, 78–85 (2014).
3. X. Liu, D. Teng, T. Li, Y. Yu, X. Shao, X. Yang, Phosphorus-doped tin oxides/carbon nanofibers webs as lithium-ion battery anodes with enhanced reversible capacity, *J Power Sources.*, **272**, 614–621 (2014).
4. R. Nirmala, H. Y. Kim, R. Navamathavan, C. Yi, J. J. Won, K. Jeon, A. Yousef, R. Afeesh, M. El-Newehy, Photocatalytic activities of electrospun tin oxide doped titanium dioxide nanofibers, *Ceram Int.*, **38**, 4533–4540 (2012).
5. T. Jia, X. Wang, W. Wang, Y. Wang, G. Liao, Y. Xiong, Facile synthesis of porous SnO<sub>2</sub> spherical-like aggregates and their gas sensing property, *Int Ferroelectr.*, **128**, 30–36 (2011).
6. K. Zhao, G. Du, G. Qin, Y. Liu, H. Zhao, Facile synthesis of boscage-like SnO<sub>2</sub> nanorods by hydrothermal method, *Mater Lett*, **141**, 351–354 (2015).
7. M. R. Yang, S. Y. Chu, Studies on the characterization of the SnO<sub>2</sub> nanowires growth, *Int Ferroelectr.*, **78**, 299–307 (2006).
8. G. H. Lee, Rapid synthesis of SnO<sub>2</sub> nanowires employing solar thermal energy, *Ceram Int.*, **40**, 9903–9906 (2014).
9. J. Yuan, H. Li, Q. Wang, X. Zhang, S. Cheng, H. Yu, X. Zhu, Y. Xie, Facile fabrication of aligned SnO<sub>2</sub> nanotube arrays and their field-emission property, *Mater Lett.*, **118**, 43–46 (2014).
10. H. E. Wang, L. J. Xi, R. G. Ma, Z. G. Lu, C. Y. Chung, I. Bello, J. A. Zapien, Microwave-assisted hydrothermal synthesis of porous SnO<sub>2</sub> nanotubes and their lithium ion storage properties, *J Solid State Chem.*, **190**, 104–110 (2012).

11. S. Z. Kang, Z. Cui, J. Mu, Electrical property of tin oxide doped with multi-walled carbon nanotubes, *J Dispersion Sci Technol.*, **28**, 569–571 (2007).
12. N. Yongvanich, S. Maensiri, Synthesis of cobalt-doped SnO<sub>2</sub> nanoparticles by chemical precipitation with Chelating, *Int Ferroelectr.*, **156**, 53–57 (2014).
13. J. Doshi, D. H. Reneker, Electrospinning process and applications of electrospun fibers, *J Electrostat.*, **35**, 151–160 (1995).
14. S. Wongsasulak, K. M. Kit, D. J. McClements, T. Yoovidhya, J. Weiss, The effect of solution properties on the morphology of ultrafine electrospun egg albumen PEO composite fibers, *Polymer*, **48**, 448–457 (2007).
15. W. K. Son, J. H. Youk, T. S. Lee, W. H. Park, The effects of solution properties and polyelectrolyte on electrospinning of ultrafine poly(ethylene oxide) fibers, *Polymer*, **45**, 2959–2966 (2004).
16. J. M. Deitzel, J. Kleinmeyer, D. Harris, N. C. Beck Tan, The effect of processing variables on the morphology of electrospun nanofibers and textiles, *J Eur Ceram Polymer*, **42**, 261–272 (2001).
17. J. Muangban, P. Jaroenapibal, Effects of precursor concentration on crystalline morphologies and particle sizes of electrospun WO<sub>3</sub> nanofibers, *Ceram Int.*, **40**, 6759–6764 (2014).
18. Z. Li, C. Wang, *One-Dimensional nanostructures Electrospinning Technique and Unique Nanofibers*, SpringerBriefs in Materials, (2013).
19. W. Q. Li, S. Y. Man, J. Luo, Y. Z. Mao, L. Cheng, D. J. Gengzang, X. L. Xu, S. H. Yan, Synthesis of hollow SnO<sub>2</sub> nanobelts and their application in acetone sensor, *Mater Lett.*, **132**, 338–341 (2014).
20. X. Wang, H. Fan, P. Ren, Electrospinning derived hollow SnO<sub>2</sub> microtubes with highly photocatalytic property, *Catal Commun.*, **31**, 37–41 (2013).
21. X. Xia, X. J. Dong, Q. F. Wei, Y. B. Cai, K. Y. Lu, Formation mechanism of porous hollow SnO<sub>2</sub> nanofibers prepared by one-step electrospinning, *Express Polym Lett.*, **6**, 169–176 (2012).
22. J. Wua, Q. Huang, D. Zeng, S. Zhang, L. Yang, D. Xia, Z. Xiong, C. Xie, Al-doping induced formation of oxygen-vacancy for enhancing gas-sensing properties of SnO<sub>2</sub> NTs by electrospinning, *Sens Actuators B.*, **198**, 62–69 (2014).
23. W. Wang, J. Zhou, S. Zhang, J. Song, H. Duan, M. Zhou, C. Gong, Z. Bao, B. Lu, X. Li, W. Lan, E. Xie, A novel method to fabricate silicananotubes based on phase separation effect, *J Mater Chem.*, **20**, 9068–9072 (2010).

## Author Biography

Name	Mr. Somtop Santibenchakul
Date of Birth	2 January 1977
Address	219/38 Moo.9 Bansaun Sukumvit Road Maung Chonburi 20000
Education	(1998) Bachelor of Science in Industrial Chemistry GPA 2.20 King Mongkut's Institute of Technology Ladkrabang (KMITL) (2005) Master of Science in Analytical Chemistry GPA 3.40 Burapha University
Scholarship	Rajmangala University of Technology Tawan-Ok (Rmutto) for the Ph.D scholarship
Academic Publication(s)	<ol style="list-style-type: none"> <li>1. S. Santibenchakul, S. Chaiyasith and W. Pecharapa. "PVP-assisted Sb-doped SnO<sub>2</sub> nanofibers synthesized by electrospinning process" <i>Key Engineering Materials</i> 675-676 (2016) pp 150-153.</li> <li>2. S. Santibenchakul, S. Chaiyasith and W. Pecharapa. "Sb/F-Codoped SnO<sub>2</sub> Nanofibers Synthesized by Electrospinning" <i>Journal of Nanoscience and Nanotechnology</i> 16 (2016) pp 13001-13006.</li> <li>3. S. Santibenchakul, S. Chaiyasith and W. Pecharapa. "Effect of PVP concentration on microstructure and physical properties of electrospun SnO<sub>2</sub> nanofibers" <i>Integrated Ferroelectrics</i> 175 (2016) pp 130-137.</li> </ol>